

Janne Aho

Adaptive Signal Processing Techniques and Realistic Propagation Modeling for Multiantenna Vital Sign Estimation

School of Electrical Engineering

Thesis submitted for examination for the degree of Master of
Science in Technology.

Espoo 3.1.2013

Thesis supervisor:

Academy prof. Visa Koivunen

Thesis instructor:

D.Sc. (Tech.) Jussi Salmi

Author: Janne Aho

Title: Adaptive Signal Processing Techniques and Realistic Propagation
Modeling for Multiantenna Vital Sign Estimation

Date: 3.1.2013

Language: English

Number of pages:10+87

Department of Signal Processing and Acoustics

Professorship: Signal Processing

Code: S-88

Supervisor: Academy prof. Visa Koivunen

Instructor: D.Sc. (Tech.) Jussi Salmi

This thesis addresses the problem of vital sign estimation through the use of adaptive signal enhancement techniques with multiantenna continuous wave radar. The use of different adaptive processing techniques are proposed in a novel approach to combine signals from multiple receivers carrying the information of the cardiopulmonary micro-Doppler effect caused by breathing and heartbeat. The results are based on extensive simulations using a realistic signal propagation model derived in the thesis. It is shown that these techniques provide a significant increase in vital sign rate estimation accuracy, and enable monitoring at lower SNR conditions.

Keywords: micro-Doppler, vital sign estimation, adaptive filtering, SIMO Radar, spectral estimation

Tekijä: Janne Aho

Työn nimi: Adaptiiviset signaalinkäsittelymenetelmät ja realistiset häviömallit elintoimintojen estimoinnissa moniantennitutkalla

Päivämäärä: 3.1.2013

Kieli: Englanti

Sivumäärä:10+87

Signaalinkäsittelyn ja akustiikan laitos

Professuuri: Signaalinkäsittely

Koodi: S-88

Valvoja: Akatemiaprof. Visa Koivunen

Ohjaaja: TkT Jussi Salmi

Tämän työn keskeisimpänä tavoitteena on ihmisen elintoimintojen tarkkailu ja estimointi käyttäen radiotaajuisia mittauksia ja adaptiivisia signaalinkäsittelymenetelmiä monen vastaanottimen kantoaaltotutkalla. Työssä esitellään erilaisia adaptiivisia menetelmiä, joiden avulla hengityksen ja sydämen värähtelyn aiheuttamaa micro-Doppler vaihemodulaatiota sisältävät eri vastaanottimien signaalit voidaan yhdistää. Työssä johdetaan lisäksi realistinen malli radiosignaalien etenemiselle ja heijastushäviöille, jota käytettiin moniantennitutkan simuloinnissa esiteltyjen menetelmien vertailemiseksi. Saatujen tulosten perusteella voidaan osoittaa, että adaptiiviset menetelmät parantavat langattoman elintoimintojen estimoinnin luotettavuutta, ja mahdollistavat monitoroinnin myös pienillä signaali-kohinasuhteen arvoilla.

Avainsanat: micro-Doppler, elintoimintojen estimointi, adaptiiviset suotimet, SIMO tutka, spektrin estimointi

Preface

The work of this thesis was carried out in the SMARAD Center of Excellence, in the department of Signal Processing and Acoustics at Aalto University School of Electrical Engineering. I would like to thank the department of Signal Processing and Acoustics for providing the facilities and tools for the work. Also, I want to thank my colleagues for the encouraging and pleasant social atmosphere, which has made working here a joy.

I want to thank my supervisor academy prof. Visa Koivunen for giving me the opportunity to work on such an interesting topic and providing the financial support. His years of experience in academic writing have played a key role in finalizing this thesis through detailed advices and commenting. I also want to give special thanks to my instructor and 'personal coach' Dr. Jussi Salmi, for his perseverance, as well as his technical expertise in providing the answer to all of my questions, and occasionally even presenting the questions for me. I thank my colleague Dr. Mário Costa for his support in refining the beamforming techniques, and my friend BM. Antti Tuokko for providing the related Medical literature.

I thank my family for their everlasting love and support that have helped me over numerous challenges in life.

Finally, I want to thank my future wife Laura, who has supported me through her love and attention, not only during this work, but throughout our time together.

In memory of my father.

Otaniemi, 3.1.2013

Janne Aho

Contents

Abstract	ii
Abstract (in Finnish)	iii
Preface	iv
Contents	v
Symbols and Abbreviations	vii
1 Introduction	1
1.1 Motivation	1
1.2 Micro-Doppler: Applications and Challenges	2
1.3 Contributions	4
1.4 Outline of the Thesis	4
2 Models for Vital Sign Monitoring	5
2.1 Physiology and Modeling of Cardiopulmonary Activity	5
2.1.1 Cardiac Activity	5
2.1.2 Respiration	7
2.2 Continuous Wave Radar	8
2.2.1 Operation and Motion Detection	9
2.2.2 Micro-Motion Dynamics in Radar	11
2.2.3 Micro-Doppler Motion Model	12
2.2.4 Multipath Signal Model	13
2.3 Multiantenna Vital Sign Signal Models	15
2.3.1 Multiantenna Receiver System	15
2.3.2 Amplitude Model	17
2.3.3 Reflection Model	18
2.3.4 General Multiantenna Signal Model	20
2.3.5 Beamforming Signal Model	21
2.4 Conclusion and Remarks of Vital Sign Modeling	25
3 Signal Processing for Vital Sign Estimation	26
3.1 Received Signal Structure	26
3.2 Complex Signal Demodulation	27
3.2.1 Linear Demodulation	28
3.2.2 Nonlinear Demodulation	29
3.3 Overview of Spectral Estimation	30
3.3.1 Periodogram	31
3.3.2 Capon	32
3.3.3 Fast Recursive Capon Estimation	33
3.4 Time-Frequency Analysis	34
3.4.1 Short-Time Fourier Transform	35

3.4.2	Wigner-Ville Distribution	35
3.5	Discussion on Suitable Algorithms	38
4	Multiantenna Adaptive Signal Enhancement Techniques	39
4.1	Review of Multiantenna Vital Sign Monitoring	39
4.2	Adaptive Noise Cancellation	40
4.2.1	Minimum Mean-square-error Filtering	41
4.2.2	Least-Mean-Square Algorithm	44
4.2.3	Normalized Least-Mean-Square Algorithm	45
4.2.4	Recursive Least-Square Algorithm	47
4.3	Spatial Methods	49
4.3.1	Conventional Beamforming	50
4.3.2	Optimum Beamforming	51
4.3.3	Robust Capon Beamforming	53
4.3.4	Direction of Arrival Estimation	54
4.4	Maximum Ratio Combining	56
4.5	Independent Component Analysis	57
4.6	Adaptive Vital Sign Estimation System	59
4.7	Challenges with Adaptive Techniques	60
5	Simulation results	62
5.1	Simulation Environment and Measurement Setup	62
5.2	Adaptive Processing Parameter Optimization	63
5.3	Performance of Adaptive Noise Canceller	65
5.3.1	Results for Estimating Both Cardiopulmonary Activities	65
5.3.2	Results for Estimating Heartbeat Only	68
5.4	Simulation Results for Spatial Methods	70
5.4.1	Results for Beamforming on One Subject	71
5.4.2	Results for Directional Interference Cancelling	73
6	Summary	77
6.1	Discussion	77
6.1.1	Performance and Application of Adaptive Techniques	77
6.1.2	Array Size Considerations	78
6.2	Conclusion	79
6.3	Future Work	79
	References	81
	Appendix A	86
A	Convergence Analysis of LMS Algorithm	86

Symbols and Abbreviations

Symbols

a_m	signal amplitude at m^{th} receiver in IQ-plane
$a_{m,p}$	signal amplitude of p^{th} propagation path at m^{th} receiver
A_m, A_p	effective area of m^{th} receiver, and p^{th} reflection point
\mathbf{a}	Vandermonde type Fourier Transform vector
\mathbf{A}	mixing matrix
\mathbf{b}	array response vector
c	speed of light
\mathbf{c}	channel coefficient vector
\mathbf{C}	positive definite diagonal uncertainty matrix
\mathbf{d}_m	vector of m^{th} receiver coordinates
D	size of array aperture
\mathbf{D}	matrix of receiver coordinates
$e(k)$	instantaneous estimation error at discrete time k
\mathbf{e}	vector of estimation errors
f	frequency
\mathbf{F}_{amb}	array response ambiguity function
\mathbf{g}	adaptation gain vector
G_m, G_T	gain of m^{th} receiver, and gain of transmit antenna
\mathbf{h}	adaptation channel coefficients
H	frequency response of adaptive channel coefficients
\mathbf{I}	identity matrix
k	discrete time-index
L	filter length
m	receiver array antenna index
M_R	number of receive antennas
M_T	number of transmit antennas
p	propagation path index
P	number of vital sign propagation paths
P_m, P_T	power received by m^{th} receiver, total transmit power
$P(\theta)$	narrow frequency window around center frequency θ
$r(k)$	autocovariance sequence
$r_p, r_{\bar{p}}$	radial distance from transmitter to target, and receiver to target
\mathbf{r}_{xy}	cross-correlation vector of x and y
$\hat{\mathbf{R}}$	estimate of autocovariance matrix
$\mathbf{R}_{xx}, \mathbf{R}_{i+n}$	autocovariance matrix of sequence x , autocovariance of interference plus noise
s	static reflection path index
$s(t)$	vibration model
$\mathbf{s}(t)$	vector of mutually independent source signals
S	number of static reflection paths
$S(t, \omega)$	time-frequency distribution of STFT
$SW(t, \omega)$	smoothed pseudo WVD of a continuous time signal

$SW(k, m)$	smoothed pseudo WVD of a discrete time signal
t	continuous time-index
u	amplitude of vibration
\mathbf{U}	matrix of true normalized array response vectors
\mathbf{U}_{bf}	matrix of normalized beamforming array response vectors
v_r	target radial velocity relative to radar
v_g	inner product of FT vector and a priori Kalman gain vector
$w(t)$	window sequence
$\mathbf{w}(k)$	vector of additive white Gaussian noise
$W(t, \omega)$	Wigner-Ville distribution of a signal
\mathbf{W}	inverse of mixing matrix
$x(k)$	received adaptive processing input samples
$\mathbf{x}(t)$	mixture vector of independent components
\mathbf{X}	matrix of adaptive processing input samples
$y(k)$	adaptive processing reference signal, and beamforming output
\hat{y}	estimate of adaptive processing reference signal
\mathbf{y}	vector of received samples
$Y(t, \omega)$	short-Time Fourier Transform of a signal
β	step-size
δ	signal substance penetration depth
ϵ	permittivity of a substance
η	ratio of refractive indices
θ_p	angle of arrival at p^{th} reflection point
$\theta_{m,p}$	angle between m^{th} receiver and normal of p^{th} reflection point
$\tilde{\theta}_p$	angle of absorption at p^{th} reflection point
φ_p	angle between transmitter broadside and p^{th} reflection point
$\varphi_{m,p}$	angle between m^{th} receiver broadside and p^{th} reflection point
φ_R	signal direction of arrival at receiver
λ	wavelength, forgetting factor
τ	time-delay
$\phi(t)$	signal phase
$\hat{\phi}(\omega)$	estimated signal spectrum
ψ	initial phase of micro-Doppler motion
ω	angular frequency

Operators

$E\{\cdot\}$	expected value
$\Im[z]$	imaginary part of a complex number z
\log_{10}	base 10 logarithm
\max	maximum value
\min	minimum value
$\Re[z]$	real part of a complex number z
$ \cdot $	absolute value
$(\cdot)^T$	transpose of a vector or matrix
$(\cdot)^*$	conjugate of a vector or matrix
$(\cdot)^H$	Hermitian (conjugate) transpose of a vector or matrix
$(\cdot)^{-1}$	inverse of a matrix
\circ	Hadamard matrix element wise product
∇	gradient

Abbreviations

BSS	Blind Source Separation
CW	Continuous Wave
EKG	Elektrokardiogramm
FBA	Filter-Bank Approach
FIR	Finite-Impulse Response
FM	Frequency Modulation
FFT	Fast Fourier Transform
GRLT	Generalized Likelihood Ratio Test
ICA	Independent Component Analysis
IF	Instantaneous Frequency
ISAR	Inverse Synthetic Aperture Radar
LMS	Least-Mean-Squares
LOS	Line of Sight
LS	Least-Squares
MFB	Matched Filter Beamformer
MIMO	Multiple-Input Multiple-Output
ML	Maximum-Likelihood
MMSE	Minimum Mean-Square-Error
MRC	Maximum Ratio Combining
MSE	Mean-Square-Error
MTI	Moving-Target Indicator
MUSIC	Multiple Signal Classification
MVDR	Minimum-Variance Distortionless Response
PSD	Power Spectral Density
RCB	Robust Capon Beamformer
RCS	Radar Cross Section
SAR	Search and Rescue
SIMO	Single-Input Multiple-Output
SINR	Signal to Interference-Plus-Noise Ratio
SISO	Single-Input Single-Output
SMI	Sample Matrix Inversion
SNR	Signal to Noise Ratio
SPWVD	Smoothed Pseudo Wigner-Ville Distribution
STAP	Space-Time Adaptive Processing
STFT	Short-Time Fourier Transform
TFD	Time-Frequency Distribution
ULA	Uniform Linear Array
WSS	Wide-Sense Stationary
WVD	Wigner-Ville Distribution

1 Introduction

1.1 Motivation

Through the latest developments in wireless communication systems, medical technology has become less intrusive and more sophisticated with non-contact monitoring systems. In addition to telecommunications, high-frequency wireless radios may be employed for non-contact monitoring of human vital signs, including breathing and heart beat. The development of such measurement systems has become an active research topic especially due to the growing need of location independent healthcare services. Currently, the main limitation for online medical diagnosis is not set by the existing communication infrastructure, but the lack of compact and reliable mobile medical sensors. However, as new smartphones carry multiple high end radios on board and enable wireless access to the Internet, these mobile devices could become the missing link between routine visits at the doctor and online medical diagnosis.

This thesis studies the application of wireless microwave radar systems in human vital sign monitoring. The use of microwave radar systems for human life-detection was studied already in the 1970's, and later on in 1980's when the use of X-band frequencies was proposed for detecting respirational and cardiovascular motion [1, 2]. Subsequent studies have also shown that wireless microwave radar can be used in human life-detection behind various obstacles and earthquake rubble up to three meters [3]. Currently, a big driver on the topic are new high end mobile phones that carry these microwave radios embedded, in addition to the high computational power. Therefore, vital sign estimation using such a device is of high interest as soon everyone could be carrying personal healthcare services in their pocket. However, there are specific challenges still related to detection and estimation of vital signs, which is why this technology is not yet available.

Wireless detection and monitoring of the cardiopulmonary vital signs is based on the vibrating motion of the body resulting from breathing and heartbeat activities. A radar system observes this vibration as small periodic Doppler shifts, known as micro-Doppler. At low signal-to-noise ratio (SNR), accurate micro-Doppler estimation presents a major challenge for vital sign monitoring using single antenna continuous wave radar systems. The application of multiple receive antennas has been introduced in vital sign monitoring to overcome challenges like random body movement cancellation, signal enhancement, and resolving or separating different source of micro-Doppler [4, 5]. While these techniques have limitations in fixed measurement geometry and implementation complexity, the current multiantenna vital sign solutions have not addressed the problem of rate estimation under low SNR conditions.

In this thesis, adaptive multiantenna signal processing techniques are proposed for enhancing micro-Doppler effect caused by vital signs such as heart beats and breathing. The system model employs CW radar and multiantenna receiver. The performances of the proposed methods are evaluated in extensive simulations and using realistic radio wave propagation models derived in this thesis. The performance

gains in low SNR regime are of particular interest.

1.2 Micro-Doppler: Applications and Challenges

During the last decade, there has been an increasing interest in the study of micro-Doppler dynamics due to its ability to provide unique target specific movement signatures [6]. It has been proposed that the micro-Doppler information can be used to distinguish vehicles, including cars, airplanes, helicopters and ballistic targets, based on the mechanical vibration or rotation of structures, such as the engine, blades on a helicopter, or the wobble of a missile [7] [8] [9]. Further studies have proposed models using micro-Doppler with high resolution inverse synthetic aperture radars (ISAR) for pedestrian identification based on their unique gait signatures [10] [11]. Also the healthcare industry has received attention with studies on noncontact vital sign measurements utilizing micro-Doppler motion models [12] [13], see Figure 1. While this thesis focuses on the use of cardiopulmonary micro-Doppler information solely for vital sign rate estimation, the same information could be used by healthcare doctors in diagnosing potential heart diseases like arrhythmia, or sleep apnea [14]. A nonintrusive active wireless noncontact monitoring system provides also a convenient alternative for strap on premature infant cardiopulmonary monitoring and in-home healthcare monitoring [12]. Other proposed applications include entrance surveillance monitoring and movement tracking, various search and rescue (SAR) tasks with victim locationing in smoke diving and earthquake rubble for firemen, border patrol and police. The military has also shown interest in through-the-wall imaging radar for antiterrorist activities.

The many applications of vital sign detection pose different requirements for the used radar systems. Required sensitivity and Doppler resolution are key system parameters that depend on the used radar waveform and frequency. Other common design parameters are the physical size of the radar unit, dynamic operating range, available processing power, and mobile unit battery lifetime. Applications such as search and rescue require a considerably larger operating range for vital sign detection and are usually battery operated compared to for example clinical health care monitoring. The latter application takes place in close to ideal conditions, where the subject is typically stationary with respect to the radar and there is very little motion clutter from the environment. Moreover, in health care monitoring the distance between the radar unit and monitored subject is adjustable for optimal detection, whereas in search and rescue, and surveillance applications the subject location is generally unknown. Radar systems that would address these issues with digital automatic gain control circuits and improved dynamic range, are still under development [12].

In many vital sign detection applications utilizing battery operated radar systems, minimizing the processing power is critical for achieving sufficiently long operational lifetime. Since various applications, such as entrance security, fire rescue, earthquake victim locationing, and border patrol need merely the knowledge whether heartbeat or respiration is present or not, high-complexity signal processing can be kept to minimum. Many of these applications are time critical, thus it is enough for

the system to make a binary decision on the presence of vital signs. For example a fireman needs to know whether there is a person trapped in a smoke filled room or not, and an entrance security system if an intruder has entered a room, hence there is no need for accurate vital sign estimation. As spectrum estimation methods are not required for such applications, system costs and power consumption can be reduced by eliminating the need of advanced digital signal processing microprocessors [12].

Further challenges in vital sign estimation are imposed by weak signal returns and interference caused by excess motion artifacts. While noncontact vital sign detection is based on sensing small physiological movements on the order of millimeters, random body movement and environment dynamics can cause a significant interference for accurate detection. Moreover, the problem of weak signal returns is emphasized when the signal conditions deteriorate or the subject is further away from the radar. However, recent studies in vital sign estimation have developed accurate mathematical models for detecting heartbeat and breathing motion using continuous wave radar. It has been shown that the application of these models along with robust high resolution spectral estimation methods in a single-input single-output (SISO) continuous wave radar facilitate accurate wireless vital sign monitoring at close range [13, 15]. One significant challenge still remaining in wireless vital sign estimation is the weakness of the vital sign information in the reflected return signal. In order to solve this problem, advanced signal enhancement techniques in multiantenna continuous wave radar systems are developed in this thesis.

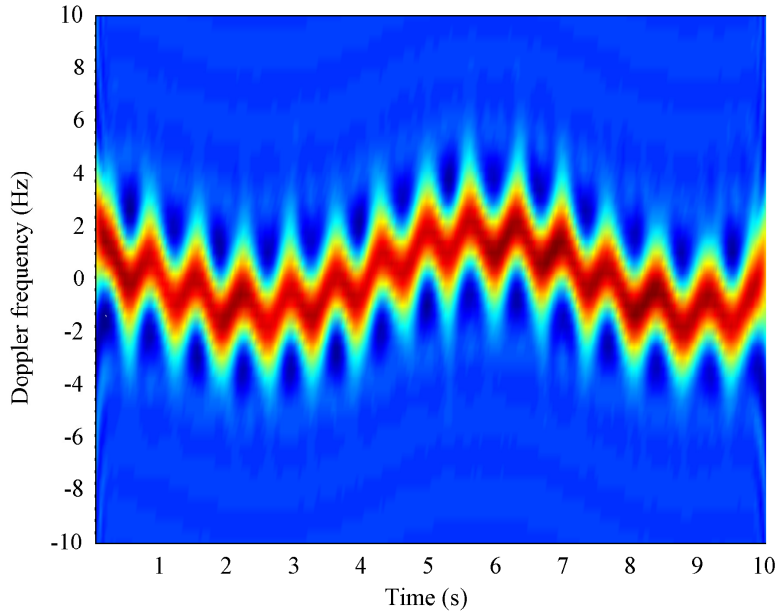


Figure 1: Time-frequency spectrum illustrating the micro-Doppler effect caused by breathing and heartbeat. Heartbeats are visible as fast variations in the time-frequency spectrum, whereas breathing results in lower micro-Doppler frequencies.

1.3 Contributions

This thesis proposes a novel approach for signal enhancement in wireless vital sign monitoring using adaptive noise cancellation methods with multiple receivers. Also, the application of spatial filtering methods for directional micro-Doppler interference cancellation is presented. A mathematical model for radio wave propagation is derived to allow realistic modeling of signal attenuation and reflections. This model is applied in MATLAB simulations studying the performance of the presented adaptive processing techniques. Based on the simulations, it is shown in this thesis that adaptive multiantenna signal enhancement techniques may be used to solve the problem of vital sign monitoring in low SNR regime. Finally, a paper on the presented adaptive methods was written and submitted to the 2013 IEEE Radar Conference [16].

1.4 Outline of the Thesis

The thesis is structured as follows. In Chapter 2 the physiology and dynamics of heartbeat and breathing activities are described. Also, the continuous wave (CW) radar system is presented for vital sign monitoring, along with detailed derivation of a general signal propagation micro-Doppler model for single and multiantenna systems. Chapter 3 describes the signal processing and spectral estimation tools used for extracting the instantaneous vital sign rate estimates from return signals. The adaptive multiantenna signal enhancement techniques are introduced in Chapter 4, which gives a detailed presentation of the applied adaptive noise cancellation and spatial processing techniques. Chapter 5 provides simulation results demonstrating the excellent performance of the proposed signal enhancement techniques. Finally, Chapter 6 summarizes the contributions and results in this thesis.

2 Models for Vital Sign Monitoring

Although microwave life-detection systems were proposed already in the 1970's [1], only recent advances in both wireless and medical technology have offered an alternative to the common chest-strap respiration and heartbeat monitors. This new noncontact monitoring technology has several advantages in terms of subject comfort, measurement reliability, and both implementation and acquisition costs. While there is no physical contact during monitoring, the system does not confine or inhibit the subject, nor does it cause any discomfort or skin irritation like straps and electrodes [12]. This makes the system ideal for long-term continuous monitoring, which also increases measurement reliability as subjects are unaware of the system, and thus less likely to unintentionally alter their respiration or heartbeat due to monitoring involved stress. Furthermore, the low hardware costs and small physical size of the technology allows it to be embedded in various systems and consumer products.

This section begins by explaining the basic physiology behind cardiopulmonary activity, and how respiration and heartbeat are detected using a continuous wave radar. Thereafter, the section focuses on the applied radar technology by giving an overview on the operation and motion detection capabilities of a SISO continuous wave radar. In order to further elaborate the use of continuous wave radar is the detection of vital signs, a mathematical relation is given between the cardiopulmonary activities and observed radar signal frequency shifts. After the physiological system and measurement technology is defined, the section derives a micro-motion based micro-Doppler signal model for multiantenna receiver systems. For improved simulation accuracy, this extended signal model considers various signal propagation losses, including path loss and nonideal reflections. Finally, the section presents a commonly used alternative multiantenna signal model known as the beamforming model, which relies on specific assumptions on subject range. Due to its mathematical simplicity, the beamforming model is used when introducing spatial methods later on in chapter 4.

2.1 Physiology and Modeling of Cardiopulmonary Activity

Talking, stress and exercise influence the instantaneous heartbeat and breathing rates. Additionally, as the heart muscle, like skeletal muscles, requires oxygen in the chemical reactions causing the muscle contraction, there is an evident co-dependence between the heart and breathing rates [17]. However, since the goal is simply to detect both vital signs, it is enough to model them as independent activities without any loss of generality for detection. The following sections give a brief introduction to the physiology of cardiac and respirational activities, and describe simple mathematical models that can be used to simulate these motions.

2.1.1 Cardiac Activity

Cardiac activity comprises of the contractions of the heart muscle and expansion of the pulmonary arteries and ventricles due to blood flows. The heart muscle

can be characterized by two unique features: the ability to generate self-stimulated rhythmic electrical impulses for muscle contraction, and conducting these impulses quickly forward through the heart. However, as skeletal muscles have similar conductive abilities, the electrical currents passing through the heart also spread into adjacent tissues. Consequently, part of this current passes directly to the surface of the body, thus enabling recording of the potentials induced by heart electrical currents, as is illustrated in Figure 2. Such recording is known as elektrokardiogramm (EKG).

On the other hand, the detection of cardiac activity using microwave radar systems relies on the physical motion of the contracting heart muscle. However, as most of the microwave signal reflections originate from the skin layer, which is shown in section 2.3.3, the radar is limited to observing heart induced vibration of the thorax or carotid artery, not the heart muscle itself. As the heart is protected by the rib cage and chest muscles, it is clear that the conducted heart vibration observable on the skin layer is smoothed and attenuated by the surrounding tissues. Consequently, the cardiac vibration is strongest on the left side of the thorax, directly above the heart muscle.

The rate of heart pumping is regulated by specialized fibers of the heart's conducting system capable of self-excitation. These fibers have an intrinsic normal discharge rate of 70 to 80 stimulations per minute. Furthermore, the rate is controlled by the volume of blood flowing into the heart, as well as the autonomic nervous system that can increase the regular heart rate by up to 100 per cent under extrinsic stimulation. Consequently, the pumping rate can be decreased or even stopped for a few seconds under strong parasympathetic nervous stimulation. [17] In general, rapid natural fluctuations of the heart result from external stimulus from the environment or sudden mental stress in situations, such as job interviews and moments of frightening.

It is clear that the heart induced physical vibration on a healthy subject does not obey a perfect periodic sinusoidal motion, but is characterized by a time-varying rhythmic pulsation. Nevertheless, to illustrate the applied radar system detection capabilities of any periodic motion, the cardiac activity on a subject's body is modeled as a sinusoid with a temporally fluctuating period. To justify the sinusoid

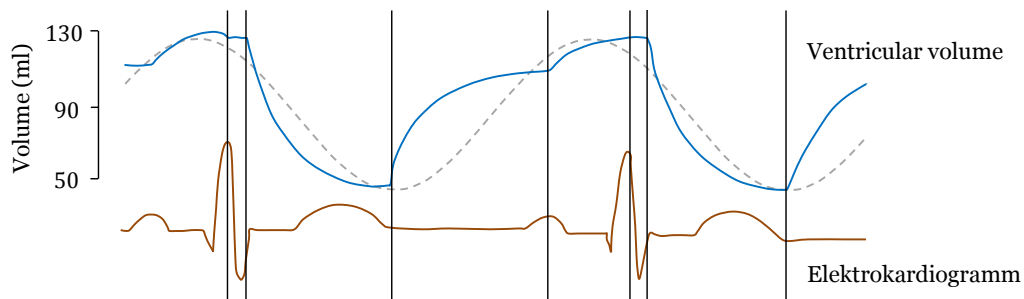


Figure 2: Elektrokardiogramm measured potential variations and ventricular volume of the heart during two cardiac cycles [17]. The dashed line represents a sinusoidal approximation of the heart activity.

approximation, it can be seen in Figure 2 that the ventricular volume of the heart follows roughly a continuous sinusoidal pattern during one cardiac cycle. Although the observed vibration originates from the periodic contraction and relaxation of the heart muscle, rather than expansion due to blood flow, the mechanical vibration is smoothed by the protective tissues round the heart. Even though the sinusoidal model is a rough approximation of the true muscular vibration, this model allows for simplified simulations without the loss of generality for detecting the rhythmic cardiac activity. The same sinusoidal approximation is made also when simulating respiratory activity, which is discussed in the following section.

2.1.2 Respiration

The main function of the respiratory system is to provide oxygen to the tissues and to remove any carbon dioxide from the body. This is accomplished, among other things, by the pulmonary ventilation system that causes lung expansion and contraction. It is exactly this slow periodic inspiration and expiration motion that may be observed using continuous wave radar systems.

Normally, breathing is regulated by the respiratory center nervous system located in the brain. The main functions of this nervous system are to control the rate and depth of expiration and inspiration. The rate is regulated so that the relative concentration of oxygen, carbon dioxide, and hydrogen ions in the blood circulation remain constant even under heavy exercise. Excess carbon dioxide ions are the main stimulant for the respiratory center to directly increase the strength of both inspiratory and expiratory signals for respective muscles. These signals further stimulate the respiratory muscles, including diaphragm and intercostal muscles that control the expansion of lungs. [17] At rest, a common respiration rate for a healthy person is from 6 to 20 breaths per minute, but during strong exercise the ventilation rate can increase above 140.

There is an intrinsic connection between the expansion of the lungs and the increase in diameter of the chest. During normal breathing, the lungs are expanded either by contraction of the diaphragm, which pulls the lungs downwards, or by

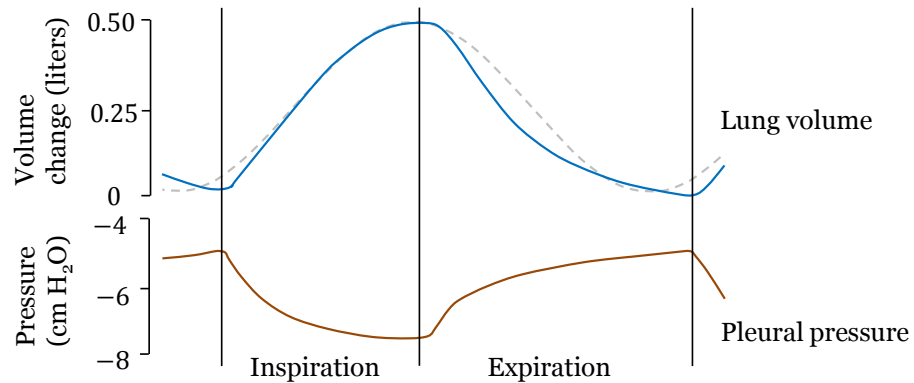


Figure 3: Variations in lung volume and pleural pressure during one respirational cycle [17]. The dashed line represents a sinusoidal approximation of the breathing activity.

elevation and depression of the ribs to increase and decrease the diameter of the chest cavity. During inspiration, both of these methods lead to an expansion of the lung volume, which consequently decreases the pleural pressure and results in air flow into the lungs. In rest, a regular respirational lung volume change for a male is 0.5 liters, which is illustrated in Figure 3 along with changes in the pleural pressure. The maximum lung capacity is however far greater, and can reach up to 5.8 liters especially with athletic people. [17]

In contrast to the cardiac activity, the lung volume variations in regular breathing are considerably larger. Therefore it is clear that also the physical movement generated by the respirational activity has larger amplitude, which makes it easier to detect with microwave radar systems. The reasoning for this is presented in section 2.2.3. Furthermore, as the volume changes during one respirational cycle are close to sinusoidal, as can be seen in Figure 3, this supports modeling breathing as a sinusoid with a temporally fluctuating period.

2.2 Continuous Wave Radar

A typical application of continuous wave radar is to detect target motion in the environment. This is also the case in vital sign monitoring, where the target motion is caused by the small physical vibration of heartbeat and breathing activity on the subject's thorax, as described in previous sections. The continuous wave radar detects motion by observing frequency changes in the reflected signals, which are caused by any radial movement relative to the radar. Such frequency shifts are known as Doppler shifts, which is also why the continuous wave radar is sometimes referred to as Doppler radar.

In addition to the vital sign application, CW radars are widely used in many basic consumer products as well as official and military grade equipment. Besides the well-known application of traffic control officials using CW radars to measure the speed of passing vehicles, a frequency modulated (FM) version of the radar can also be used in air traffic as simple altimeters to measure the distance between the ground and plane. However, in life critical missions such as commercial airplanes, the accuracy of laser operated devices is preferred over the cost savings of CW radar. Other common applications utilizing the inexpensive and compact technology of CW radars include car parking aid proximity sensors, entrance surveillance motion detectors in various premises, forecasting rapid changes in weather conditions especially near airports [18], and measuring the speed of a tennis ball after the serve. Also the military has found use for this technology by applying it in various early warning and combat missile systems [19], [20], as well as antiterrorist through-the-wall imaging.

Based on the numerous applications of CW radars, it is evident that the technology has multiple advantages compared to other types of radars. Firstly, the simple operation principle allows the CW radar to be built from common and inexpensive hardware components. This reduces the overall manufacturing costs and brings the technology available even for small entrepreneur businesses, thus allowing faster adaptation to new markets and applications, including basic consumer products. Secondly, the simple hardware makes the radar relatively failure safe and service

free with little or no maintenance costs. Therefore the CW radar is ideal for embedded systems like cars or aircrafts, where access to the components is usually limited. Finally, the simple structure of the radar allows for a small and compact assembly that is easy to carry around or embed into small devices, such as mobile phones and toys.

2.2.1 Operation and Motion Detection

There are two basic types of continuous wave radars: unmodulated and modulated. They both have the same operation principle of transmitting a continuous wave signal and monitoring the return for amplitude and phase changes. As their names already imply, the main difference with these two types of radars lie in the way the transmitted signal frequency is modulated. The unmodulated CW radar transmits a fixed frequency continuous wave signal, whereas the modulated radar uses frequency modulation to alternate the carrier frequency in which the signal is transmitted. It is in fact this underlying difference in modulation technique that determines the operational capabilities of the radar.

The unmodulated CW radar, or Doppler radar, has the ability to detect moving targets and determine their radial velocity relative to the radar. However, it will be explained later on that the CW radar is unable to detect stationary targets or perform ranging without the use of a transmit signal modulation scheme. Therefore, the unmodulated CW radar has most of its applications in the field of simple motion detection, such as traffic control and various sports. Moreover, since the goal in the vital sign estimation task is to simply detect the cardiopulmonary motion on the subject's body, it is enough to use an unmodulated CW radar in vital sign estimation. Consequently, this thesis focuses on the operation and application of the unmodulated CW radar. For brevity, in what follows, the unmodulated CW radar is referred to as CW radar, unless stated otherwise.

The CW radar operates by transmitting a fixed frequency $f_c = \omega_c/2\pi$ signal and analyzing the return for Doppler shifts f_D , as is illustrated in Figure 4. The return signals are a result of electromagnetic wave interactions with various objects and nonuniformities in the propagation medium. Whenever the transmitted signal encounters such nonuniformities, like a human body, part of the signal energy is reflected and scattered back to the receiver. In the case of a SISO radar observing a single moving reflection point, the transmission channel output at the receiver can be modeled as

$$y(t) = a(t) \sin(\omega_c(t - \tau(t))), \quad (2.2.1)$$

where $a(t)$ represents a complex channel amplitude, and $\tau(t)$ is the propagation time-delay. A complex representation of the output is obtained by IQ demodulating the signal (2.2.1) to its baseband form of

$$y(t) = a(t)e^{j\phi(t)}, \quad (2.2.2)$$

where $\phi(t)$ is the phase term carrying the Doppler information.

Variations in the two way signal path length modulate the phase of the signal, which in turn gives rise to the Doppler shifts. For example, assume that the radar

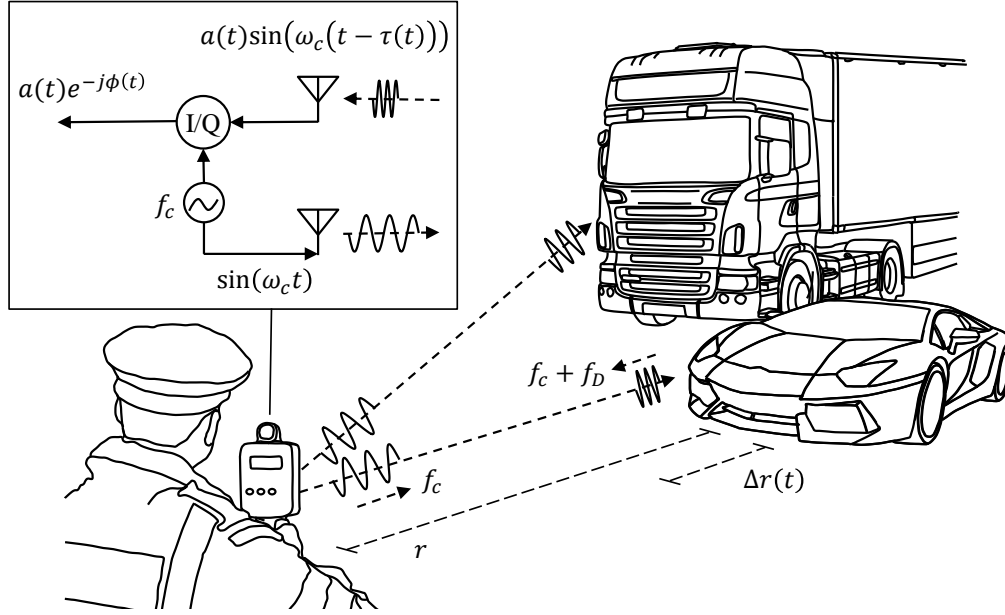


Figure 4: A basic CW radar operates by transmitting a fixed frequency f_c continuous signal, and monitoring the return for frequency shifts f_D .

is illuminating a target at distance r that is moving with a radial displacement of $\Delta r(t)$ towards the radar. Then the time-dependent signal propagation path length for a single reflection point is

$$\bar{r}(t) = r + \Delta r(t) = r + \frac{\partial r}{\partial t}t. \quad (2.2.3)$$

To highlight the propagation path length dependency on the target movement velocity, the equation (2.2.3) can be rewritten as

$$\bar{r}(t) = r + v_r t, \quad (2.2.4)$$

where v_r is the radial velocity component along the line of sight (LOS) of the radar. Furthermore, by assuming that the radar is monostatic, that is the transmitter and receiver are co-located, then the transmitted signal experiences a propagation time-delay of

$$\tau(t) \approx \frac{2}{c}\bar{r}(t), \quad (2.2.5)$$

where c denotes the speed of light. Consequently, the signal phase observed at the receiver is given by

$$\begin{aligned} \phi(t) &= \omega_c \tau(t) \\ &= 4\pi f_c \frac{r + v_r t}{c}, \end{aligned} \quad (2.2.6)$$

and consequently the output signal defined in (2.2.2) is

$$y(t) = a(t)e^{-j\omega_c \frac{2}{c}(r + v_r t)}. \quad (2.2.7)$$

It is worth noting that already a radial displacement of $v_r t = \lambda/2$ is enough to result in a complete 2π rotation of the signal phase. Therefore the Doppler shift corresponding to target motion is now given by the instantaneous phase change as

$$\begin{aligned} f_D &= \frac{1}{2\pi} \frac{\partial \phi(t)}{\partial t} \\ &= 2f_c \frac{v_r}{c}. \end{aligned} \quad (2.2.8)$$

Clearly there is a linear relation $2f_c/c$ between the instantaneous radial velocity and the instantaneous Doppler shift. This relation is the basis for estimating simple target motion using the Doppler information.

In the case that nothing is moving in the environment, that is $v_r = 0$ for all reflection points, then also the observed Doppler component f_D is zero, and the receiver output (2.2.7) is simply a constant complex number. Therefore stationary targets do not provide any information for CW radar, thus rendering the radar unable to detect them.

In addition to the phase changes, the transmitted signal experiences amplitude attenuation in the propagation medium. This loss in the received signal energy is generally caused by signal reflections, path loss, shadow fading, and multipath fading. In close range vital sign monitoring, the most significant losses result from path losses and signal reflections, where part of the energy is absorbed into the body and transformed into heat. A detailed model for the amplitude $a(t)$ is given in Section 2.3.2.

It is evident from equation (2.2.7) that any radial target movement relative to the radar results in reflected signal Doppler shifts that are observable at the receiver input. Furthermore, by applying proper signal processing techniques, the radar system can determine the radial velocity of the target by extracting v_r from the input signal. However in the vital sign application, the target motion is introduced by the periodic vibration of the subject's body. Therefore, instead of detecting simple constant velocity, the following section focuses on detecting small periodic micro-motion components by introducing the concept of micro-Doppler.

2.2.2 Micro-Motion Dynamics in Radar

A micro-Doppler motion model can be used to characterize vibrational periodic or quasi-periodic (periodic over some observation window) motion in radar applications. Micro-motion dynamics, such as mechanical vibration, tumbling, and rotation induce small Doppler modulations on the reflected radar signal. This phenomenon is referred to as micro-Doppler [8]. A basic CW radar is able to detect simple target motion and determine its velocity. This is usually enough information for a binary decision on target detection or simple velocity measurements. However, the main Doppler component does not generally provide enough information for radar systems performing sophisticated target movement analysis and identification, such as air surveillance and target recognition, and vital sign monitoring. Therefore, the additional micro-Doppler information is required for reliable target recognition and fine scale movement analysis.

In many radar applications like the vital sign estimation, the target might include micro-motions that induce time-varying micro-Doppler frequency shifts onto the carrier frequency. These micro-motions yield more accurate information about the target movement or inner structure, which are usually defining characteristics for different targets. For example, if a human is walking towards a CW radar, the forward movement of the body will generate a main Doppler component in the reflected signal, thus allowing detection of the person. Similarly, the swinging arms and legs will contribute additional micro-Doppler sidebands around the main Doppler shifted central carrier frequency. By nature, the dynamics of these micro-motions are fairly unique between individuals, thus according to [11] this additional information could be used to identify persons by their walk.

Like the movement of arms and legs, also the cardiopulmonary motion on the body of a subject results in detectable micro-motions. However compared to gait analysis, the detection of vital signs is more challenging due to the significantly smaller motion amplitude. Furthermore during normal walking, the average human heart rate is close to the rate of swinging arms that may also be illuminated by the radar. Therefore any arm movement produces significant interference to vital sign measurements. Additionally, any periodic wobble of the body, like nodding, will result in interfering micro-Doppler frequencies. In order to minimize these interferences, it is assumed in this thesis that the observed subject is stationary during the measurements, hence only the cardiopulmonary micro-Doppler is observed. As the elementary theory behind detecting vital sign micro-Doppler components is similar to basic operation principles of a CW radar, the following signal model derivation is merely an extension of the theory in section 2.2.1.

2.2.3 Micro-Doppler Motion Model

The micro-Doppler effect in vital sign monitoring is generated by the periodic motion of the pulsating heart muscle and chest, as described in section 2.1. Like in the case of a moving car, the vital sign motions modulate the phase of the reflected radar signal through propagation path length variations. In contrast to the previous case of constant Doppler-shift, the periodic cardiopulmonary vibration results in a smaller time-varying periodic micro-Doppler. Figure 5 illustrates the application of a CW radar system to the task of vital sign monitoring. In order to derive an expression for micro-Doppler effect observed at the receiver, it is necessary to find a vibrating model for the target.

The instantaneous amplitude of the cardiopulmonary motion is determined by the phase and strength of the respective breathing and heartbeat activities, as was presented in Section 2.1. For example, when a subject is breathing at rest, the chest cavity is expanding and contracting in a slow periodic manner, thus resulting in amplitude variations that reflect exhaling and inhaling. Similarly, the beat of heart muscle resonates on the chest, while the pulse of oxygenated blood spreads in the arteries. Consequently, by using the sinusoidal approximation of cardiopulmonary motions, the vibrations can be modeled independently as

$$s(t) = u(t) \cdot \sin(2\pi f(t) \cdot t + \psi), \quad (2.2.9)$$

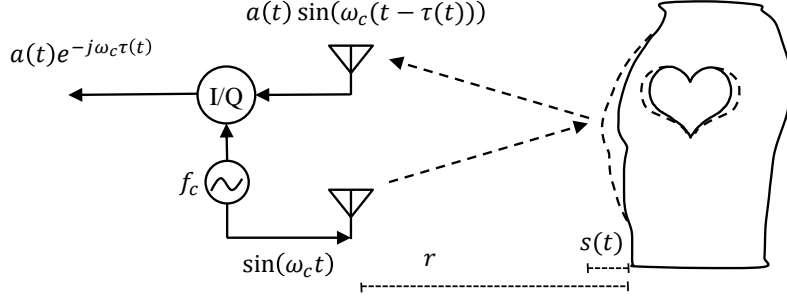


Figure 5: Example of micro-Doppler in continuous wave radar system with application to vital sign monitoring. For simplicity, the subject is assumed to be stationary with respect to the radar so that random body movements do not contribute the vital sign measurements.

where $u(t)$ denotes the amplitude, $f(t)$ the instantaneous frequency (IF), and ψ the initial phase of respective breathing and heartbeat activities. Furthermore, let us assume that the subject is at rest during measurements, and the small amplitude fluctuations may be neglected, that is $u(t) = u$ is constant. Then, the micro-Doppler effect of either vital sign seen at the receiver of a monostatic radar is given by

$$\phi(t) = \omega_c \cdot \frac{2 \cdot s(t)}{c} = \frac{4\pi f_c}{c} \cdot u \cdot \sin(2\pi f(t) \cdot t + \psi). \quad (2.2.10)$$

This indicates that also the observed micro-Doppler frequency shifts are periodic, and the magnitude depends on the chosen carrier frequency, and the phase and amplitude of the vibrating target motion.

It is worth noting that the model in (2.2.10) applies to the micro-Doppler of an individual vibrating target. In order to account for reflections from multiple sources, and to model both breathing and heartbeat simultaneously, the following section presents a micro-Doppler multipath signal model for general single receiver radar.

2.2.4 Multipath Signal Model

Recalling that in the case of a single constant velocity target, the received baseband signal was given by (2.2.2). Generally however, the SISO channel between a pair of transmit and receive antennas comprises of multiple propagation paths, that is reflections from chest, throat, etc., or secondary subjects nearby. Therefore, the channel output at the receiver can be modeled as a sum of the P distinct multipath components containing vital sign phase modulation, and S components with static interference from the environment. Hence, the receive input signal can be modeled as

$$y(t) = \sum_{p=1}^P y_p(t) + \sum_{s=1}^S y_s + y_l + w(t), \quad (2.2.11)$$

where p denotes the propagation path component $y_p(t)$ containing contributions from vital signs, s denotes the static reflections y_s , l denotes the direct transmitter to

receiver leakage y_l , and $w(t) \sim \mathcal{N}(0, \sigma_w^2)$ is white noise [13]. By further assuming that both the measurement environment and radar geometry are static, the interference and leakage components do not contribute any Doppler shifts because

$$\begin{aligned} y_s &= a_s \cdot e^{-j\omega_c \cdot \tau_s} \\ &= a_s \cdot \exp\left(-j\omega_c \cdot \frac{r_s + r_{\bar{s}}}{c}\right) \end{aligned} \quad (2.2.12)$$

is a constant complex number for both y_s and y_l . Here r_s and $r_{\bar{s}}$ are used to denote the radial distance from transmitter to target, and receiver to target respectively.

As a result of the periodic cardiopulmonary micro-Doppler signal phase modulation, the vital sign carrying propagation paths are time-dependent, and therefore modeled as

$$y_p(t) = a_p \cdot e^{-j\omega_c \tau_p(t)}, \quad (2.2.13)$$

where the signal amplitudes a_p are approximately constant over time due to the small physical amplitude of vital sign motion. Let us assume that the periodic breathing and heartbeat activities are characterized by given mathematical models $s^{(b)}(t)$ and $s^{(h)}(t)$ respectively. Then, the two way radial propagation path length for one reflection point p in the azimuth plane is given by

$$\begin{aligned} \bar{r}_p(t) &= r_p + s^{(b)}(t) \cdot \cos \theta_p + s^{(h)}(t) \cdot \cos \theta_p \\ &\quad + r_{\bar{p}} + s^{(b)}(t) \cdot \cos \theta_{\bar{p}} + s^{(h)}(t) \cdot \cos \theta_{\bar{p}}, \end{aligned} \quad (2.2.14)$$

where θ_p and $\theta_{\bar{p}}$ are the corresponding angles between the normal of the p^{th} reflective surface and the transmitter, and receiver. When the cardiopulmonary vibrations are modeled according to (2.2.9) as sinusoids with frequencies $f_p^{(b)}(t)$ and $f_p^{(h)}(t)$, and amplitudes $u_p^{(b)}$ and $u_p^{(h)}$, the path delay for the p^{th} reflection point is

$$\begin{aligned} \tau_p(t) &= \frac{1}{c} \left(r_p + r_{\bar{p}} \right. \\ &\quad \left. + u_p^{(b)} \cdot \sin(2\pi f_p^{(b)}(t) \cdot t + \psi_p^{(b)}) \cdot (\cos(\theta_p) + \cos(\theta_{\bar{p}})) \right. \\ &\quad \left. + u_p^{(h)} \cdot \sin(2\pi f_p^{(h)}(t) \cdot t + \psi_p^{(h)}) \cdot (\cos(\theta_p) + \cos(\theta_{\bar{p}})) \right), \end{aligned} \quad (2.2.15)$$

where the phase terms $\psi_p^{(b)}$ and $\psi_p^{(h)}$ represent the relative phase of the respiratory and cardiac activities on different points of reflection on the subjects body. It is worth noting that the oscillation frequencies $f_b(t)$ and $f_h(t)$ are time-dependent and may fluctuate based on the excitement and stress felt by the monitored subject. These frequency variations are however usually relatively slow, thus the signal can be assumed stationary within a short time window, but not over long periods. In other words, the signal is quasi-stationary. The stationarity assumption is important for the applied spectral estimation techniques that are discussed in more detail in Chapter 3.

The micro-Doppler effect at the receiver resulting from path delay (2.2.15) is given by

$$\phi_p(t) = \omega_c \frac{\tau_p(t)}{c} + \phi_{p,0}, \quad (2.2.16)$$

where $\phi_{p,0}$ is a phase term comprising of the antenna beampattern angular phase offset and phase shift due to reflection. Clearly, the cardiopulmonary vibration frequency information is preserved in the received signal phase term $\phi_p(t)$. The connection to the instantaneous micro-Doppler frequency shifts can be obtained by differentiating the phase term in time, thus yielding

$$f_{mD,p}(t) = 2\pi f_c \frac{1}{c} \left(u_p^{(b)} f_p^{(b)}(t) \cdot \cos(\omega_p^{(b)}(t) + \psi_p^{(b)}) (\cos(\theta_p) + \cos(\theta_{\bar{p}})) \right. \\ \left. + u_p^{(h)} f_p^{(h)}(t) \cdot \cos(\omega_p^{(h)}(t) + \psi_p^{(h)}) (\cos(\theta_p) + \cos(\theta_{\bar{p}})) \right), \quad (2.2.17)$$

where $\omega_p^{(b/h)}(t) = 2\pi f_p^{(b/h)}(t)$. Evidently the magnitude of the micro-Doppler component depends on the periodic motion amplitudes $u_p^{(b/h)}$ and frequencies $f_p^{(b/h)}(t)$. Moreover, it is also dependent on the chosen carrier frequency f_c and the relative signal angle of arrival at the vibrating target. Consequently, the multipath components may experience different Doppler shifts. However, assuming that there is only one source of vital sign phase modulation, the corresponding frequency information can be recovered using advanced signal processing and spectral estimation techniques. These techniques are presented in Chapter 3.

Estimation of the micro-Doppler frequencies is however not trivial due to the small amplitude of the periodic motion contributing to the low frequency shifts. The weakness of the signal imposes high requirements on the radar hardware quality as well as maximum monitoring range. In order to deal with these limitations, this thesis extends the models and concepts of previous research from SISO continuous wave radar systems into multiple antenna radar systems [13]. Applying multiple antennas at the transmitter and receiver enables the use of various signal enhancement and spatial diversity techniques, thus allowing improved SNR and enhanced reception of the weak vital sign information signal. These techniques are introduced in Chapter 4. The following section introduces a realistic signal propagation model for multiantenna radar systems with both arbitrary and uniform linear array (ULA) receiver geometry.

2.3 Multiantenna Vital Sign Signal Models

The advantages of multiple transmit and receive antennas are widely known in communications engineering. In the application of wireless vital sign monitoring, the multiantenna systems have been proposed to overcome challenges arising from excess motion artifacts, and detecting multiple sources of micro-Doppler motion [4, 5, 12]. While this thesis is focused on the application of single-input multiple-output (SIMO) receiver systems, this Section presents the advantages of having multiple receive antennas, and derives the vital sign signal models employed in the simulations.

2.3.1 Multiantenna Receiver System

The application of multiple receive elements may be used to improve the reliability and performance of radar systems. It has been shown that the multiantenna

systems have more degrees of freedom than single element radars, thus enabling improved angular resolution and parameter identifiability [21]. By using sufficient displacement among the antennas, these systems are able to illuminate the target from different angles and consequently exploit target radar cross section (RCS) diversity in target detection and identification. These widely separated radars achieve performance gains also in detection of slow moving targets due to multidirectional Doppler estimates, as is the case with vital sign monitoring, see Figure 6. Furthermore, frequency modulated radars enable multidirectional delay estimates, allowing high resolution target locationing when the radars are accurately synchronized. [22] Consequently, the main applications of widely separated antennas lie in various surveillance and positioning systems, including air surveillance, military signal intelligence and locationing.

Conversely, colocated antennas with small sensor interelement spacing provide increased radar directivity and higher SNR gains through coherent processing and excellent interference cancelling capabilities [23]. Typical usage of colocated multiantenna systems include target detection and tracking in low signal conditions, direction of arrival (DoA) estimation, and wireless link telecommunications. Due to the beamforming and coherent processing capabilities of colocated receiver antennas, such systems are most suitable for the task of vital sign estimation where low signal to interference plus noise (SINR) conditions are typical. This thesis employs both colocated and widely separated receiver geometries.

The general multiantenna signal model used in this thesis stems from previous research in CW radar vital sign measurements with SISO and MIMO systems [15, 13, 24]. For single antenna systems, the simplified single target CW radar micro-Doppler signal model was presented in the previous Sections 2.2.3 and 2.2.4. It has been shown that such micro-motion based models are fairly good approximations of the actual vital sign process, and can be used for accurate single source vital sign estimation [13]. These prior research models have assumed fairly static measurement conditions with little or no reflected signal amplitude modulation and simple reflection modeling. To improve modeling accuracy, the signal model presented here extends the micro-Doppler vital sign model for multiantenna systems

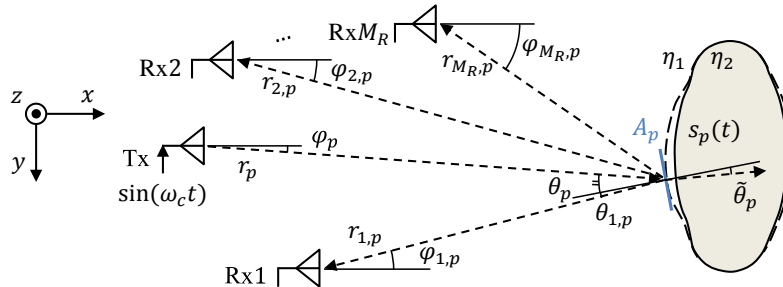


Figure 6: System geometry of a one transmitter and M_R receiver SIMO CW radar with arbitrary receiver geometry observing one source of vital sign micro-Doppler phase modulation. To reduce modeling complexity, it is assumed that all radio elements are observing the same face of the subject, that is $\theta_p, \theta_{m,p} \in (-\pi/2, \pi/2)$ with $m = 1, \dots, M_R$.

with more realistic propagation, reflection and interference modeling.

In order to derive the signal model used in the simulations, a more detailed understanding of the electromagnetic wave propagation losses is required. In addition to the transmitted signal power distribution over space, part of the signal power is lost in every reflection and scattering in the environment. Therefore accurate modeling of the received signal requires more detailed amplitude and reflection modeling, which is presented in the following sections. It is worth noting that in this context signal power losses mean that part of the total transmitted signal power is not available at the receiver end, and is thus lost.

2.3.2 Amplitude Model

The amplitude model for vital sign simulations is based on the general radar equation. An ideal isotropic transmit antenna radiates the transmitted signal power uniformly into space. In other words, the total transmit power P_T at distance r_p from the antenna is distributed over a sphere of size $4\pi r_p^2$. As a result, the signal power experienced at the target with an effective area of A_p is proportional to

$$P_\sigma(r_p, \varphi_p) = \frac{A_p}{4\pi r_p^2} P_T G_T(\varphi_p), \quad (2.3.1)$$

where $G_T(\varphi_T)$ is the transmit antenna gain towards the target at an azimuth angle $\varphi_p \in [-\pi/2, \pi/2]$. Assuming that the target reflects all incoming power as an ideal isotropic radiator, the signal power at a receiver antenna with effective area A_m at a distance $r_{m,p}$ from the target is given by

$$P_m(r_p, r_{m,p}, \varphi_p, \varphi_{m,p}) = \frac{A_p}{4\pi r_p^2} P_T G_T(\varphi_p) \frac{A_m(\varphi_{m,p})}{4\pi r_{m,p}^2}, \quad m \in \{1, \dots, M_R\} \quad (2.3.2)$$

with $\varphi_{m,p} \in [-\pi/2, \pi/2]$, which is the general radar equation. In the case of a non-isotropic antenna, the receiver effective area is a function of the azimuth angle $\varphi_{m,p}$, and it is usually defined via the antenna beampattern gain $G_m(\varphi_{m,p})$ as

$$A_m(\varphi_{m,p}) = \frac{\lambda^2 G_m(\varphi_{m,p})}{4\pi}, \quad (2.3.3)$$

To compute the transmitted signal amplitude attenuation in a simulation, it is assumed that the coordinates of antenna elements and reflection points are known. In the case of a Cartesian coordinate system, the propagation path distances are trivially obtained through the Pythagorean Theorem. Consequently, as the signal power is proportional to the amplitude squared, the time-dependent signal amplitude attenuation coefficient between the transmit and m^{th} receiver element can be approximated with

$$a_{m,p}(t) = \sqrt{P_m(r_p, r_{m,p}, \varphi_p, \varphi_{m,p})}, \quad (2.3.4)$$

where the superscript p specifies the reflection point. Again, by using the small amplitude assumption on cardiopulmonary activity, the attenuation coefficient time-dependency may be omitted.

As the transmitted power attenuates relative to the inverse square of the distance, this constrains the radar maximum operation range after which the low reflected signal power levels at the receiver are no longer detected. [19] Moreover, the propagation path lengths are time-dependent due to the periodic target motion in the vital sign application. To overcome the path loss attenuation problem, many applications utilize directive antennas that, instead of radiating all energy isotropically, focus the transmitted energy on a narrow beam pointing at desired direction. Such narrow beam transmitters enable higher received signal levels if the angular position of the target is known, thus allowing efficient target illumination. However, the amount of received signal energy is also dependent on the signal angle of incidence at the reflective surface.

The model in (2.3.4) relies on a simplifying assumption that all received signal energy is reflected isotropically without losses. In general this is however not the case, but part of the incoming signal energy is absorbed into the target. The amount of absorbed energy depends on the conductive properties of the reflective material and the angle of incidence of the electromagnetic wave. A smaller angle between the signal and the normal of the plane implies that a larger percentage of the inbound signal energy is absorbed. The following section improves the presented attenuation model by including advanced reflection modeling.

2.3.3 Reflection Model

Another common source for electromagnetic signal fading are nonideal reflections where part of the signal energy is absorbed and refracted into nonuniformities in the transmission medium. The reflection of planar wave on a smooth surface is characterized by the Snell's law and Huygens principle. The Snell's law states that there is a linear dependence between the angle of incidence and refraction, and the refractive indices of the interfacing mediums. On the other hand, Huygens principle proposes that every point of an electromagnetic wave is a source of a spherical wave. The combination of these theorems gives a model for absorbent reflection of electromagnetic waves, which is illustrated in Figure 7. While the angle of incidence equals to the angle of reflection, part of the incoming signal energy is absorbed and refracted into the reflecting substance. Furthermore, by applying the Maxwell's equations for electromagnetic wave propagation with perpendicular polarization, it is possible to derive the ratio of reflected signal power to the incoming signal power as

$$\frac{P_2}{P_1} = \left| \frac{\cos(\theta_1) - \eta \cos(\theta_2)}{\cos(\theta_1) + \eta \cos(\theta_2)} \right|^2, \quad (2.3.5)$$

where θ_1 and θ_2 are the angle of incidence and refraction in azimuth plane, $\eta = \eta_2/\eta_1 = \sqrt{\epsilon_2/\epsilon_1}$ is the ratio of refractive indices and ϵ_1 and ϵ_2 are the respective permittivity of primary and secondary substances [25]. Values for specific human tissue permittivity at the 20 GHz frequency range are listed in table 2.

Based on the given permittivity values, it is possible to determine the electromagnetic signal penetration depth δ in human tissues. According to [25], the penetration

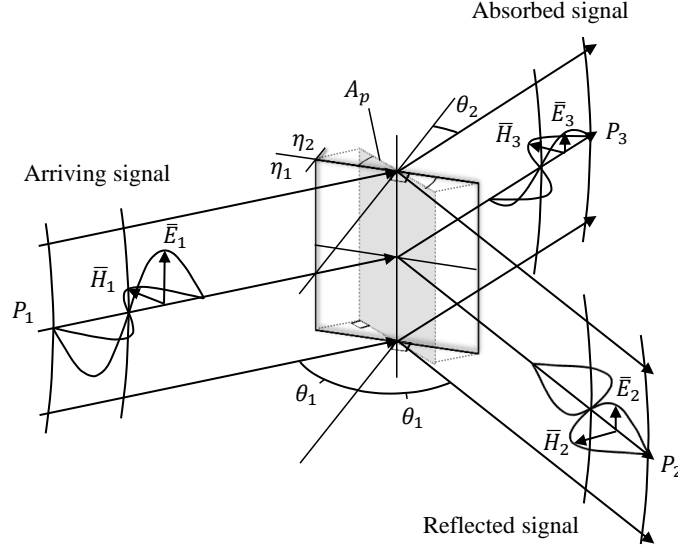


Figure 7: Electromagnetic wave reflection and refraction of a smooth surface with perpendicular polarization, that is the signal electric field is perpendicular to the normal of the reflection plane. Incoming, reflected, and absorbed signal powers are denoted by P_1 , P_2 , and P_3 . Correspondingly, E_i and H_i denote the electric and magnetic field for $i = 1, 2, 3$.

depth for conductors is given by

$$\delta \approx \Im \left[\frac{2\pi}{\lambda} \sqrt{\epsilon(\omega_c)} \right]^{-1}, \quad (2.3.6)$$

where $\epsilon(\omega_c)$ is the frequency dependent permittivity of the substance. By using the value for dry skin given in table 2, the corresponding penetration depth is $\delta_{skin} \approx 0.0016$ m for a 20 GHz radar. Considering that the penetration depth is inversely proportional to the frequency, it is evident that most of the vital signals observed at above 20 GHz frequencies are reflections from the skin layer.

Table 2: Permittivity of specific human tissue measured at $f_c = 20$ GHz. Here permittivity is defined as a complex number $\epsilon(\omega_c) = \epsilon'(\omega_c) - j\epsilon''(\omega_c)$. [26]

Tissue	$\epsilon'(20 \text{ GHz})$	$\epsilon''(20 \text{ GHz})$
Muscle	28.27	22.01
Stomach	36.70	37.53
Skin (Dry)	22.27	15.12
Skin (Wet)	23.67	18.70
Air	1.0006	0

An important observation is that if the angle of incidence is set to $\theta_1 = \theta_2 = 0$, then equation (2.3.5) implies that approximately 48 % of the incoming signal power is reflected back from the skin layer. On the other hand, if the angle is reduced to $\theta_1 = \pi/4$, the amount of reflected power increases to 59 %. However, it should

be noted that the reflection model per se does not take into account the reduced effective area of increasing θ_1 , but this is done in the path loss model. Furthermore, to benefit from the increase of reflected power, the radar system would need to be bistatic. Considering the small physical size of potential platforms to embed vital sign radars, it is reasonable to assume the radar system to be monostatic. Therefore, in order to maximize the received signal power in frontal vital sign measurements, the subject should be facing the radar at broadside.

2.3.4 General Multiantenna Signal Model

The previous sections derived realistic mathematical models for signal amplitude attenuation and reflections. Let us use these models to formulate a multiantenna receiver signal model by combining the respective path loss (2.3.4) and reflection models (2.3.5).

The realistic multiantenna signal amplitude model for a single receiver is given by simply multiplying the two models as

$$a_{m,p} = \sqrt{\frac{A_p}{4\pi r_p^2} P_T G_T(\varphi_p) \frac{A_m(\varphi_{m,p})}{4\pi r_{m,p}^2} \left| \frac{\cos(\theta_p) - \eta \cos(\tilde{\theta}_p)}{\cos(\theta_p) + \eta \cos(\tilde{\theta}_p)} \right|}, \quad (2.3.7)$$

where θ_p and $\tilde{\theta}_p$ are the respective signal angle of incidence and absorption on the target surface, see Figure 6. Now using this amplitude fading model, the different propagation channels can be expressed as a sum of the individual propagation paths. For an illuminated environment with P vital sign emitting reflection points and S interference scatterers, the antenna specific transmission channel after IQ sampling can be modeled as

$$c_m(k) = \sum_{p=1}^P a_{m,p} e^{j\phi_p(k)} + \sum_{s=1}^S a_{m,s} e^{j\phi_s(k)} + a_{m,l} e^{j\phi_l}, \quad (2.3.8)$$

where k denotes the sampling instant, $\phi_p(k)$ is the micro-Doppler phase modulation given in (2.2.16), and $a_{m,l} e^{j\phi_l}$ represents the constant leakage term. In this thesis the phase modulation for static background objects is assumed constant $\phi_s(k)$. However, the model (2.3.8) allows to define any motion model also for the interference scatterers.

In the vital sign application, the SIMO CW radar system uses one transmit antenna to illuminate the vibrating target. The various propagation paths essentially function as individual SISO transmission channels, where the micro-Doppler information is preserved in the channel phase modulation term. Finally, the IQ sampled receiver input vector is given by

$$\mathbf{y}(k) = \mathbf{c}(k) + \mathbf{w}(k), \quad (2.3.9)$$

where $\mathbf{y}(k) = [y_1(k), \dots, y_{M_R}(k)]^T \in \mathbb{C}^{M_R \times 1}$ is a vector of received samples, $\mathbf{c}(k) = [c_1(k), \dots, c_{M_R}(k)]^T \in \mathbb{C}^{M_R \times 1}$ is a vector of channel coefficients defined by (2.3.8),

and $\mathbf{w}(k) = [w_1(k), \dots, w_{M_R}(k)] \in \mathbb{C}^{M_R \times 1}$ are independent samples of white Gaussian noise with variance σ_w^2 . As a result of the compact receiver array geometry, it is clear that unlike the noise components, the vital signals sampled at different antennas are highly correlated. It is exactly this correlation that allows the application of various noise cancelling and signal enhancement techniques, that are used to improve detection and estimation of the vital signs encoded in the micro-Doppler frequencies.

The signal model defined in (2.3.9) is a general model that is applicable for any SIMO CW radar system independent of the array geometry or target range. Other signal models that assume a fixed geometry or a minimum target range do not provide a similar variability as the model presented here. However, by assuming that the target is located far from the receiver, it is possible to simplify the model knowing that the incoming signals behave like planar waves. It should be noted that this simplification does not hold when distance to the target is small compared to the array aperture. While the previously defined model does not rely on such assumptions, it is more versatile in terms of applicability without any loss of modeling accuracy.

Although such alternative models might be inaccurate for some specific measurement setups, however they may provide simplified system signal model. One widely used such signal model in radar engineering is the beamforming signal model. It is designed for modeling returns from far away targets and therefore has a minimum range requirement. When this requirement is met, the model gives a well-established approximation of wave propagation within the array, thus simplifying the ensuing mathematical analysis of the system. As a result, the following section introduces this alternative model, which is thereafter used in the presentation of beamforming techniques.

2.3.5 Beamforming Signal Model

When the target is located far from the radar, the incoming signals can be modeled as planar waves. Consequently, all array elements observe the signal reflections in an approximately same angle of arrival. As a result of the array interelement spacing, the antennas observe different phase shifts due to the differences in signal propagation path time delays. As opposed to the array signal model in (2.3.9), the phase shifts can now be determined without the knowledge of global system transmitter, receiver, and target coordinates. It is enough to know the receiver array internal geometry. Consequently, the application of coherent processing allows the system to determine the signal direction of arrival and apply beamforming or adaptive noise cancelling techniques similarly as with the previous model. Because this model is generally used in radar systems with applications to beamforming, it is known as the beamforming model.

For the receiver array to be able to obtain coherent processing gains, the angle of arrival for the observed signal of interest should be equal across all antenna elements. This implies that the target has to be located far enough from the radar to fulfill the planar wave assumption. The minimum target range is defined by the Fraunhofer

region, which is determined by the array's largest geometric dimension D and the signal wavelength as

$$r_{min} = \frac{2D^2}{\lambda}. \quad (2.3.10)$$

The Fraunhofer region is sometimes referred to as the far field. When the target is located beyond r_{min} , all receiver antennas observe the incoming signal in approximately the same angle of incidence φ . For example, for an optimal ULA receiver with 5 antennas operating at $f = 24$ GHz with $D = (5 - 1) \cdot \lambda/2$, the far field given by (2.3.10) starts at $r_{min} \approx 0.1$ m. However, as further discussions will show, it might be infeasible in this case to fulfill the $\lambda/2$ requirement for antenna spacing.

As a result of the antenna colocation and the far field assumption, the concept of a single propagation path is redefined for the beamforming model. Instead of considering paths relative to individual antennas, one path is now defined as the signal propagation path between chosen array center points at the transmitter and receiver. The center need not be the geometric or physical center. Therefore, as is illustrated in Figure 8, the vital sign modulated phase shifts are also measured relative to the receive array center point.

Following from the assumption that the antenna coordinates $\mathbf{d}_m = [x_m, y_m, z_m]^T$ relative to this center are known for all $m = 1, 2, \dots, M_R$, the corresponding response for the m^{th} antenna is

$$b_{R,m}(\varphi, \vartheta, f) = e^{-j2\pi \frac{f}{c} (\mathbf{d}_m^T \cdot \mathbf{r}(\varphi, \vartheta))} \cdot b_{ref}(\varphi - \tilde{\varphi}, \vartheta - \tilde{\vartheta}, f), \quad (2.3.11)$$

where $\mathbf{r}(\varphi, \vartheta) = [\cos(\varphi) \cos(\vartheta), \sin(\varphi) \cos(\vartheta), \sin(\vartheta)]^T$ is a unit vector in respective azimuth and elevation angles φ and ϑ , $\mathbf{D} = [\mathbf{d}_1, \mathbf{d}_2, \dots, \mathbf{d}_{M_R}]$ is a matrix of antenna coordinates, and $b_{ref}(\varphi - \tilde{\varphi}, \vartheta - \tilde{\vartheta}, f)$ is the angular-frequency response for the single antenna measured relative to its own center and rotation $(\tilde{\varphi}_m, \tilde{\vartheta}_m)$ [27]. The

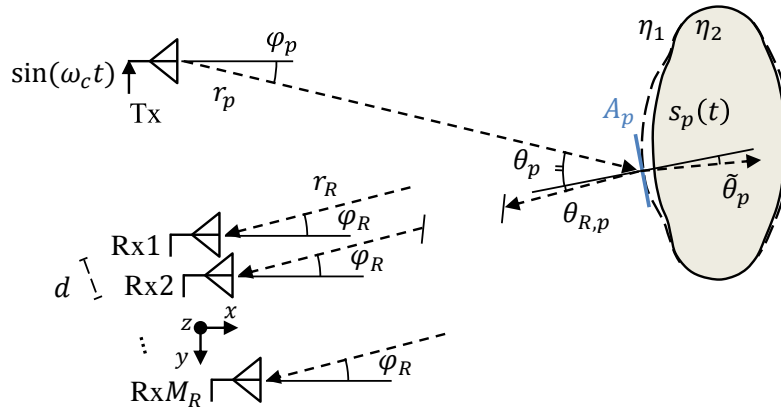


Figure 8: In the beamforming array model, the receive elements form a linear array with d interelement spacing.

response of multiple antennas can be further expressed using vector notation as

$$\mathbf{b}_R(\varphi, \vartheta, f) = \frac{1}{\sqrt{M_R}} \begin{bmatrix} b_{R,1}(\varphi, \vartheta, f) \\ \vdots \\ b_{R,M_R}(\varphi, \vartheta, f) \end{bmatrix} \in \mathbb{C}^{M_R \times 1}. \quad (2.3.12)$$

Here the azimuth and elevation angles are defined with respect to the transmitter and receiver internal coordinate axes, as is shown in Figure 8.

The phase scaling vector defined in (2.3.12) is also known as array response vector since it determines the array transfer characteristics in a specific look direction. The normalization of $1/\sqrt{M_R}$ is used for mathematical convenience to give the array response vector unit norm. Due to the measurement complexity, the antenna specific response vectors are generally not determined individually, but the combined array response is measured using all antennas simultaneously. Such a response includes the mutual coupling of antennas, which is excluded from (2.3.11). For simplicity, let us focus the following analysis on the azimuth plane.

For the specific case of an ULA with isotropic antennas, the array is simply defined by the antenna interelement spacing d . As a result, the array response vector in azimuth plane simplifies to

$$\mathbf{b}_R(\varphi, f) = \frac{1}{\sqrt{M_R}} \begin{bmatrix} e^{-j2\pi \frac{d}{\lambda} \sin(\varphi_R) \left(\frac{-M_R+1}{2} \right)} \\ \vdots \\ e^{-j2\pi \frac{d}{\lambda} \sin(\varphi_R) \left(\frac{M_R-1}{2} \right)} \end{bmatrix}, \in \mathbb{C}^{M_R \times 1} \quad (2.3.13)$$

which is also the array response considered in the vital sign simulations presented in chapter 5 [27]. As with Shannon's theorem for discrete time sampling, in order to avoid spatial aliasing the ULA interelement spacing d should be

$$d \leq \frac{\lambda}{2}. \quad (2.3.14)$$

To minimize redundant sampling and maximize effective array aperture, this parameter is generally set to $d = \lambda/2$. [28] In mobile terminals however, it might be difficult to have $\lambda/2$ spacing or a uniform array geometry due to the limited space available.

After using beamforming techniques to linearly combine the different receiver inputs, the one transmit antenna SIMO system essentially reduces to a SISO channel. With $M_T = 1$, the transmit array response $\mathbf{b}_T(\varphi_T, f)$ is simply a constant complex number. Consequently, the individual SISO channels defined in (2.3.8), may be rewritten as

$$\begin{aligned} \tilde{c}_m(k) = & \sum_{p=1}^P a_{m,p} b_T(\varphi_T, f) e^{j\phi_p(k)} + \sum_{s=1}^S a_{m,s} b_T(\varphi_T, f) e^{j\phi_s(k)} + \\ & a_{m,l} b_T(\varphi_T, f) e^{j\phi_l}, \end{aligned} \quad (2.3.15)$$

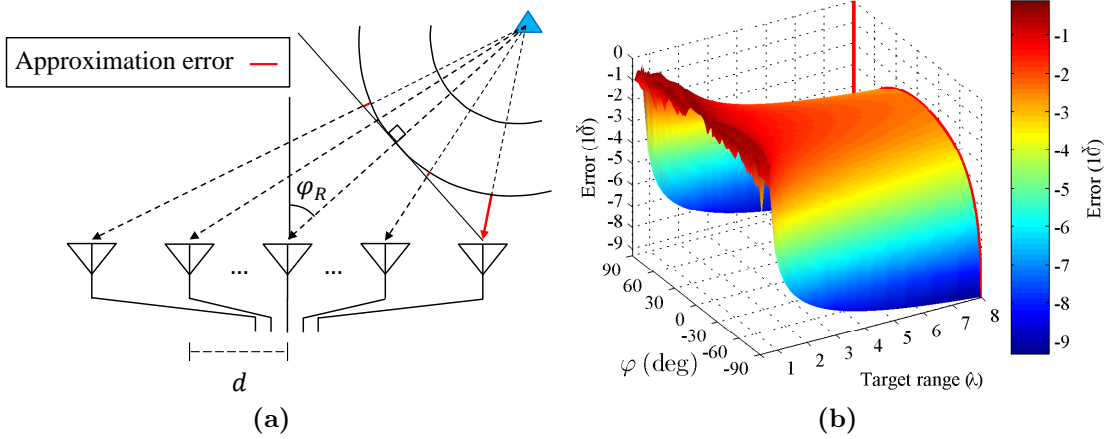


Figure 9: Beamforming signal model error may be significant if the far field assumption is not satisfied. a) Beamforming path length approximation error, and b) corresponding logarithmic error ambiguity function for a 5 element ULA with $\lambda/2$ sensor spacing.

where the micro-Doppler phase modulation is measured relative to the receiver array center point. Thereby, the beamforming channel model is given by

$$\begin{aligned} \mathbf{c}(k) &= \begin{bmatrix} \tilde{c}_1(k) \mathbf{b}_{R,1}(\varphi, f) \\ \vdots \\ \tilde{c}_{M_R}(k) \mathbf{b}_{R,M_R}(\varphi, f) \end{bmatrix} \\ &= \tilde{\mathbf{c}}(k) \circ \mathbf{b}_R(\varphi_R, f), \end{aligned} \quad (2.3.16)$$

where \circ is used to denote the element wise Hadamard product. Finally, the beamformer output at time instant k can be modeled as

$$\mathbf{y}(k) = \tilde{\mathbf{c}}(k) \circ \mathbf{b}_R(\varphi_R, f) + \mathbf{w}(k), \quad (2.3.17)$$

where $w(k)$ is complex white Gaussian noise.

The model (2.3.17) is widely used in array signal processing, but as it is based on the assumption of planar waves, it incorporates a modeling error. The problem is illustrated in Figure 9a, where it can be seen that neglecting the wave front curvature results in an approximation error that is proportional to target range, DoA, and antenna dimensions. The error can be quantified using a logarithmic array response ambiguity function that measures the correlation between the beamforming and true array response for different range and DoA's. The ambiguity function is defined as

$$\mathbf{F}_{amb}(\varphi, r) = \log_{10} (|\mathbf{U}_{bf}^H(\varphi, r) \cdot \mathbf{U}(\varphi, r)| - 1), \quad (2.3.18)$$

where $\mathbf{U}_{bf}(\varphi, r)$ and $\mathbf{U}(\varphi, r) = [\mathbf{u}(\varphi_1, r), \dots, \mathbf{u}(\varphi_N, r)] \in \mathbb{C}^{M_R \times N}$ are matrices with normalized array response vectors (2.3.11) as columns for respective beamforming and true ULA signal models [29]. Figure 9b shows the ambiguity function for a 5 element ULA with $\lambda/2$ sensor spacing. As can be seen, the model error is high

when the target is close to the radar, especially along the broadside at $\varphi = 0$. Nevertheless, when the far field assumption is met, the beamforming model error becomes negligible $\mathbf{F}_{amb}(\varphi, r) < 10^{-2}$ in all look directions. To minimize modeling error in the simulations described in Section 5, the vital sign subject is placed in the far field.

2.4 Conclusion and Remarks of Vital Sign Modeling

As has been shown, wireless noncontact estimation of vital sign activity has an increasing number of applications in various fields ranging from fire rescue to health-care monitoring. Although the concept was already invented in the last century, recent technological advances in wireless communications have inspired new research interest in the topic, as well as decreased the size and cost of the hardware. As presented, the estimation of vital sign activity is based on detecting the periodic cardiopulmonary micro-motion on the subject's body. In many applications, the resulting periodic micro-Doppler is detected by utilizing the simple and inexpensive hardware technology of continuous wave radars. Despite the numerous technological advances, the vital sign estimation problem is generally far from trivial mainly due to the dynamic measurement environment and extremely weak signals. Periodic subject motion or interfering background scattering may render the SINR so low that vital sign detection is no longer feasible. To mitigate the low signal conditions, this chapter presented the use of receiver diversity through multiple receiver antennas.

The introduced multiantenna vital sign signal model extends models presented in previous research papers. Using the derived advanced path loss and reflection modeling, the current signal model enables relatively accurate and realistic data generation for multiantenna vital sign CW radar systems with arbitrary receiver geometry. However, as this thesis is focusing on SISO systems, the introduced signal model is not fully applicable to multi-transmitter MIMO systems. The main challenge with MIMO CW radar systems is the design of orthogonal transmit signals that are distinguishable at the receiver side. While this topic is out of the scope of this thesis, it certainly is an interesting subject for future research considering the vast advantages of MIMO radar systems.

Moreover, it has been shown in [24] that even very similar cardiovascular signatures can be separated with SISO and MIMO systems based on the angle of arrival. Such beamforming and adaptive signal enhancement techniques are presented in chapter 4. With the application of these techniques, the success rate of vital sign estimates in low SINR conditions can be increased significantly. The following chapter introduces signal processing and spectral estimation techniques that can be used to obtain the actual vital sign estimates from the received signal.

3 Signal Processing for Vital Sign Estimation

A typical vital sign measurement is subject to various levels of interference and noise resulting from background objects and receiver system components respectively. In order to improve the initial SNR and the accuracy of the final vital sign rate estimation, it may be desirable to perform various signal pre-processing to suppress or completely remove unwanted components such as DC offset, and high-frequency noise [13]. With high carrier frequencies, the DC compensation is efficiently accomplished by using a nonlinear demodulation technique with adaptive center estimation algorithms. Finally, after signal pre-processing, the respiratory and cardiac rates may be estimated using any given high-resolution spectral estimation technique. To obtain the full spatial diversity gain in multiantenna systems, there is an additional step of combining the different inputs coherently. However, these techniques are presented in detail in Section 4.

This section begins by describing the structure of the micro-Doppler phase modulated signal at the receiver. The received signal model was defined in Section 2.3. By analyzing the signal frequency domain characteristics, it will be shown that the cardiopulmonary rates cannot be estimated by directly applying spectral estimation methods on the received signal. Therefore, the section describes typically used signal demodulation techniques that are used to recover the micro-Doppler phase information required in accurate vital sign estimation. Finally, the section presents different approaches for estimating the vital sign frequencies from the received signal data.

3.1 Received Signal Structure

The structure of the signal at different receiver antennas defined in (2.3.9) is illustrated in Figure 10. The periodic vital sign micro-Doppler phase modulation observed at each antenna forms an arc on the IQ-plane, with a center corresponding to the respective DC-offset due to static reflection and leakage components. The length of the arc depends on both the radar carrier frequency, as well as the amplitude of the physical cardiopulmonary motion, as was shown in (2.2.17) for the magnitude of the micro-Doppler frequency shift. As a result of the antenna displacement, each receiver observes a distinct phase modulation offset corresponding to the respective propagation path delay and radial motion component of an individual target, see Figure 10a.

The radius of the vital sign phasor represents the antenna specific signal amplitude defined in (2.3.7), which is further used in defining the SNR at the m^{th} receiver as

$$\text{SNR}_m \text{ (dB)} = 10 \cdot \log_{10} \frac{a_m^2}{\sigma_{a_m}^2}, \quad (3.1.1)$$

where a_m^2 is the signal amplitude in the IQ-plane, and $\sigma_{a_m}^2$ is the radial variance of the arc. The presence of only one vital sign micro-Doppler phase modulating source is assumed. Although it is typical to have reflections from multiple micro-Doppler sources, for simplicity let us assume only one source of vital signs in what follows.

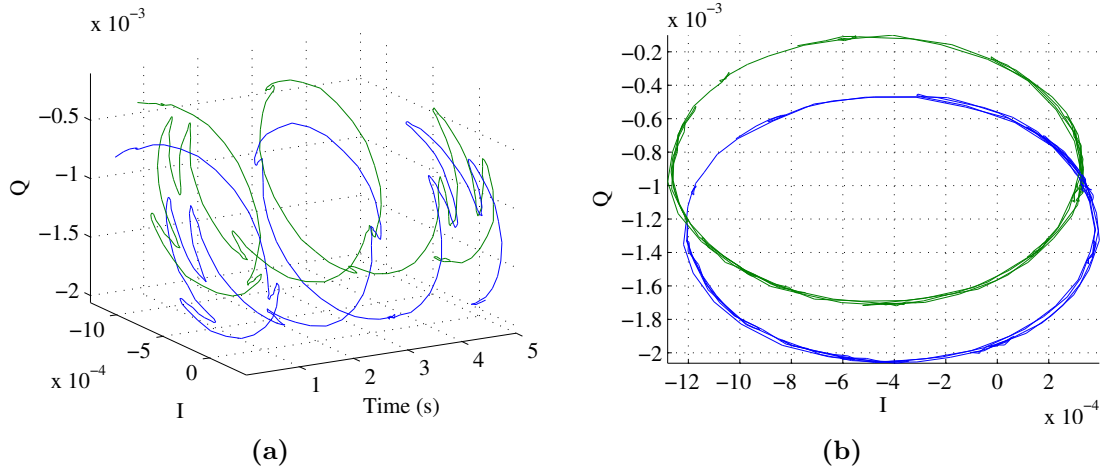


Figure 10: The vital sign micro-Doppler effect modulates the signal phase. IQ channel output of two receivers observing one vital sign target (SNR = 40dB), a) signal in IQ-time space, and b) in IQ plane.

Without any pre-processing, direct estimation of the vital sign rates from the received signals would be difficult. This is due to the signal frequency characteristics, which contain even and odd order harmonics of the fundamental vital sign frequencies [6, 30]. Although the power of these harmonic terms generally decays with higher order multiples, the third and fourth breathing harmonics are typically close to or overlap the heartbeat frequencies. Moreover, due to the small amplitude of cardiac activity, these breathing harmonics have approximately same power as the fundamental heartbeat frequency. In order to perform reliable vital sign parameter estimation, these harmonic terms need to be removed. The problem may be illustrated by analyzing the vital sign reflections observed by a single receiver system, see Figure 11. In this example, both the breathing and heartbeat frequency information is masked by the strong breathing harmonics. To overcome the problem of interfering harmonics, the following section gives an overview of two commonly used signal demodulation techniques.

3.2 Complex Signal Demodulation

The purpose of signal demodulation is to convert the received data into a form that enable reliable vital sign rate estimation. Essentially this means extracting the signal phase, which contains the quasi-periodic micro-Doppler information of vital sign activities. However, obtaining the phase information may be difficult especially in the presence of large and unwanted DC offsets that shift the signal center, see Figure 10b. That is why various demodulation techniques require DC cancellation before estimating the micro-Doppler phase information.

This section presents and evaluates two typically applied complex signal demodulation techniques known as linear and nonlinear demodulation. These techniques are good examples, as they differ in both removing the DC offset, and obtaining the

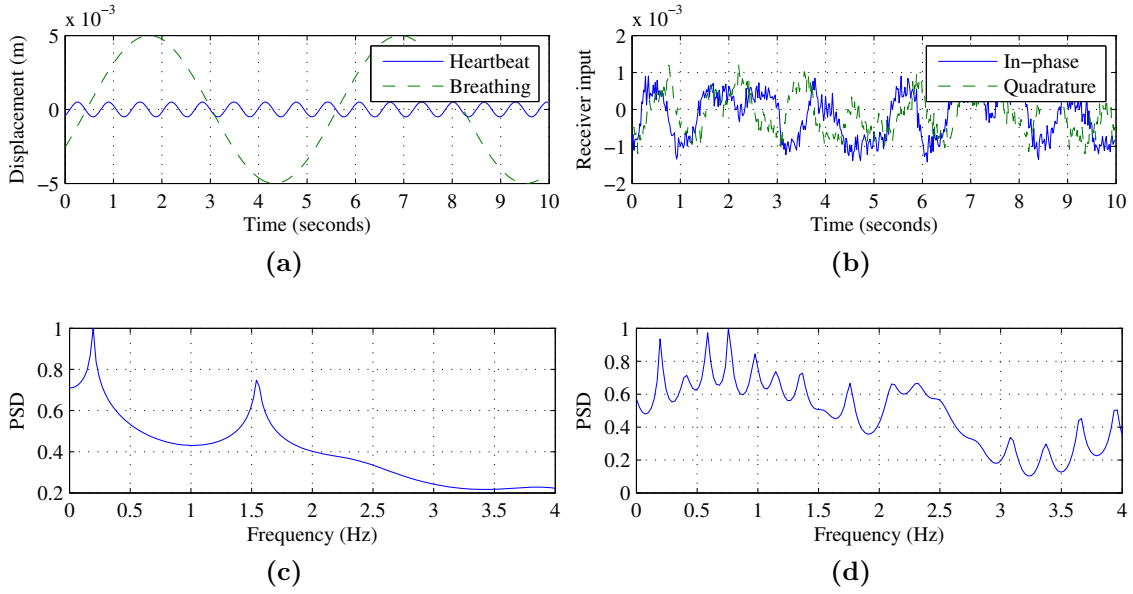


Figure 11: Time and frequency analysis of micro-Doppler modulated signal at one receiver, a) Cardiopulmonary activity, b) receive IQ-input signals, c) true vital sign frequencies, and d) spectrum estimate of DC-compensated receive data. The breathing harmonics make estimation of the heartbeat frequency difficult.

estimate of the signal phase. Furthermore, it can be shown that although the linear demodulation technique has a lower computational complexity, the accuracy of the nonlinear demodulation technique is required for reliable micro-Doppler estimation with high frequency systems or detecting large amplitude vibration.

3.2.1 Linear Demodulation

Linear demodulation is a simple and computationally efficient way of extracting the phase information at low carrier frequencies. More importantly, removing the DC offset may be implemented simply by using a time average, thus requiring no high complexity center estimation and tracking algorithms like in nonlinear demodulation. As was shown in (2.2.17), the arc length is proportional to the chosen carrier frequency. Consequently, using lower carrier frequencies yields smaller arc lengths, thus enabling the application of principal component analysis in signal phase estimation. It has been shown in [31] that when the arc length is less than 0.13 radians, linear demodulation can achieve a high degree of accuracy in extracting the signal phase information.

Before linear demodulation, the data DC offset need to be compensated. This is accomplished by simply averaging the data over a short temporal window, and removing the average from the given samples. For signal fulfilling the WSS requirement, it is enough to compute average once, and use it for all future samples to remove the DC offset. However, in the application of vital sign monitoring with nonstationary signals, the DC offset may change over time due to random body

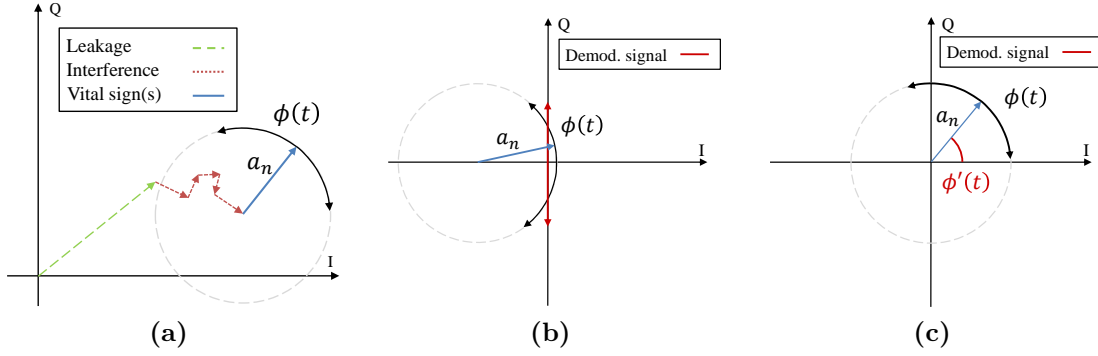


Figure 12: Extraction of Doppler information from the IQ sampled data. a) Received signal, b) linear demodulation, and c) nonlinear demodulation.

movement, or motion interference from the environment. As a result, the signal needs to be averaged with regular intervals. After removing the offset, the DC compensated arc is rotated parallel to the Q-axis, where after the demodulated signal is simply obtained as the Q-component of the rotated data, as is illustrated in Figure 12b. The rotation of the arc is performed by multiplying the data with the transpose of the eigenvector matrix of the data sample covariance matrix.

The accuracy of linear demodulation decreases by increasing the arc length. The reason for this lies in the loss of phase information with long arc lengths, or circles, when only the Q-component of rotated data is used for further processing. In order to preserve all phase information, a more advanced demodulation approach known as nonlinear demodulation is required.

3.2.2 Nonlinear Demodulation

Nonlinear demodulation preserves the complete phase information by applying center tracking algorithms for DC offset compensation. When the circle center is estimated and removed from a sample window, the cardiopulmonary phase information can be recovered as the phase of the resulting complex phasor. This technique is also known as arctangent demodulation.

In contrast to linear demodulation, the nonlinear demodulation applies center estimation algorithms to track the signal DC component, which is the center of the circle. The center is estimated using the nonlinear LS method and Levenberg-Maquardt algorithm for circle fitting, which is an extension of the iterative Gauss-Newton method [32, 33]. For accurate phase recovery, the center estimate needs to be updated periodically to compensate for random subject body movement and temporal background interference. Due to the adaptive circle fitting, the computational cost of nonlinear demodulation is significantly higher than with linear demodulation applying simple time-averaging. Furthermore, the complexity of nonlinear demodulation is increased in multiantenna systems since each receiver observes a different DC offset, thus the center estimation need to be done individually for all receivers.

After center estimation, the signal DC component is removed to translate the vital sign phasor center to the origin of the IQ-plane. Consequently, the demodulated

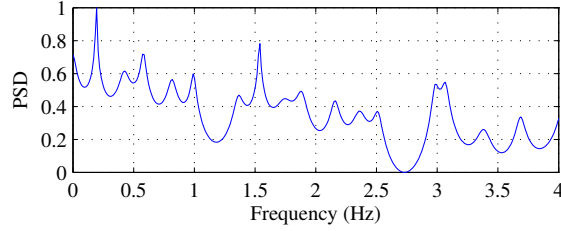


Figure 13: Applying adaptive center tracking algorithms with nonlinear demodulation allows extraction of the complete micro-Doppler phase information. The breathing and heartbeat frequencies are visible as the two largest spectrum peaks at approximately 0.2 Hz and 1.5 Hz respectively, as compared to Figure 11d where heartbeat component was overpowered by breathing harmonics.

signal is obtained by

$$\phi'(t) = \arctan \left(\frac{\Im[y'(t)]}{\Re[y'(t)]} \right), \quad (3.2.1)$$

where $y'(t)$ is the DC compensated version of the signal (2.2.11) at one receiver, as illustrated in Figure 12c. It should be noted that the micro-Doppler phase information is now completely preserved in $\phi'(t)$, thus allowing accurate estimation of the instantaneous micro-Doppler frequencies. Due to the arctan-operator, the nonlinear demodulation is sometimes referred to as arctan demodulation.

The nonlinear demodulation technique with dc offset compensation can achieve a high degree of accuracy, particularly with long arc lengths [31]. The advantage is illustrated in Figure 13, which shows the absence of the harmonic terms that were interfering the frequency spectrum of the unprocessed signal, see Figure 11d. However, the total computational complexity of nonlinear demodulation is higher than with linear demodulation, due to the center estimation algorithms. While nonlinear demodulation is necessary when using high carrier frequencies, the effects of increased complexity can be reduced by updating the center estimate infrequently every two or three seconds, depending on the second order statistics of the observed micro-Doppler modulation.

3.3 Overview of Spectral Estimation

The basic spectral estimation problem can be formulated as follows: From a finite set of given samples $\mathbf{y} = [y(1), y(2), \dots, y(N)] \in \mathbb{C}^{N \times 1}$ of a second-order stationary random process, obtain an estimate $\hat{\phi}(\omega)$ for the power spectral density (PSD) [34]. Many modern applications use spectrum analysis to determine hidden periodicities in the data. The information of the power distribution is used in applications such as speech analysis, radar and sonar systems, seismology, and medicine. In the ideal case, the obtained spectral estimate would equal to the true spectrum of the data. However, this is not usually possible due to limitations on the amount of available data samples. Typically the main reason for limited sample space is that the processed data may be considered second-order stationary for only a short period

in time. Also, in applications such as radar monitoring, the time available for sampling is usually limited, since it accumulates the total delay for target detection.

Different spectral estimation methods are typically classified as nonparametric or parametric methods, depending on the a priori assumptions of the signal generating process. As the name already implies, nonparametric methods require no prior information of the functional form of the studied signal, but they rely solely on the definitions of power spectral density in determining the spectral estimate, denoted by $\phi(\omega)$. That is, they can be applied to almost any data set without the need of parameterizing or modeling the data in advance. In contrast, if a mathematical model of the signal generating sequence is available, this information can be utilized by the parametric methods to provide estimates with higher statistical accuracy when compared to the nonparametric methods. In addition to the nonparametric and parametric methods, a third approach to spectral estimation is to use a bank of narrow selective bandpass filters for determining power distribution over respective frequency bands. This section presents some of the typically used spectral estimation methods from each of these three classes with a focus on the current vital sign application.

3.3.1 Periodogram

The periodogram is a simple and straight forward approach to nonparametric spectral estimation. The method relies solely on the definition of the PSD by averaging the signal energy spectral density over the observed discrete-time data samples $y(k), k \in \{1, \dots, N\}$ as

$$\hat{\phi}_p(\omega) = \frac{1}{N} \left| \sum_{k=1}^N y(k) e^{-j\omega k} \right|^2 \quad (3.3.1)$$

However, the simplicity of the formulation has its drawbacks in terms of resolution and statistical properties of the estimator $\hat{\phi}_p(\omega)$.

The frequency resolution, that is the ability to resolve closely spaced spectra, of the periodogram is mainly limited by the amount of available samples N . At best, the frequency resolution of the periodogram method equals to the reciprocal of the temporal width N of the rectangular window. This translates to a spectral resolution of approximately $1/N$ at the -3 dB points. [35] Furthermore, when N grows to infinity, it is easy to verify that the periodogram is an asymptotically unbiased spectral estimate [34]. However, with a finite sample space, the estimate $\hat{\phi}_p(\omega)$ contains a bias which results from the leakage and smoothing of the spectra due to windowing. The main limitation of the periodogram however does not lie in its frequency resolution, but its large statistical variance.

By analyzing the statistical properties of the estimated spectrum, it can be shown that the periodogram is not a consistent estimate of the true spectrum $\phi(\omega)$ [35], [34]. Although the finite sample variance of $\hat{\phi}_p(\omega)$ may be difficult to establish in specific cases, the asymptotic variance in the case of Gaussian white noise is

$$\lim_{N \rightarrow \infty} \text{var}\{\hat{\phi}_p(\omega)\} = \phi^2(\omega). \quad (3.3.2)$$

Consequently, the periodogram does not converge to the true power spectrum density. [35]

Many other classical nonparametric estimation methods that are based on the periodogram like the Bartlett and Welch method, attempt to decrease the statistical variance at the cost of reducing the frequency resolution. For a detailed description of these methods, the reader is referred to [34] and [35]. Nevertheless, the simple and fast implementation of periodogram through the use of fast Fourier transforms (FFT) makes it a useful tool in nonparametric spectral estimation. Another well-known approach to increasing the statistical accuracy of the spectral estimate, is to apply data-dependent bandpass filtering known as the Capon method described in the following section.

3.3.2 Capon

Capon is a nonparametric high resolution spectral estimation method applying optimized finite impulse response (FIR) filters in the estimation process [36]. Unlike many other nonparametric methods like periodogram and refined filter-bank approach (FBA), the Capon method adapts to the available data in order to provide more accurate spectral estimates [34].

By definition, the Capon uses one FIR bandpass filter $\mathbf{h} = [h_0, h_1, \dots, h_m]^H \in \mathbb{C}^{(m+1) \times 1}$ to process the N data samples in small subsequences of size $m + 1$ as

$$\begin{aligned} y_h(t) &= \sum_{k=0}^m h_k y(t-k) \\ &= \mathbf{h}^H \begin{bmatrix} y(t) \\ y(t-1) \\ \vdots \\ y(t-m) \end{bmatrix} = \mathbf{h}^H \mathbf{y}(t). \end{aligned} \quad (3.3.3)$$

The spectrum estimate is obtained by minimizing the variance of the filtered output sequence $E\{|y_h(t)|^2\} = \mathbf{h}^H \mathbf{R} \mathbf{h}$, while still constraining the filter to pass the passband frequencies ω undistorted. This results in an optimization criterion for the filter coefficients as

$$\min_{\mathbf{h}} \mathbf{h}^H \mathbf{R} \mathbf{h} \quad \text{subject to} \quad \mathbf{h}^H \mathbf{a}(\omega) = 1, \quad (3.3.4)$$

where \mathbf{R} is the autocorrelation matrix of the data sequence $\mathbf{y}(t)$, and $\mathbf{a}(\omega) = [1, e^{-j\omega}, \dots, e^{-jm\omega}]^T \in \mathbb{C}^{(m+1) \times 1}$ is the Vandermonde type Fourier transform vector. It is shown in [34], that the solution to this problem is given by

$$\mathbf{h} = \frac{\mathbf{R}^{-1} \mathbf{a}(\omega)}{\mathbf{a}^H(\omega) \mathbf{R}^{-1} \mathbf{a}(\omega)}. \quad (3.3.5)$$

If this optimal filter is substituted into the expression for the variance in (3.3.4), the total power over the passband centered at ω is given by

$$\sigma_{y_h}^2 = E\{|y_h(t)|^2\} = \frac{1}{\mathbf{a}^H(\omega) \mathbf{R}^{-1} \mathbf{a}(\omega)} \quad (3.3.6)$$

Finally, the minimum variance spectral estimate is obtained by dividing the total power by the bandwidth of the adaptive filter of length $m + 1$, and replacing the autocovariance matrix with its finite sample estimate

$$\hat{\mathbf{R}} = \frac{1}{N - m} \sum_{t=m+1}^N \begin{bmatrix} y(t) \\ \vdots \\ y(t - m) \end{bmatrix} \begin{bmatrix} y^*(t) & \dots & y^*(t - m) \end{bmatrix}. \quad (3.3.7)$$

Hence the Capon spectral estimate is given by

$$\hat{\phi}(\omega) = \frac{m + 1}{\mathbf{a}^H(\omega) \hat{\mathbf{R}}^{-1} \mathbf{a}(\omega)}. \quad (3.3.8)$$

While it is clear from (3.3.8) that the FIR filter is data dependent through the autocovariance matrix, the expression implicitly assumes that its inverse $\hat{\mathbf{R}}^{-1}$ exists. In order for $\hat{\mathbf{R}}$ to be invertible, the value of m has to be chosen appropriately to fulfill the condition $m < N/2$ [34]. This inequality also sets a limit to the resolution achievable by the Capon method as m determines the length of the adaptive filter. On the other hand, increasing m for higher resolution will decrease the statistical accuracy of $\hat{\phi}(\omega)$, as there are less samples for estimating $\hat{\mathbf{R}}$. Hence, the choice of m is a tradeoff between variance and resolution of the estimate. Moreover, it is worth noting that the estimator computational complexity depends also on the value chosen for m , which is important especially for applications with restricted processing capabilities.

Based on empirical evidence, it has been shown that the Capon method has a higher statistical resolution than the periodogram and its low variance extensions [34], [37]. The performance of the Capon spectrum estimator is attributed to the higher statistical stability and the resolution improvement gained through data-dependent filter coefficient optimization. The statistical stability of the estimator is especially important in applications with quasi-stationary signals like vital sign estimation, where the signal statistics may vary with time. The following section presents a low complexity fast recursive algorithm for computing the Capon spectral estimate, which is eventually applied for rate estimation in the conducted experiments presented in Chapter 5.

3.3.3 Fast Recursive Capon Estimation

The main limitation of the high resolution minimum variance Capon estimation method (3.3.8) is the high computational cost involved in inversion of the covariance matrix $\hat{\mathbf{R}}$. Moreover, the inversion needs to be done every time a new block of samples is available. This results in excessive use of computational resources, especially with close to stationary signals that yield only small changes to consecutive instances of $\hat{\mathbf{R}}$. However, the computational complexity of Capon can be reduced by formulating the spectrum estimate into a recursive structure, and thus avoiding the need for direct matrix inversion on each iteration.

When the covariance matrix is estimated as an exponentially weighted sample average as

$$\hat{\mathbf{R}}(k) = \sum_{l=0}^k \lambda^{k-l} \mathbf{y}(l) \mathbf{y}^H(l), \quad (3.3.9)$$

where $\lambda \in (0, 1)$ is a forgetting factor, the covariance matrix can be computed using the recursion

$$\hat{\mathbf{R}}(k) = \lambda \hat{\mathbf{R}}(k-1) + \mathbf{y}(k) \mathbf{y}^H(k). \quad (3.3.10)$$

Consecutively, by applying the matrix inversion lemma [34] to (3.3.10), it has been shown in [38] that the covariance matrix can be inverted using the following recursion

$$\hat{\mathbf{R}}^{-1}(k) = \lambda^{-1} \hat{\mathbf{R}}^{-1}(k-1) - \lambda^{-2} \varphi(k) \mathbf{g}'(k) \mathbf{g}'^H(k), \quad (3.3.11)$$

where $\mathbf{g}'(k) = \hat{\mathbf{R}}^{-1}(k-1) \mathbf{y}(k)$ denotes the a priori Kalman gain vector, and

$$\varphi(k) = \frac{\lambda}{\lambda + \mathbf{y}^H(k) \hat{\mathbf{R}}^{-1}(k-1) \mathbf{y}(k)}. \quad (3.3.12)$$

Thereafter, the recursion for the spectrum estimate at angular frequency ω can be derived by pre- and post-multiplying (3.3.11) from both sides by \mathbf{a}^H and \mathbf{a} , thus yielding to

$$\hat{\phi}(\omega, k) = \lambda^{-1} \hat{\phi}^{-1}(\omega, k-1) - \lambda^{-2} \varphi'(k) |v_g(k)|^2, \quad (3.3.13)$$

where $\varphi'(k) = (1 - \lambda)^{-1} (m+1)^{-1} \varphi(k)$, and $v_g = \mathbf{a}^H \mathbf{g}'(k)$ [38].

The complexity of the recursive Capon spectral estimate (3.3.13) can be further reduced by computing the product $v_g = \mathbf{a}^H \mathbf{g}'(k)$ recursively through linear prediction [38]. The resulting total complexity of the fast recursive algorithm for N samples evaluated at $K = N = m+1$ frequency bands is $36N^2 + 15N$ multiplications, whereas the corresponding complexity for the direct Capon spectrum (3.3.8) is $4N^3 + 5N^2$ multiplications [38]. Clearly, the fast recursive Capon method is computationally less expensive, which is an important criterion for applications like vital sign estimation where the spectrum needs to be estimated frequently.

3.4 Time-Frequency Analysis

Another approach to estimating the instantaneous frequency content of a signal is to use two-dimensional time-frequency distributions (TFDs) to represent the power distribution simultaneously in both time and frequency domains. While the periodogram and Capon methods provide estimates of the signal spectrum evaluated over a window in time, the TFDs can be used to convey a time-frequency description of how the spectrum content is changing over time. That is, the latter allows us to determine what frequencies existed at a particular time instant, whereas the former only shows which frequencies were present in the signal. This section gives a brief overview of the general time-frequency tools and their application to the analysis of signal micro-Doppler components.

3.4.1 Short-Time Fourier Transform

Accurate vital sign rate estimation with pure spectrum estimation methods like the periodogram and Capon, require repetitive computation of the frequency spectrum. For example, in order to update the instantaneous heart rate estimate every second, the Capon MVDR spectrum need to be computed every second to determine what was the heartbeat frequency at a given time instant. Thereafter, by truncating these spectra after one another in the time domain, it is possible to construct a time-frequency spectrum that indicates how the heart rate varied over time. This is essentially the same approach used in the two-dimensional time-frequency distribution tool known as the short-time Fourier Transform (STFT); break up the signal into small time segments and analyze their frequency content separately [39].

In the construction of the STFT, the signal of interest is multiplied by a window function $w(t)$, centered at t , to obtain a short snapshot of the original signal as

$$y_t(\tau) = y(\tau)w(\tau - t), \quad (3.4.1)$$

where τ is the integration time. Since this snapshot identifies the signal around time t , then its Fourier transform reflects the respective frequency distribution. Hence, the STFT is defined as

$$Y(t, \omega) = \frac{1}{\sqrt{2\pi}} \int e^{-j\omega\tau} y(\tau)w(\tau - t)d\tau, \quad (3.4.2)$$

and the corresponding time-frequency distribution is

$$S(t, \omega) = |Y(t, \omega)|^2. \quad (3.4.3)$$

The frequency resolution of STFT is determined, according to the time-bandwidth product, by the chosen window shape and length $w(t)$. If the window is rectangular, the STFT coincides with a series of truncated periodograms. As with periodogram, the choice of window length is always a compromise between resolution and statistical variance. Taking a shorter window in time increases the temporal resolution, but this degrades the resolution in frequency domain [39]. Figure 14a illustrates the application of STFT to estimating the micro-Doppler components from a vital sign modulated CW radar signal. The applied window was a Hanning window of length 3 seconds, giving a compromise between resolution and statistical accuracy. Although the slowly varying breathing component is visible in the time-frequency distribution of Figure 14a, the resolution is not enough to perform accurate estimation of the heartbeat frequencies in the signal. In order to increase the resolution in the time-frequency domain, the following section presents the Wigner distribution.

3.4.2 Wigner-Ville Distribution

The Wigner-Ville distribution (WVD) is another TFD widely used in signal processing for high-resolution time-frequency spectrum analysis. The distribution was

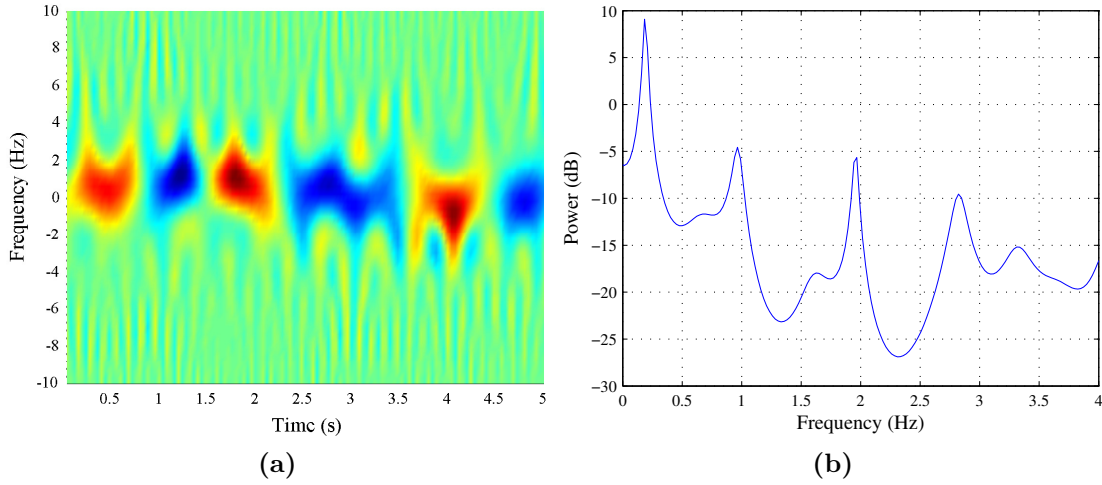


Figure 14: a) Time-frequency distribution of a vital sign modulated CW radar signal using the STFT with a 3 second Hanning-window, b) frequency spectrum of the 5 second data. Heartbeat frequency at 2 Hz may not be detected.

originally defined by Wigner in quantum mechanics, and later applied to signal processing by Ville [40]. For a signal $y(t)$, the WVD is given by

$$W(t, \omega) = \frac{1}{2\pi} \int_{-\infty}^{\infty} y(t + \tau/2) y^*(t - \tau/2) e^{-j\omega\tau} d\tau. \quad (3.4.4)$$

This may be interpreted as to multiplying the signal with a time-reversed copy of it, and integrating the product over time. Whenever the signals overlap at the integration time instants, the WVD will have nonzero density. As a result, the WVD may contain contribution from signals present at times $t \pm \tau/2$, even if there was no signal present at time t . Such contributions are called cross term interference, as they do not represent the true characteristics of the observed signal. Moreover, when integrating over infinite time signals, there will be always overlap, thus the WVD is heavily crippled by noise resulting from the cross terms.

The problem with the pure Wigner distribution is that it weights all past and future time instants equally. In order to suppress the effect of cross term noise from signals far in the past and future, the WVD is windowed to emphasize signals around time t , like in the case of STFT. This windowed WVD is known as pseudo Wigner-Ville distribution (PWVD), and defined as

$$\begin{aligned} W(t, \omega) &= \int_{-\infty}^{\infty} w(\tau/2) w^*(-\tau/2) y(t + \tau/2) y^*(t - \tau/2) e^{-j\omega\tau} d\tau \\ &= \frac{1}{2\pi} \int_{-\infty}^{\infty} Y(t, \omega + \theta/2) Y^*(t, \omega - \theta/2) d\theta. \end{aligned} \quad (3.4.5)$$

The windowing improves the resolution of the WVD by making it more local, but on the other hand the PWVD does not have the same marginal distribution properties of the WVD [39]. It has been further shown in [41], that the effects of cross terms

can be reduced, or even completely removed by introducing a narrow frequency window $P(\theta)$ into (3.4.5), thus yielding the smoothed pseudo Wigner-Ville distribution (SPWVD)

$$SW(t, \omega) = \frac{1}{2\pi} \int_{-\infty}^{\infty} P(\theta) Y(t, \omega + \theta/2) Y^*(t, \omega - \theta/2) d\theta. \quad (3.4.6)$$

The accuracy of the SPWVD is shown in Figure 15a, where the method is applied to the same signal as in Figure 14a with the STFT. Now the heartbeat micro-Doppler contribution is clearly visible, and the rate can be estimated by running the density peak values through any frequency estimation method.

Although many of the TFD may provide a high time-frequency resolution of the signal, they generally have the disadvantage of high computational complexity. However, as a result of windowing in the frequency domain, the discrete time version of the SPWVD, which is given by

$$SW(k, m) = \sum_{i=-L}^L P_d(i) Y(k, m+i) Y^*(k, m-i), \quad (3.4.7)$$

where $P_d(i)$ is the discrete window of length $2L+1$, can be implemented efficiently using recursive FFT in computing $Y(k, m \pm i)$ [41]. The fast implementation together with the high time-frequency resolution provided by the SPWVD, make it a useful tool especially in vital sign rate estimation. However, for simplicity of implementation, the simulations presented in Section 5 applied the high resolution fast MVDR Capon spectral estimate in vital sign rate estimation.

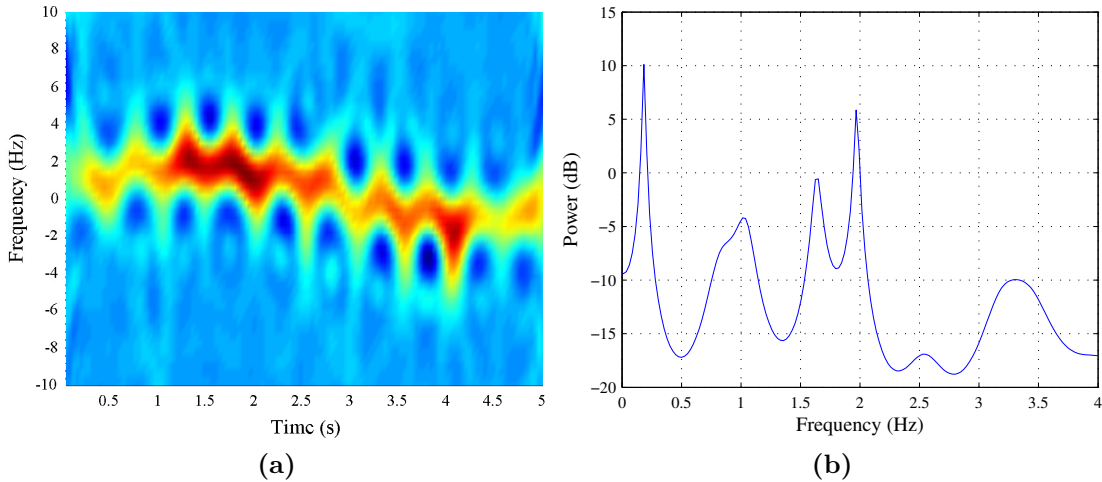


Figure 15: Application of the SPWVD to the same vital sign modulated signal as in Figure 14a. The heartbeat frequency at approximately 2 Hz is easily recovered as the second largest spectrum peak.

3.5 Discussion on Suitable Algorithms

One of the main considerations in choosing appropriate algorithms for vital sign estimation is to maximize the gain and statistical accuracy of the chosen signal processing methods. There is an obvious driver for such thinking, since estimation of the cardiopulmonary activities is difficult to begin with due to the weakness of the modulated micro-Doppler components. However, choosing the signal processing algorithms is always balancing with the tradeoff between output gain and computational complexity. In accordance to the previous sections, the high-resolution and high-accuracy processing methods typically have also the highest computational costs. This section gives a brief discussion on selecting suitable algorithms for vital sign monitoring, with the focus on systems with limited computational resources such as battery operated mobile devices.

The first consideration is the choice of a suitable pre-processing algorithm for signal demodulation and DC compensation. This decision depends more on the CW radar specifications than the computational savings. That is because the nonlinear demodulation techniques applying center estimation and tracking algorithms is typically necessary in high-frequency operated systems. Although the linear demodulation achieves great computational savings compared to the nonlinear one, it is unable to preserve complete micro-Doppler phase information with long arc lengths in the IQ-plane, as was seen in Section 3.2. However, it has been shown that for vital sign estimation, the linear demodulation is as accurate as the nonlinear demodulation with low frequency 2.4 GHz systems.

While the demodulation technique is mainly determined by the system specifications, significant computational savings can be achieved in choosing the vital sign rate estimation algorithms, since they are run frequently. From the presented spectral estimation algorithms, the periodogram would be the choice in minimizing processing cycles, as it can be implemented simply using FFT. On the other hand, with a slightly increased computational cost, the fast recursive Capon method provides minimum-variance high-resolution spectral estimates. Thereby, the latter method would also be applicable in systems with limited processing power.

Although the TFD tools have a considerably higher complexity, partly due to the overhead of pre-computing the FFTs, they should not be neglected. It has been shown that these techniques may provide a high resolution in both time and frequency domains [39, 42]. As a result, if the monitoring system has the necessary resources and high-resolution monitoring is necessary, for example in diagnosing heartbeat abnormalities such as arrhythmia, then the SPWVD may be the suitable rate estimation tool. However, with battery operated monitoring devices with on-board computation, one should consider the lower complexity algorithms. Moreover, one should also consider the software implementation complexity of the considered algorithms, since many software architectures may not have ready libraries for such specific needs.

4 Multiantenna Adaptive Signal Enhancement Techniques

To obtain the full diversity gain of using multiple receive antennas, the different input signals need to be combined coherently. As a result of the quasi-stationarity of the vital sign modulated micro-Doppler, the use of basic signal enhancement techniques, such as fixed linear filtering or channel equalization is not feasible. These techniques are generally based on knowledge of the second-order statistics of the observed signals, but like many other signal processing application, this information is not a priori available in vital sign estimation. The temporal variations in the multiantenna propagation channels call for signal enhancement techniques that are time adaptive, and thus enable real time tracking of channel and signal variations.

This chapter begins by giving a brief overview of related work on vital sign monitoring with multiantenna systems. Thereafter, the chapter presents adaptive array signal enhancement techniques that can be used to improve receiver SINR in a multiantenna receiver system. The firstly presented signal processing method is a novel application of adaptive noise cancellation techniques that utilize various algorithms in adaptive filtering. The following section introduces spatial methods, and the last section briefly discusses the application of independent component analysis (ICA) in vital sign estimation. All the presented techniques rely on the basics theories of adaptive filtering and statistical signal processing. The adaptive filtering based methods are used to suppress wideband additive noise that is masking the narrowband vital sign signal, whereas the spatial methods enable attenuation of directional interference and motion clutter resulting from a dynamic measurement environment. Spatial methods can additionally be used to distinguish multiple subjects even if their vital sign signatures are identical. The presented methods are compared to the case of using a simple one receiver system.

4.1 Review of Multiantenna Vital Sign Monitoring

The application of microwave radio waves in monitoring of human respiration was proposed already in the 1970's [1]. A simple SISO CW radar system was introduced to detect the breathing induced micro-Doppler phase modulation. Since then, this technique has been extended to include monitoring the higher frequency heart beat as well. During the last decade, the main research focus in wireless vital sign monitoring has been in devising various signal processing methods to improve the system performance [31, 43]. However, the SISO system cannot be used to mitigate the problem of excess motion artifacts and other sources of micro-Doppler motion. Therefore, the application of MIMO systems has been suggested to address these problems.

To address the problem of monitored subject random body movement cancellation, a fixed geometry two receiver CW radar system has been proposed [44]. The two receivers are placed in front and behind the subject to enable monitoring of the vital signs. Since the sign of the vital sign phase components are equal at both receivers, whereas other motion artifacts differ in sign, the random phase interferences

may be removed by simple addition of the two receivers phase terms. The main restriction of this technique is the fixed measurement geometry, since observations are needed from both sides of the monitored subject.

It has been shown in [4, 24] that multiantenna systems can be used in detection of multiple source of micro-Doppler motion. An array of receive antennas is used to either determine the signal direction of arrival, or the problem of determining the number of different sources is formulated into a problem of model order selection. The latter paper presents a generalized likelihood ratio test (GRLT) for testing a composite hypothesis on the number of subjects present. A more complex MIMO system utilizing the BLAST techniques to isolate unwanted interference from the signal of interest was proposed in [45], thus enabling detection of multiple source signals. Additional processing is however required to estimate the vital sign rates of the different subjects.

Although it is generally known that such multiantenna techniques may be used to increase the channel capacity, the advantage of these systems in vital sign monitoring has not been studied in detail. In addition to presenting a novel approach to vital sign monitoring with multiantenna systems using adaptive filtering techniques, this thesis evaluates the performance of the proposed method, as well as prior multiantenna processing techniques.

4.2 Adaptive Noise Cancellation

Adaptive noise cancellation is an application of adaptive filtering. Adaptive filtering is generally used in time-variant systems where the signal or noise frequency characteristics may vary with time. This is also the case in vital sign estimation, where the cardiopulmonary signal frequencies experience natural temporal fluctuations, thus requiring adaptation of the filter coefficients. In the vital sign application, the baseband cardiopulmonary signal of interest is a narrowband signal at frequencies below 4 Hz, whereas the masking additive noise is wideband with a uniform power spectrum. Therefore the goal of adaptive filtering is to provide an accurate estimate of this narrowband signal, while suppressing the wideband noise outside the band of interest.

Self-tuning of the adaptive filter coefficients is generally based on the knowledge of the desired output signal, which is either transmitted as training data or known in advance. The multiantenna vital sign estimation system developed in this thesis uses the former approach, where one antenna is configured as a reference receiver that provides the "desired" output $y(k)$, as is illustrated in Figure 16. This setup allows for real time filter adaptation without the need of sequential transmission breaks due to recalibration with separate training data. Furthermore, as a result multiple antennas observing the same phase modulating source, the signals containing vital sign information at different receivers are highly correlated with a deterministic delay. On the contrary, the additive noise components can be approximated as uncorrelated samples of white Gaussian noise. By exploiting the high correlation between the different antennas, the secondary inputs can be adaptively filtered to obtain an estimate $\hat{y}(k)$ where the wideband noise is attenuated, thus enhancing the

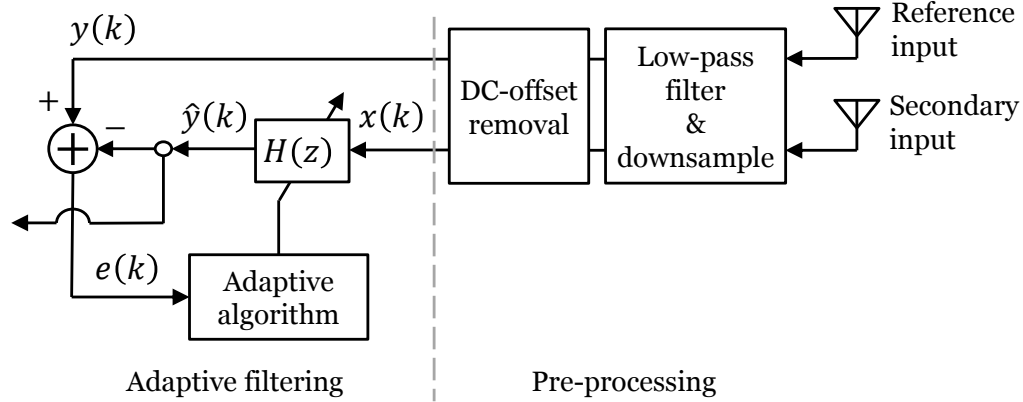


Figure 16: Adaptive noise cancellation system block diagram used in multiantenna vital sign estimation. The delay of the secondary inputs correspond to the respective propagation path delays at a given angle of arrival φ .

original signal. [35] An adaptive noise cancellation system like this is also known as an adaptive line enhancer.

Since the filter is adjusted to match the correlated secondary input signal to the primary signal, the filter becomes essentially a frequency selective bandpass filter where the frequency response peaks at observed signal frequencies. With a long enough filter length, it would be possible to estimate the vital sign frequencies from the filter frequency response. However, the filter length is one important parameter in the adaptation process, and as the performed simulations imply, should be below 250 ms to guarantee fast enough adaptation. As a consequence, the resulting frequency resolution is not enough to allow accurate estimation of the vital sign parameters from the filter frequency response; thus the advanced frequency estimation techniques presented in Chapter 3 are necessary.

In addition to choosing the optimal length for the adaptive filter, there are other decisions to be made on the adaptation algorithm itself. The following section introduces a widely used optimization criterion in adaptive filtering, which is later on applied in the presentation of three commonly used adaptation algorithms known as the least-mean-squares (LMS), normalized least-mean-squares (NLMS) and recursive-least-squares (RLS).

4.2.1 Minimum Mean-square-error Filtering

An important consideration in the design of adaptive filter algorithms is the optimization criterion for adjusting the filter parameters. The criterion must not only be meaningful from the applications point of view, but it needs to result in a practically realizable algorithm as well. Some optimization criterion, like minimizing the average probability of error in a communication system, might result in a nonlinear function of the filter coefficients, which is highly undesirable due to implementation complexity. However, two good criteria that are known to provide good performance measures in adaptive filtering are the least-squares (LS) and mean-square-

error (MSE) criterion. Both criterion results in a quadratic performance index for the filter coefficients having a unique minimum or maximum solution. This section introduces the minimum mean-square-error (MMSE) filtering, which is later used in derivation of the stochastic gradient based LMS algorithm used to minimize a convex error function.

The derivation of the optimum filter using the MMSE criterion is based on the system identification problem; determine system time-domain or frequency domain characteristics by observing the system input and output sequences. Assuming that the complex valued transmitted data sequence $x(k)$ is generated from a stationary random process and has an autocorrelation sequence

$$r_{xx}(m) = E\{x(k)x^*(k-m)\}. \quad (4.2.1)$$

Then by using the samples $x(k)$, it is possible to construct an estimate of the observed output sequence $y(k)$ by filtering the input data with a causal FIR filter of length L having unknown coefficients $h(k)$. The output of the filter is now the estimate $\hat{y}(k)$ of our desired sequence $y(k)$

$$\hat{y}(k) = \sum_{n=0}^{L-1} h(n)x(k-n), \quad k = 0, \dots, M-1. \quad (4.2.2)$$

Due to the finite sample length and additive noise, the derived estimator will always contain some error. The estimation error is defined as

$$\begin{aligned} e(k) &= y(k) - \hat{y}(k) \\ &= y(k) - \sum_{n=0}^{L-1} h(n)x(k-n), \end{aligned} \quad (4.2.3)$$

which can be simplified by using matrix notation to

$$\mathbf{e} = \mathbf{y} - \mathbf{X}\mathbf{h}, \quad (4.2.4)$$

where \mathbf{y} is a $M \times 1$ vector of system outputs $\mathbf{y} = [y(0), y(1), \dots, y(M-1)]^T$, \mathbf{X} is a $M \times L$ data matrix with input snapshots as rows, \mathbf{h} is the unknown $L \times 1$ dimensional coefficient vector $\mathbf{h} = [h(0), h(1), \dots, h(L-1)]^T$, and \mathbf{e} is a $M \times 1$ vector of errors. In order to optimize the estimator accuracy, the estimation error should be constrained with some optimization criterion. One typically used optimization criterion leading to a quadratic optimization problem is to minimize the mean-square error of the estimate as a function of the filter coefficients, that is

$$\mathcal{E}_{MSE} = E\{|\mathbf{e}|^2\} \quad (4.2.5)$$

$$\begin{aligned} &= E\{\mathbf{e}^H \mathbf{e}\} \\ &= E\{(\mathbf{y} - \mathbf{X}\mathbf{h})^H (\mathbf{y} - \mathbf{X}\mathbf{h})\} \\ &= E\{\mathbf{y}^H \mathbf{y}\} - E\{(\mathbf{X}^H \mathbf{y})^H\} \mathbf{h} - \mathbf{h}^H E\{\mathbf{X}^H \mathbf{y}\} + \mathbf{h}^H E\{\mathbf{X}^H \mathbf{X}\} \mathbf{h} \end{aligned} \quad (4.2.6)$$

where $(\cdot)^H$ denotes the conjugate transpose operation. By noting that $E\{\mathbf{y}^H \mathbf{y}\} \triangleq P_y$ is the signal power of the desired sequence \mathbf{y} , $E\{\mathbf{X}^H \mathbf{y}\} \triangleq \mathbf{r}_{xy}$ is the cross-correlation vector between data \mathbf{X} and response \mathbf{y} , and that $E\{\mathbf{X}^H \mathbf{X}\} \triangleq \mathbf{R}_{xx}$ is the Hermitian Toeplitz data autocorrelation matrix, we can rewrite the expression (4.2.6) as

$$\mathcal{E}_{MSE} = P_y - \mathbf{r}_{xy}^H \mathbf{h} - \mathbf{h}^H \mathbf{r}_{xy} + \mathbf{h}^H \mathbf{R}_{xx} \mathbf{h}. \quad (4.2.7)$$

Finally, the minimum filter coefficient vector \mathbf{h} and the minimum squared error can be solved from (4.2.7) by reformulating it into a perfect square as

$$\mathcal{E}_{MSE} = P_y - \mathbf{r}_{xy}^H \mathbf{R}_{xx}^{-1} \mathbf{r}_{xy} + (\mathbf{R}_{xx} \mathbf{h} - \mathbf{r}_{xy})^H \mathbf{R}_{xx}^{-1} (\mathbf{R}_{xx} \mathbf{h} - \mathbf{r}_{xy}). \quad (4.2.8)$$

As the input and output sequences are random variables and the minimization is performed as a function of the filter coefficients \mathbf{h} , the mean-square-error \mathcal{E}_{MSE} reaches its minimum when the last term in (4.2.8) is minimized. The squared expression $(\mathbf{R}_{xx} \mathbf{h} - \mathbf{r}_{xy})^H \mathbf{R}_{xx}^{-1} (\mathbf{R}_{xx} \mathbf{h} - \mathbf{r}_{xy})$ can only get nonnegative values, hence it has the smallest positive contribution of zero when

$$\begin{aligned} \mathbf{R}_{xx} \mathbf{h} - \mathbf{r}_{xy} &= \mathbf{0} \\ \mathbf{R}_{xx} \mathbf{h} &= \mathbf{r}_{xy}. \end{aligned} \quad (4.2.9)$$

These are the Wiener-Hopf equations that give the optimum linear FIR filter in the MMSE sense [35].

A unique solution for the filter coefficients \mathbf{h} exists whenever the autocorrelation matrix \mathbf{R}_{xx} is positive definite; that is $\mathbf{a}^H \mathbf{R}_{xx}^{-1} \mathbf{a} > 0$ for all $\mathbf{a} \neq \mathbf{0}$. In general, \mathbf{R}_{xx} is guaranteed to be at least positive semidefinite. However, in most physical applications the autocorrelation matrix is also positive definite, thus possessing an inverse [28]. Consequently, the coefficients \mathbf{h} are given by

$$\mathbf{h} = \mathbf{R}_{xx}^{-1} \mathbf{r}_{xy}, \quad (4.2.10)$$

which is the optimum causal FIR Wiener filter, and the resulting MMSE is thereafter

$$\mathcal{E}_{MMSE} = P_y - \mathbf{r}_{xy}^H \mathbf{R}_{xx}^{-1} \mathbf{r}_{xy}. \quad (4.2.11)$$

Finding the solution for (4.2.10) will give the optimal filter weights. For small values of L , the solution is usually straightforward as shown in [46], but with long filter lengths the problem presents a significant computational burden due to the inversion of the $L \times L$ autocorrelation matrix \mathbf{R}_{xx} . Furthermore, in many applications like vital sign estimation, the input signal statistics might change slowly over time, thus requiring continuous filter coefficient optimization. In practice, a perfect solution for the coefficients cannot be found because the correlation values are estimated from a finite sample space.

An approximate solution for the equation (4.2.10) can be found using steepest descent gradient based iterative algorithms. One of these algorithms is the widely used iterative stochastic gradient LMS algorithm presented in the following section for adaptive antenna arrays. The LMS algorithm solves the convex optimization problem based on instantaneous error values, instead of the true gradient, thus removing

the need for complex inversions and estimations. In general, for nonstationary processes like the cardiopulmonary activity in vital sign estimation, the system weights \mathbf{h} need to be solved for each time instant separately. This is a problem for real time applications utilizing gradient based algorithms that have a slow convergence time. However, there are fast recursive algorithms for updating the weights. One such algorithm is the RLS, which is based on LS error minimization [35]. The problem of convergence time is thus not a problem for real time processing, but it could still be an issue if the signal statistics change before the algorithm converges.

4.2.2 Least-Mean-Square Algorithm

The LMS algorithm is an iterative algorithm for finding an approximate solution to the Wiener-Hopf equations (4.2.9). The LMS finds the solution by a method of steepest-descent search using the stochastic gradient of the MMSE equation as the direction vector. Solving the Wiener-Hopf equations directly relies on acquiring accurate estimates of the auto- and cross-correlation matrices. It is computationally expensive for long filter lengths due to the inversion of the autocorrelation matrix. Instead of finding correlation estimates by lengthy averaging, the LMS algorithm uses instantaneous values of the squared error for iterative optimization of the filter coefficients. The LMS algorithm has its main applications in adaptive filtering with equalizers, adaptive noise cancellation systems. This chapter gives a mathematical formulation for the LMS algorithm from an adaptive antenna array point of view, where the algorithm is used to find optimal array input weights to suppress interference impinging the array from a specific look direction.

Generally, the LMS algorithm finds a solution for an overdetermined system of equations where there are more equations than unknowns. The solution is found by starting from an initial guess, and iteratively searching the optimal solution by changing the weights $\mathbf{h} = [h(0), h(1), \dots, h(L-1)]^T$ along the direction of the instantaneous estimate of the true gradient of the MSE cost function. The iterative update algorithm for the coefficients is given by

$$\mathbf{h}(k+1) = \mathbf{h}(k) + \beta \nabla_{\mathbf{h}} e^2(k), \quad (4.2.12)$$

where $\mathbf{h}(k+1)$ is the updated coefficient vector obtained from the previous iteration value $\mathbf{h}(k)$ corrected by the scaled gradient of the squared instantaneous estimation error, that is $\beta \nabla_{\mathbf{h}} e^2(k)$ [35]. Here $\beta < 0$ denotes the step size controlling the algorithm rate of convergence and stability, and k is the iteration and time index. It is worth noting that the gradient approximation is computed for a single time sample of the squared error, which is defined as

$$\begin{aligned} e^2(k) &= \left(y(k) - \sum_{i=0}^{L-1} x_i(k) h_i^* \right)^2 & k = 0, \dots, M-1 \\ &= (y(k) - \mathbf{h}^H \mathbf{x}(k))^2, \end{aligned} \quad (4.2.13)$$

where $\mathbf{x}(k)$ is the $L \times 1$ array input snapshot at time instant k . Consequently, the

approximation of the gradient using instantaneous error is given by

$$\begin{aligned}\nabla_{\mathbf{h}} e^2(k) &\approx -2 (y(k) - \mathbf{h}^H \mathbf{x}(k)) \mathbf{x}(k) \\ &= -2e(k) \mathbf{x}(k).\end{aligned}\tag{4.2.14}$$

Inserting this gradient to the iterative update equation (4.2.12), the LMS algorithm for array coefficients becomes

$$\mathbf{h}(k+1) = \mathbf{h}(k) - 2\beta e(k) \mathbf{x}(k).\tag{4.2.15}$$

Whenever the value of β is chosen within the limits

$$-\frac{1}{\lambda_{max}} < \beta < 0,\tag{4.2.16}$$

where λ_{max} is the maximum eigenvalue of \mathbf{R}_{xx} , the LMS converges towards the optimal Wiener-Hopf solution (4.2.10), see Appendix A for detailed convergence analysis. The LMS algorithm is not able to reach the optimal solution due to the excess MSE, which with WSS signals is determined by the step size β , and the eigenvalues of the autocorrelation matrix [47]. Furthermore, this algorithm will converge to a solution even when the autocorrelation matrix \mathbf{R}_{xx} is not invertible and direct application of (4.2.10) would not be possible [28].

In addition to the simplicity of the LMS algorithm, it is also robust against disturbances like measurement noise, model mismatches, quantization errors, and various other inaccuracies. As is shown in [48], the LMS algorithm is the most robust adaptive algorithm in a sense that the resulting estimation error energy will never exceed the associated energy of the disturbances.

Choosing the adaptation step size parameters β is always a tradeoff between speed of convergence and excess MSE in the steady state. Whenever the signal satisfies the wide-sense stationary (WSS) condition, one can choose a small step size in order to obtain small steady state error. However, if the WSS assumption is not applicable, it is typically necessary to have a larger step size to enable tracking of the changing signal statistics. This in turn results in a larger excess MSE [47]. On the other hand, if the step size is fixed for non-stationary signals, although in reality the signals might be quasi-stationary over some observation windows, the LMS yields an overly MSE. This problem of fixing the step size with nonstationary signals is overcome by using an adaptive step size version of LMS known as normalized LMS algorithm.

4.2.3 Normalized Least-Mean-Square Algorithm

The normalized LMS algorithm is an adaptive step size variation of the previously described LMS algorithm. They both have the same operation principle of recursively updating the filter weights using a gradient estimate of the instantaneous squared error. Additionally, the convergence of these algorithms is controlled by one parameter that is the step size β . However, as was already pointed out, the LMS algorithm is mainly designed to operate in WSS signal conditions where the

signal characteristics do not change rapidly over multiple observation periods. The WSS assumption enables the use of a smaller fixed step size β , resulting in slower convergence but also a smaller steady state error. The steady state error is the mismatch in filter coefficients with respect to the optimal filter. The error is a result of a large step size that prevents the coefficients from converging beyond a threshold to the optimal solution. As opposed to LMS, the NLMS algorithm is designed for nonstationary environments where signal statistics may change within consecutive observations. This imposes high requirements for the algorithm as it should be able to track fast signal changes while minimizing the error resulting from too large step size. The following presents a brief derivation of the NLMS algorithm based on the book by [28].

The goal of NLMS algorithm is to approximate the filter coefficients \mathbf{h}_0 , that correspond to the optimal filter of a stationary signal at a given time instant. As the signal statistics may change over time, also the respective optimal filter coefficients \mathbf{h}_0 vary with time. The recursive coefficient update rule for $\mathbf{h}(k+1)$ is based on the input signal vector $\mathbf{x}(k+1)$, the desired reference response $y(k+1)$, and the previous coefficient estimate $\mathbf{h}(k)$. The updated estimate is chosen to satisfy $\|\tilde{\mathbf{h}}(k+1)\| < \|\tilde{\mathbf{h}}(k)\|$, where $\tilde{\mathbf{h}}(k) = \mathbf{h}(k) - \mathbf{h}_0$ is the coefficient error. By decomposing the error vector $\tilde{\mathbf{h}}(k)$ into two orthogonal components

$$\tilde{\mathbf{h}}(k) = \tilde{\mathbf{h}}_x(k) + \tilde{\mathbf{h}}_x^\perp(k), \quad (4.2.17)$$

where $\tilde{\mathbf{h}}_x(k)$ is parallel, and $\tilde{\mathbf{h}}_x^\perp(k)$ perpendicular to the input vector $\mathbf{x}(k)$, the response of the error filter $\tilde{\mathbf{h}}(k)$ with input $\mathbf{x}(k+1)$ can be written as

$$\tilde{y}(k+1) = \tilde{\mathbf{h}}^H(k)\mathbf{x}(k+1) = \tilde{\mathbf{h}}_x^H(k)\mathbf{x}(k+1). \quad (4.2.18)$$

Furthermore, this implies that

$$\tilde{\mathbf{h}}_x(k) = \frac{\tilde{y}^*(k+1)}{\|\mathbf{x}(k+1)\|^2} \mathbf{x}(k+1), \quad (4.2.19)$$

and therefore the best way to update the coefficients $\mathbf{h}(k+1)$ is given by subtracting $\tilde{\mathbf{h}}_x(k)$ from $\tilde{\mathbf{h}}(k)$, thus resulting in the following update recursion

$$\tilde{\mathbf{h}}(k+1) = \tilde{\mathbf{h}}(k) - \tilde{\beta} \frac{\tilde{y}^*(k+1)}{\|\mathbf{x}(k+1)\|^2} \mathbf{x}(k+1) \quad (4.2.20)$$

Now, the time-dependency of the step size parameter can be seen by setting

$$\beta(k+1) = \frac{\tilde{\beta}}{\|\mathbf{x}(k+1)\|^2}. \quad (4.2.21)$$

This shows that the NLMS algorithm may exhibit a faster rate of convergence than the conventional LMS algorithm. Potential issues with this adaptive step size of the NLMS algorithm may be introduced if the input vector $\mathbf{x}(k+1)$ is small, since the division by the squared norm could result in numerical difficulties. However, this problem can be mitigated by modifying the equation for the step size (4.2.21) by adding a small weight δ in the denominator [47].

4.2.4 Recursive Least-Square Algorithm

The main advantage of the LMS algorithm lies in its computational simplicity and ease of implementation. However, a downside of the simplicity is the algorithm's slow convergence towards the optimal Wiener solution. The problem of slow convergence is especially emphasized in applications, such as the vital sign estimation, where the input signals are fluctuating over time and do not fulfill the WSS requirement. If the adaptive algorithm is not able to reach a steady solution within a quasi-stationary signal window, the excess MSE may not be minimized thus degrading the performance of adaptive noise cancelling. Furthermore, the LMS algorithm has only one adjustable parameter to control the rate of convergence, that is the step size parameter β . In order to obtain faster convergence, it is necessary to use more complex algorithms like the recursive least-square algorithm.

The previously introduced LMS algorithm filter coefficient updating was designed to minimize the MSE by employing instantaneous estimation error approximation of the true gradient. Instead of using only instantaneous values, the RLS algorithm is based on the least squares approach, where the cost function to be minimized comprises of the sum of squared errors [47]. The RLS algorithm defines an recursive iterative solution to the LS problem, where the filter coefficients always attain the minimization of the sum of squared errors starting from the algorithm initialization. Therefore, the cost function to be minimized at time instant k is given by

$$\mathcal{E}(k) = \sum_{n=0}^k \lambda^{k-n} |e(n)|^2 = \sum_{n=0}^k \lambda^{k-n} |y(n) - \mathbf{h}^H(k) \mathbf{x}(n)|^2, \quad (4.2.22)$$

where λ is a constant forgetting factor $\lambda \in (0, 1]$, and $e(n)$ is the instantaneous error [28]. The forgetting factor is used to give past samples less attention than new ones. This ensures improved filter coefficient tracking capabilities in nonstationary signal conditions. If the forgetting factor is assigned the value $\lambda = 1$, then the RLS algorithm reduces to the conventional LS solution. When all input values are given equal weight, the RLS is said to have growing memory because the filter coefficients are a function of all observed input values [28].

For the recursive least squares optimization problem defined in (4.2.22), the optimal solution is given by the normal equations

$$\hat{\mathbf{R}}(k) \mathbf{h}(k) = \hat{\mathbf{r}}(k), \quad (4.2.23)$$

where $\hat{\mathbf{R}}(k)$ is the exponentially weighted finite sample estimate of the autocorrelation matrix

$$\hat{\mathbf{R}}(k) = \sum_{n=0}^k \lambda^{k-n} \mathbf{x}(n) \mathbf{x}^H(n) \quad (4.2.24)$$

and $\hat{\mathbf{r}}(k)$ is the respective cross-correlation vector

$$\hat{\mathbf{r}}(k) = \sum_{n=0}^k \lambda^{k-n} \mathbf{x}(n) y^*(n). \quad (4.2.25)$$

In order to operate in nonstationary signal conditions, the filter coefficients should be solved from (4.2.23) for each new time instant. This approach would be computationally very expensive firstly due to the inversion of the autocorrelation matrix, and secondly as both the auto- and cross-correlation values are each time computed from scratch. However, the computational burden can be reduced by rewriting $\hat{\mathbf{R}}(k)$ in terms of the past autocorrelation value as

$$\hat{\mathbf{R}}(k) = \lambda \hat{\mathbf{R}}(k-1) + \mathbf{x}(k)\mathbf{x}^H(k). \quad (4.2.26)$$

Similarly it is possible to compute the corss-correlation values with a time update recursion given by

$$\hat{\mathbf{r}}(k) = \lambda \hat{\mathbf{r}}(k-1) + \mathbf{x}(k)y^*(k). \quad (4.2.27)$$

Now by solving $\hat{\mathbf{R}}(k-1)$ and $\hat{\mathbf{r}}(k-1)$ from (4.2.26) and (4.2.27) while using (4.2.23), the new filter coefficient vector $\mathbf{h}(k)$ can be determined from the old vector $\mathbf{h}(k-1)$ with the following time-recursion

$$\mathbf{h}(k) = \mathbf{h}(k-1) + \mathbf{g}(k)e^*(k), \quad (4.2.28)$$

where $\mathbf{g}(k) = \hat{\mathbf{R}}^{-1}(k-1)\mathbf{x}(k)$ is the adaptation gain vector, and $e(k) = y(k) - \mathbf{h}^H(k)\mathbf{x}(k)$ is the a priori estimation error [28]. Although the computational load is reduced with the given recursions, the problem of inverting the correlation matrix still prevails in the gain vector.

To further simplify the computational burden, the inverse of the correlation matrix has to be computed recursively. By utilizing the previous rank 1 update equation (4.2.26) and the following result of the matrix inversion lemma

$$(\lambda \hat{\mathbf{R}} + \mathbf{x}\mathbf{x}^H)^{-1} = \lambda^{-1} \hat{\mathbf{R}}^{-1} - \frac{(\lambda^{-1} \hat{\mathbf{R}}^{-1} \mathbf{x})(\lambda^{-1} \hat{\mathbf{R}}^{-1} \mathbf{x})^H}{1 + \lambda^{-1} \mathbf{x}^H \hat{\mathbf{R}}^{-1} \mathbf{x}}, \quad (4.2.29)$$

it possible to obtain the desired update rule as

$$\mathbf{P}(k) = \lambda^{-1} \mathbf{P}(k-1) - \mathbf{g}(k)\bar{\mathbf{g}}^H(k), \quad (4.2.30)$$

where $\mathbf{P}(k) = \hat{\mathbf{R}}^{-1}(k)$, and $\bar{\mathbf{g}}(k) = \lambda^{-1} \hat{\mathbf{R}}^{-1}(k-1)\mathbf{x}(k)$ is the alternative adaptation gain vector [28]. Now the inversion of the correlation matrix is replaced by a simple scalar division while computing $\mathbf{g}(k)$. There are also square root algorithms for updating the square root of the inverse. Such algorithms may have better numerical properties than the conventional RLS [28].

Although the recursive computation of the correlation matrix and its inverse decreases the computational burden, the RLS algorithm is still no match to the simplicity of the LMS algorithm. The main complexity of the RLS algorithm results from updating of $\bar{\mathbf{g}}(k)$ and $\mathbf{P}(k)$. It has been shown in [28] that RLS can be implemented with a total update complexity of $2M^2 + 4M$ operations, whereas the LMS algorithm has a complexity of just $2M + 1$. Here each operation includes one multiplication and addition. However, when dealing with nonstationary signals, such as the reflections from cardiopulmonary activity, it is more important to consider the

algorithm speed of convergence since it determines the statistical accuracy and rate of adaptation.

As opposed to the LMS and NLMS, the RLS algorithm is typically considered to have a faster rate of convergence in MSE sense [28, 35]. This is due to the L elements of the gain vector $\mathbf{g}(k)$, that can be seen as individual parameters for controlling each filter coefficient. On contrary, the gradient based methods have only one parameter β controlling all filter coefficients. With WSS signals, this normally results in a faster MSE convergence for the RLS. However, with quasi-stationary signals the superiority of the RLS algorithms is not that obvious, since the fast temporal variations in the signal second order statistics necessitate short FIR filters. As a result, the advantage of multiple parameters may decrease for RLS, and the rate of convergence is mainly determined by the step size β and forgetting factor λ . A detailed convergence comparison between NLMS and RLS algorithms is presented in Chapter 5, along with experimentally optimized adaptation parameters for various SNR values.

Numerical instability of the RLS algorithm is another problem that is not encountered with the LMS. When the inverse of the correlation matrix $\mathbf{P}(k) = \mathbf{R}^{-1}(k)$ loses the Hermitian symmetry or is no longer positive definite, the RLS becomes numerically unstable. It has been shown that as long as $\lambda < 1$ the RLS algorithm is numerically stable, but diverges when $\lambda = 1$. [49] Besides this, if λ is given the value 1, then the algorithm loses its tracking ability with nonstationary signals, which is critical with especially vital sign estimation. However, the stability can be preserved by simply computing the upper triangular part of $\mathbf{P}(k)$, and then filling the rest of the matrix using the relation $p_{ij}(k) = p_{ji}^*(k)$, thus restoring the Hermitian symmetry. Another way to mitigate the stability issues of the algorithm is to use square root based RLS algorithms [28].

4.3 Spatial Methods

In radar applications, spatial methods are generally used with multiantenna receiver systems to determine how the observed signal energy is distributed over space. With coherent processing of the antenna inputs, spatial methods enable signal direction of arrival estimation and application of various signal enhancement and noise cancellation techniques. These techniques can further be used to improve the received signal SINR, thus enabling target detection and parameter estimation also in low signal conditions. Therefore, spatial methods have found applications in numerous fields, including radar and sonar systems, communications, seismology, underwater surveillance, and biomedical research like the task of vital sign estimation.

In many applications the information signal is impinging the receiver array from a specific angle, which might change over time. Therefore it would be advantageous from the detection point of view, if the receiver could focus on signals coming from this specific direction without physically moving the radar. As it turns out, this can be done by linearly combining the antenna inputs with specific weights. The weighting of antenna inputs is known as beamforming, because the process emphasized signals in one direction while attenuating all other directions, hence the name

spatial filter. Beamforming can be used both on the receiver and transmitter side, but as this thesis has its focus on receiver signal processing the former is given more attention. Receiver beamforming is sometimes referred to as spatial spectrum estimation as it enables estimation of the signal power over different look directions.

Beamforming is generally used in applications where the location of the target is not known a priori, or bad transmission channel conditions require spatial filtering for improved target detection. Beamforming techniques are widely used in military radar and air surveillance tasks due to its ability to quickly steer the transmitter or receiver beam by simply changing the antenna weights. Steering the array mechanically would be significantly slower. [19] However from the vital sign estimation point of view, the main advantage of beamforming is its spatial filtering properties that enable directional noise and motion clutter attenuation. For example, if a secondary subject is also illuminated by the radar, this subject will cause interference to the primary vital sign estimation. Therefore, if the direction of the primary subject is known, and the angular displacement between the two subjects is large enough relative to the radar, beamforming can be used to attenuate the directional interference from the secondary subject. In the context of this thesis, the main advantage of the spatial methods is ability to distinguish multiple subjects based on the received signal angle of arrival. This information can further be used to cancel out directional motion clutter to improve the SINR for estimation of primary vital sign parameters.

This chapter presents and evaluates typical beamforming techniques. The introduced beamforming techniques are not based on any specific array geometry, as generally in literature, but rely simply on the far field assumption and the knowledge of the receiver antenna coordinates. The presented spatial methods are finally applied in the conducted vital sign radar simulations to suppress directional interference and enhance the SINR. The simulations are discussed later on in Chapter 5.

4.3.1 Conventional Beamforming

The goal of conventional beamforming is to maximize the output SNR by linear weighting of the inputs. Using the notation from (2.3.17), the beamformer output signal can be defined as

$$y(k) = \sqrt{M_R} \cdot \mathbf{h}^H \cdot (\tilde{\mathbf{c}}(k) \circ \mathbf{b}_R(\varphi_R, f) + \mathbf{w}(k)). \quad (4.3.1)$$

In conventional beamforming the array weights $\mathbf{h} = [h_1, h_2, \dots, h_{M_R}]$ are chosen to perfectly phase-align signals impinging the array from a specific direction φ_R . The optimum steering vector satisfying this condition is simply the array response vector in the given direction

$$\mathbf{h} = \mathbf{b}(\varphi_R, f). \quad (4.3.2)$$

While this steering vector is a match to the array response for incoming signals in look direction φ_R , the steering vector is also known as the spatial matched filter. With a simple matched filter output SNR analysis, it can be shown that the resulting

beamforming SNR gain is given by

$$\text{SNR}_{\text{array}} \text{ (dB)} = M_R \cdot 10 \log_{10} \frac{a_m^2}{\sigma_w^2} = M_R \cdot \text{SNR}_{\text{elem}} \text{ (dB)}, \quad (4.3.3)$$

where a_m^2 and $\sigma_w^2 = E\{|w(k)|^2\}$ are the individual element signal and noise powers, and SNR_{elem} is the SNR per antenna [28].

Although equation (4.3.3) implies that the SNR of conventional beamforming could be improved by increasing the number of antennas, the physical reality limits the maximum array size. Furthermore, the spatial matched filter beamformer (MFB) maximizes the output SNR in the absence of interference, which is usually present in practical applications like vital sign detection. Therefore the use of optimum beamforming is preferred.

4.3.2 Optimum Beamforming

If the received signal at the array input is corrupted by interference, such as environmental or secondary subject motion, the optimum beamformer seeks to maximize the SINR by suppressing directional noise components. Let us assume that the array input signal consists of a primary signal, interference, and uncorrelated noise as in (4.3.1). Furthermore, assuming that all of these components are uncorrelated, the maximum output SINR is given by

$$\text{SINR}_{\text{out}}^{\text{max}} = M_R \cdot a_m^2 \mathbf{b}^H(\varphi_R, f) \mathbf{R}_{i+n}^{-1} \mathbf{b}^H(\varphi_R, f), \quad (4.3.4)$$

where $\mathbf{R}_{i+n} = \mathbf{R}_i + \sigma_w^2 \mathbf{I}$ is the interference-plus-noise correlation matrix [28]. The corresponding optimum beamformer can be thereafter obtained as a solution to the constrained optimization problem of

$$\min_{\mathbf{h}} \mathbf{h}^H \mathbf{R}_{i+n} \mathbf{h} \quad \text{subject to} \quad \mathbf{h}^H \mathbf{b}(\varphi_R, f) = 1. \quad (4.3.5)$$

As is shown in [34], the solution is the minimum-variance distortionless response (MVDR) beamformer given by

$$\mathbf{h} = \frac{\mathbf{R}_{i+n}^{-1} \mathbf{b}(\varphi_R, f)}{\mathbf{b}^H(\varphi_R, f) \mathbf{R}_{i+n}^{-1} \mathbf{b}(\varphi_R, f)}. \quad (4.3.6)$$

In practice, the correlation matrix is replaced by a finite sample estimate $\hat{\mathbf{R}}_{i+n}$ derived from the data. Such adaptive techniques are known as sample matrix inversion (SMI) beamformers where the correlation matrix is obtained through the average of outer products of the array snapshots

$$\hat{\mathbf{R}}_{i+n} = \frac{1}{N} \sum_{k=1}^N \mathbf{y}_{i+n}(k) \mathbf{y}_{i+n}^H(k), \quad (4.3.7)$$

where N is the number of averaged samples [28].

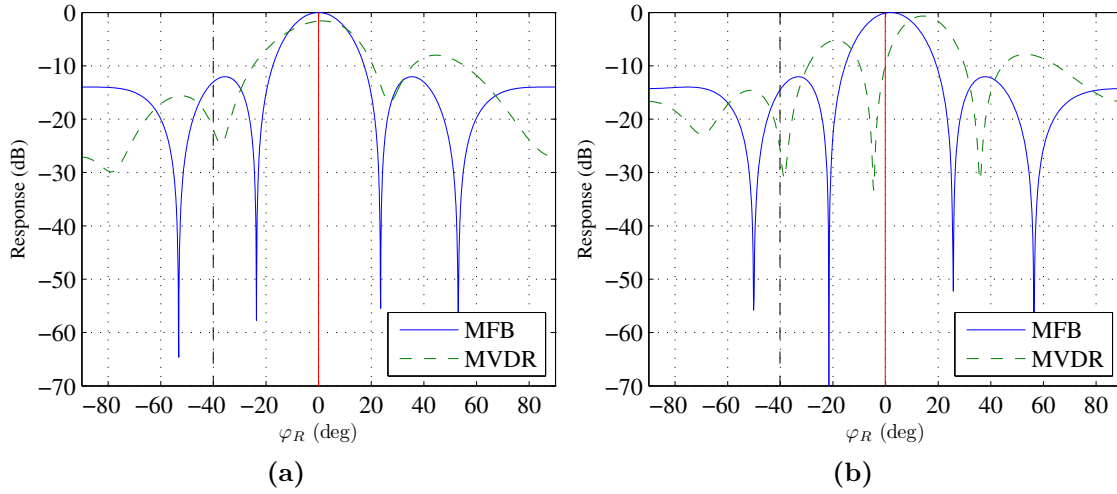


Figure 17: MFB and MVDR beampatterns using $M_R = 5$ receive antennas with $\lambda/2$ spacing with a) perfect knowledge of the target DoA, b) $\Delta\varphi_R = 2^\circ$ error in estimated target DoA. The target (solid red line) is located in look direction $\varphi_1 = 0^\circ$, and a source of interference (dashed black line) at $\varphi_2 = -40^\circ$. The MVDR beamformer is sensitive to DoA and steering vector mismatches.

Because this beamformer is data dependent via \mathbf{R}_{i+n} , it is able to suppress the directional interference components, as opposed to the conventional beamformer where any interference is passed on through the sidelobes. However, in the case that there is no interference present, the MVDR beamformer experience a small loss in output SINR compared to the matched filter, which is given by

$$L_{\text{SINR}} = \frac{\text{SINR}_{\text{out}}}{\text{SNR}_{\text{array}}} = a_m^2 \mathbf{b}^H(\varphi_R, f) \hat{\mathbf{R}}_{i+n}^{-1} \mathbf{b}^H(\varphi_R, f). \quad (4.3.8)$$

Nevertheless, in the presence of interference, the MVDR beamformer is superior to the conventional beamformer in terms of interference cancelling, see Figure 17a. [28]

It should be noted however, that in many applications it is not possible to obtain a primary signal free estimate of the correlation matrix \mathbf{R}_{i+n} . In such applications, like the vital sign estimation, the resulting Capon beamformer still maximizes the output SINR as long as there are no signal mismatches present. However, if the DoA of the primary signal is not precisely known, performance of the MVDR beamformer can decrease significantly as the array response is adjusted according to the inaccurate information. Figure 17b illustrates the effect of a small DoA error of $\Delta\varphi_R = 2^\circ$ to the performance of the Capon method. As can be seen, the optimum beamformer places a null in the direction of the target due to the error in DoA estimate. Thereby, to mitigate the effects of false assumptions or signal mismatches, it is necessary to use robust beamforming methods that are less sensitive to estimation and modeling errors.

4.3.3 Robust Capon Beamforming

The robust Capon beamformer (RCB) is an extension of the MVDR beamformer that enables operation under imprecise knowledge of array steering vector or primary signal DoA. Additionally, in many applications the sample size to form the correlation matrix might be limited, thus yielding another source of error. From the vital sign application point of view, the most probable source for inaccuracies are errors in signal DoA estimation simply because it might be difficult to determine from which part of the thorax the reflections are observed. Therefore, robust Capon beamforming is needed in especially live experiments to compensate for DoA mismatches.

The robust Capon beamforming follows the same approach as the MVDR, that is to minimize the output power while restricting the steering vector to a specific uncertainty ellipsoid

$$(\mathbf{b} - \tilde{\mathbf{b}})^H \mathbf{C}^{-1} (\mathbf{b} - \tilde{\mathbf{b}}) \leq 1, \quad (4.3.9)$$

where $\tilde{\mathbf{b}}$ is an a priori assumption of the steering vector \mathbf{b} , and $\mathbf{C} = \epsilon \mathbf{I}$ is a positive definite matrix defining the uncertainty as in [50]. Therefore the mathematical formulation of the robust beamforming can be stated as

$$\min_{\mathbf{b}} \mathbf{b}^H \hat{\mathbf{R}}^{-1} \mathbf{b} \quad \text{subject to} \quad \|\mathbf{b} - \tilde{\mathbf{b}}\|^2 = \epsilon, \quad (4.3.10)$$

when the trivial solution of $\mathbf{b} = \mathbf{0}$ is excluded. It has been shown in [50], that this quadratic optimization problem can be solved using the Lagrange multiplier methodology, which yields a solution in the form

$$\hat{\mathbf{b}} = \tilde{\mathbf{b}} - (\mathbf{I} + \lambda \hat{\mathbf{R}})^{-1} \tilde{\mathbf{b}}, \quad (4.3.11)$$

where $\hat{\mathbf{b}}$ is an estimate of the steering vector to the primary signal, and $\lambda \geq 0$ is the Lagrange multiplier. Now λ can be obtained as the solution to the constraint equation

$$g(\lambda) = \|(\mathbf{I} + \lambda \hat{\mathbf{R}})^{-1} \tilde{\mathbf{b}}\|^2 = \epsilon \quad (4.3.12)$$

which can be simplified using the eigendecomposition of the covariance matrix, and thereafter solved numerically as shown in [50]. The resulting beamforming weight vector is thereafter given by

$$\hat{\mathbf{h}} = \frac{\hat{\mathbf{R}}^{-1} \tilde{\mathbf{b}}}{\tilde{\mathbf{b}}^H \hat{\mathbf{R}}^{-1} \tilde{\mathbf{b}}} = \frac{(\hat{\mathbf{R}} + \frac{1}{\lambda} \mathbf{I})^{-1} \tilde{\mathbf{b}}}{\tilde{\mathbf{b}}^H (\hat{\mathbf{R}} + \frac{1}{\lambda} \mathbf{I})^{-1} \tilde{\mathbf{b}}}. \quad (4.3.13)$$

It is clear from (4.3.13) that the robust Capon beamformer has the form of diagonal loading with $\frac{1}{\lambda}$, which allows for an optimal amount of loading needed for a specified uncertainty ellipsoid.

It has been further shown in [51], that the robust Capon beamformer is robust with respect to choosing ϵ . This implies that the beamformer is able to adjust its diagonal loading optimally, even if the value of ϵ is not chosen in an optimal way. Furthermore, the RCB is also robust against small mismatches in estimated DoA

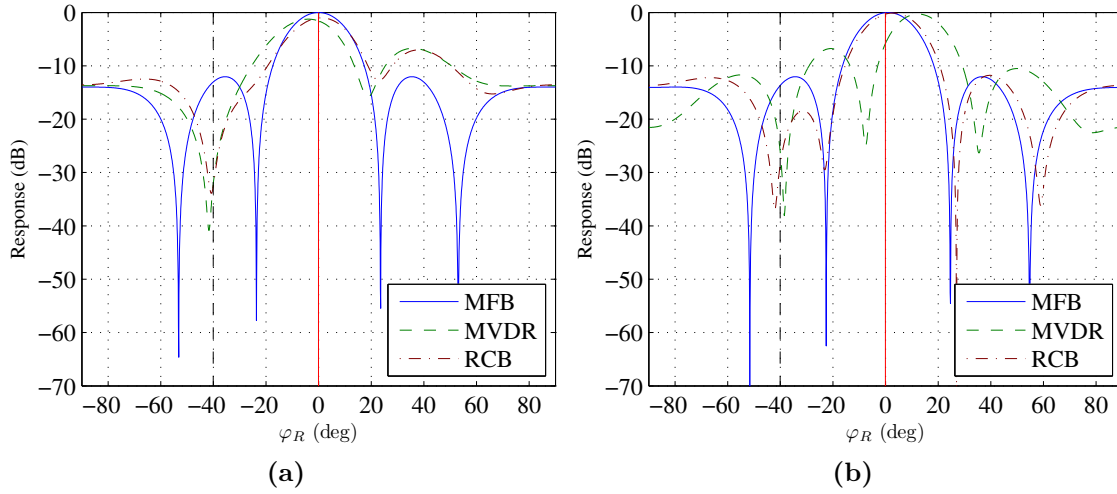


Figure 18: Beampatterns of MFB, MVDR, and RCB using a 5-element ULA ($d = \lambda/2$) with a) perfect knowledge of target DoA and array model, and b) an error of $\Delta\varphi_R = 1^\circ$ in the DoA estimate. A primary subject (solid red line) is located at $\varphi_1 = 0^\circ$, and a secondary interferer (dashed black line) at $\varphi_2 = -40^\circ$. The RCB is more robust against small mismatches in DoA estimate and array model.

and array model. With an error of just $\Delta\varphi_R = 1^\circ$ in DoA, the RCB is able to focus on the primary target, while still attenuating the interferer present at $\varphi_R = -40^\circ$, see Figure 18b. With a similar DoA error the MVDR sees the primary target as interference and attenuates the signal by placing a null close to the corresponding look direction. Due to this instability of the MVDR, it is necessary to use RCB especially in the application of multiantenna vital sign monitoring.

Before the application of beamforming techniques, it is essential that the incoming signal angle of arrival is known or estimated from the data. Thereafter, the array beampattern can be steered towards the target. The following section introduces how the DoA estimate can be obtained from the array data, and presents a commonly used estimation method known as the Capon method. This method is analogous to the previously described Capon method for time series signal processing in section 3.3.2, and is based on the same MVDR criterion as the Capon beamformer.

4.3.4 Direction of Arrival Estimation

In the presence of multiple vital sign emitting subject, the only parameter that distinguishes the subjects apart is the signal angle of arrival, or direction of arrival. If the DoA of the primary subject reflections are known or estimated from the data, it is possible to apply the presented beamforming techniques to suppress any additional interference. Although there are numerous DoA estimation methods in the literature, this section focuses on the familiar and well known Capon method.

A general approach to the DoA problem is to scan the array using all possible

steering vectors and determine which look direction gives the highest energy response

$$E \{ |\mathbf{y}(k)|^2 \} = \mathbf{h}^H \hat{\mathbf{R}}_y \mathbf{h}, \quad (4.3.14)$$

where $\hat{\mathbf{R}}_y = E \{ \mathbf{y}(k) \mathbf{y}^H(k) \}$ is the correlation matrix comprising of the signal, interference, and noise. With the conventional beamformer the DoA estimate is given by inserting (4.3.2) into (4.3.14), and consequently searching for the location of the highest peak [34]. The accuracy of the direction estimate depends of the angular resolution capabilities of the array. Typically the resolution is defined as the angular extent between the array main beam half-power points, that is, points where the maximum power has dropped by 3 dB. Often the angular resolution in radians is approximated as

$$\Delta\varphi_{3\text{dB}} \approx \frac{\lambda}{D}, \quad (4.3.15)$$

where D is the size of the array aperture in wavelengths [28]. For example, let us again take the example of a ULA array with $M_R = 5$ elements observing two targets at angles $\varphi_R = 0^\circ$ and $\varphi_R = -20^\circ$. Now using the approximation of (4.3.15), the angular resolution of the array with $d = \lambda/2$ element spacing is $\Delta\varphi_{3\text{dB}} \approx 23^\circ$. Thereby the secondary target cannot be distinguished from the primary target using the conventional beamformer, see Figure 19b. Furthermore, when the conventional beamforming is used for a general case of multiple targets, the resulting DoA estimates are inconsistent. This is important especially if the sources are closely spaced or highly correlated, since then the asymptotic bias of the estimates might be significant. A higher DoA resolution can be obtained by using the Capon based estimation methods.

The Capon DoA estimation method is essentially based on the same approach as with the conventional beamformer; find the steering vector $\mathbf{b}(\varphi_R, f)$ yielding the

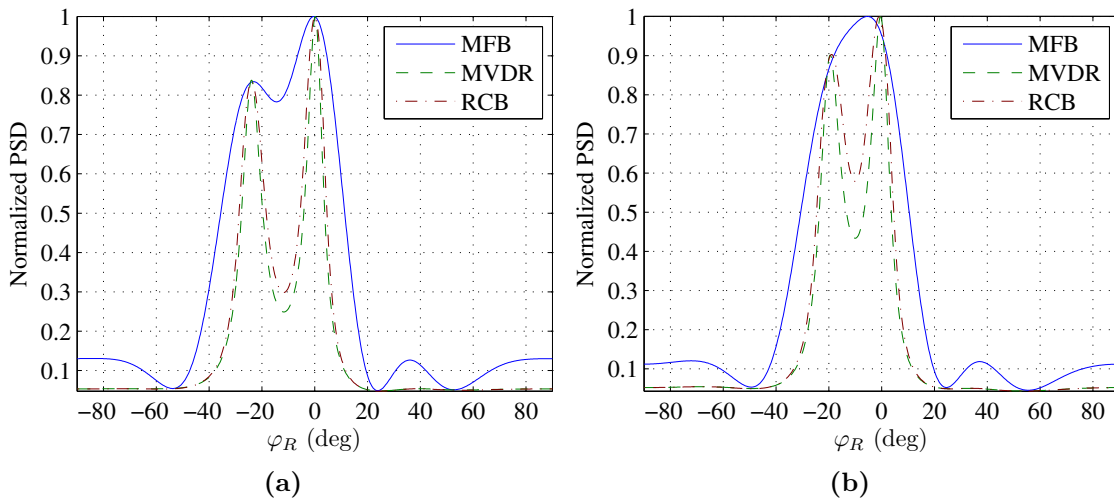


Figure 19: Spatial spectrum of MFB, MVDR, and RCB techniques with a 5-element ULA ($d = \lambda/2$) observing two targets at $\varphi_1 = 0^\circ$ and a) $\varphi_2 = -20^\circ$, and b) $\varphi_2 = -24^\circ$. Capon based beamforming methods have a higher resolution than the MFB.

highest energy response. As was already shown with the Capon beamformer, the optimum spatial weighting coefficients \mathbf{h} minimizing the constrained optimization problem of (4.3.5) are given by (4.3.6). However, these weights are optimal for beamforming in a given look direction. To estimate the signal DoA, it is necessary to go through a range of possible steering vectors and see which look direction yields the highest response. Therefore, the spatial energy spectrum is obtained by inserting the weights defined by (4.3.6) into the expression of the received energy (4.3.14). As a result, the Capon signal DoA estimate can be obtained as the highest peak of the function

$$\frac{1}{\mathbf{b}^H(\varphi_R, f) \hat{\mathbf{R}}_y^{-1} \mathbf{b}(\varphi_R, f)}, \quad (4.3.16)$$

where $\hat{\mathbf{R}}_y^{-1}$ can be computed using the SMI technique given in (4.3.7) or an adaptive sample by sample update algorithm like the RLS introduced in chapter 4.2.4. As was shown in Figure 19, clearly both the Capon, and robust Capon methods have better resolution, and eventually also better interference cancelling capabilities than the conventional data-independent MF method.

In addition to these two introduced DoA estimation techniques, there are numerous other alternatives like the subspace methods MUSIC and ESPRIT. For more information about these methods, the reader is referred to [34, 35, 52].

4.4 Maximum Ratio Combining

A third approach to utilizing the high correlation between multiple receive antennas is to apply maximum ratio combining (MRC). MRC is a well-known technique used in multiantenna systems to combine the inputs of multiple receivers so that the output SNR is maximized. In its general form, the MRC performs coherent combining of the different signals by weighting and phase aligning receiver inputs with the eigenvector corresponding to the largest eigenvalue of the finite sample data covariance matrix

$$\hat{\mathbf{R}}(k) = \frac{1}{N} \sum_{k=1}^N \mathbf{y}(k) \mathbf{y}^H(k). \quad (4.4.1)$$

Here the vector $\mathbf{y}(k) \in \mathbb{C}^{2 \times 1}$ denotes the array input snapshot, and N is the corresponding window size. There are many similarities between the MRC and beamforming techniques, since both attempt to perfectly phase align the receiver inputs. With MRC, the weights depend on also on the signal quality of each individual component. While the MRC is strictly based on covariance matrix, it is sometimes referred to as blind beamforming, because it makes no assumptions on the receiver geometry.

The advantage of the MRC technique is that it requires only one parameter, which is the window size N used to obtain quasi-stationary samples of the observed signal. The stationarity assumption is important, since averaging over too long sequences may decrease the accuracy of the covariance matrix estimate if the signal second-order statistics change during averaging. However, the window length should not be too short either, since this would also prevent reliable estimation

of \mathbf{R} . Therefore, N is dependent on the observed input second order statistics, and should generally be chosen close to the stationarity period of the data. With quasi-stationary data like the vital sign modulated micro-Doppler phase information, the covariance matrix need to be periodically updated to follow the changing data statistics.

Like other signal processing techniques relying on an estimate of the covariance matrix, the MRC suffer from the problem of updating \mathbf{R} . There are however recursive techniques that may be used to decrease the computational burden of re-computing the covariance matrix from scratch on every update. One such recursive scheme was presented with the RLS algorithm in Section 4.2.4. Other factors that affect the computational complexity of the MRC are the update frequency, window length N , and in general case the array dimension.

4.5 Independent Component Analysis

Another recently developed method in data analysis for feature extraction and signal separation is known as independent component analysis. The goal of ICA is to find a linear representation of multivariate non-Gaussian data so that the components are statistically independent, or as close to independent as possible [53]. ICA was originally developed to solve problems similar to the well-known cocktail-party problem; separate multiple independent source signals observing only their mixtures. Since then, the increased interest in ICA has led to its application to many similar problems including artifact separation in magnetoencephalography (MEG) [54], feature extraction in image and audio signal processing, financial time series analysis [55], and separation of breathing and heartbeat in radar remote sensing [56, 57].

The basic principle of ICA can be understood through the blind source separation (BSS) problem. Suppose that n unknown mutually independent source signals $\mathbf{s}(t) = [s_1(t), \dots, s_n(t)]$ are observed through n sensors, where each sensor sees a mixture $x_i(t) = a_{i1}s_1(t) + a_{i2}s_2(t) + \dots + a_{in}s_n(t)$ of the independent components for all i . Using matrix notation, the observations can be written as

$$\mathbf{x}(t) = \mathbf{A}\mathbf{s}(t), \quad (4.5.1)$$

where $\mathbf{x}(t)$ is a column vector of the mixtures, and \mathbf{A} is the mixing matrix with elements a_{ij} [53]. The task is to estimate \mathbf{A} and the independent components $\mathbf{s}(t)$ solely based on the observations $\mathbf{x}(t)$, that is without further knowledge of the source signal model or distributions, hence the name blind source separation. Once the matrix \mathbf{A} is estimated, the independent components are obtained simply as

$$\mathbf{s}(t) = \mathbf{W}\mathbf{x}(t), \quad (4.5.2)$$

where $\mathbf{W} = \mathbf{A}^{-1}$ is the inverse of the mixing matrix [53]. However, the challenge is in finding an estimate for the matrix \mathbf{A} . Without any knowledge of the source signals, this problem can be solve up to ambiguities in component scaling, permutation, and sign [53]. Fortunately, these ambiguities are irrelevant in many applications, such as vital sign estimation.

The ICA model in (4.5.1) is solved through minimizing or maximizing certain contrast functions that allow reformulating the ICA problem to a numerical optimization problem. Although ICA requires no knowledge of the source signal models, it relies on the simple assumptions that the components s_i are statistically independent and have non-Gaussian distributions. In fact, the former assumption may be relaxed since ICA finds such components that are as close to independent as possible. However, the key to estimating the ICA parameters lies in the latter assumption of nongaussianity. Therefore, adding Gaussian noise to the model (4.5.1) results in that none of the independent components are allowed to have Gaussian distributions. With vital signs however, it is easy to show that the signal phase information is non-Gaussian, thus enabling application of ICA [56].

According to the Central Limit Theorem (CLT) the distribution of a sum of independent random variables tends towards a Gaussian distribution. Therefore, let us study the linear combination of the x_i , denoted by $y = \mathbf{w}^T \mathbf{x}$. Since the sum of two or more independent random variables is more Gaussian than the original variables, $\mathbf{w}^T \mathbf{A} \mathbf{s}$ becomes least Gaussian when it equals to one of the independent components. Thus, given a measure of nongaussianity such as kurtosis, or negentropy, where the latter one is a shifted entropy, it is enough to find such \mathbf{w} that maximizes the nongaussianity of $\mathbf{w}^T \mathbf{x}$. [53] For truly independent components, one may also use the fact that their joint distribution factors to the product of marginal distributions.

A fast and robust algorithm used for estimating the independent components is known as FastICA. The algorithm may be deployed as deflative component by component based estimation, or as a symmetric simultaneous estimation of all components [58]. The latter algorithm may be more desirable for certain applications as it pays equal attention to all components. Although ICA has the advantage of fast convergence and minimum presumptions on the source signals, it has the disadvantage of being nondeterministic, that is the order, amplitude, and sign of the independent components may not be estimated. However, all of this information may not be relevant for specific applications, as has been shown by numerous studies using ICA in various forms of BSS [54, 55, 56, 57].

As the typical challenge in vital sign monitoring is estimating the weak cardiac component from the signal, the ICA model has been proposed to solve this problem by separating the respiratory and cardiac artifacts as independent components [56]. Also, this reduces the problem of interfering breathing harmonics and other motion clutter. Interestingly enough, the technique provides good results even though generally one might consider the respiratory and cardiac activities to be highly correlated, which simply emphasizes the robustness of ICA. Furthermore, it has been shown that ICA can be used for isolating the cardiopulmonary activities of multiple subjects [57]. This is a significant advance for example towards wireless clinical healthcare vital sign monitoring, since ICA does not require any specific receiver antenna geometry or large angular separation between subjects, as compared to beamforming techniques. However, to limit the scope of this thesis, the ICA model was not applied in vital sign simulations.

4.6 Adaptive Vital Sign Estimation System

The main focus on this Section has been on coherently combining the multiple received signals to improve the performance of vital sign estimation. However, a complete wireless cardiopulmonary monitoring system comprises not only from this signal enhancement block, but from the combination of all signal processing techniques presented in Sections 3 and 4.

The complete adaptive vital sign estimation system employed in this thesis is illustrated as a block diagram in Figure 20. The multiantenna signal propagation model used in the simulations was presented in Section 2. With the application of multiple receivers, the vital sign induced micro-Doppler phase modulated signal is recorded and sampled using a sampling frequency high enough to prevent aliasing of the Doppler content. In our work, a sampling frequency of 50 Hz was used. Thereafter, the signal from each receiver may be pre-filtered to attenuate high frequency noise before downsampling. To focus solely on evaluation of adaptive filtering techniques, an allpass pre-filter was applied. Since different receivers contain various levels of DC offset, these components are removed using center tracking algorithms discussed in Section 3.2.2.

After all this pre-processing, the individual receiver signals are coherently combined using the adaptive processing techniques presented previously in this Section. The adaptive processing algorithms take as inputs the M_R distinct signals, and combine them coherently to generate one output signal preserving the vital sign micro-Doppler phase information. Depending on the chosen processing method, the signals pass through an adaptive noise cancellation system as presented in Section 4.2, or a spatial filtering system like in Section 4.3. Hereafter, the micro-Doppler phase content is extracted from the signal using complex signal demodulation techniques presented in Section 3.2. The choice of demodulation technique depends on the system carrier frequency, and amplitude of the micro-Doppler generating motion. Finally, the instantaneous vital sign frequency estimates are obtained with spectral estimation methods discussed in Section 3.3. The vital sign rate estimates

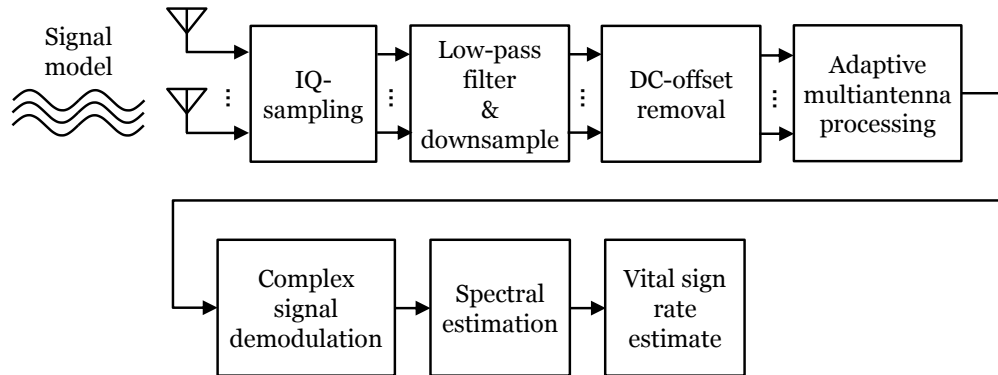


Figure 20: A block diagram of the multiantenna vital sign estimation system employed in this thesis. The Figure illustrates the different signal processing methods and their relative ordering.

are given by converting the instantaneous frequencies into beats per minute.

4.7 Challenges with Adaptive Techniques

As was shown in Section 4.2, adaptive filters can be used in estimation and tracking of instantaneous frequencies of human vital signs in the time-frequency domain. Many adaptive algorithms like the LMS algorithm, are based on modeling the data as a linear prediction filtering process, where each new data sample is estimated based on the previously observed samples. The frequency tracking performance of these adaptive filters is determined by the respective algorithm parameters and chosen filter length. For stationary signals the selection of these parameters is trivial since there is no need for adaptation. However, when the stationary condition is not met, optimal parameters like the speed of convergence and filter length are determined by the signal frequency characteristics. Additionally, the optimal parameters depend on the prevailing system SNR and performed signal pre-processing including temporal filtering and downsampling. Therefore, finding the optimal parameter values for adaptation require computationally intensive optimization algorithms with constraints on parameters like the output SNR and MSE, where there is no closed form solution available. Consequently the optimization needs to be done experimentally and in advance of the vital sign monitoring. Another significant disadvantage of the adaptive noise cancellation techniques is that simultaneous estimation of two or more subjects is not possible without spatial processing.

Although there are less parameters to consider in beamforming methods compared to adaptive filtering, they are extremely sensitive to parameter misadjustment. As was shown with the MVDR beamformer, if there is a small mismatch in the DoA estimate, the Capon beamformer will place a null in the beampattern in the direction of the target. Since this is highly unwanted behavior, more complex robust beamforming methods are required especially in real experiments where accurate array calibration is difficult. Furthermore, since the angular resolution of the beamforming techniques is directly related to the array aperture, the obtainable resolution is usually limited by the physical dimensions of the used device. Also in practice, acquiring accurate knowledge of the array steering vector requires complicated calibration measurements and varies between different arrays.

In order to combine the advantages of spatial beamforming and adaptive filtering, the use of space-time adaptive processing (STAP) could be introduced to vital sign estimation. Such techniques are already used in airborne moving-target indicator (MTI) systems operating in nonstationary environments with high levels of interference. [19] STAP increases the degrees of freedom by allowing simultaneous application of spatial filtering and adaptive noise cancellation through advanced signal processing algorithms [28]. However, the application of STAP would increase the system complexity to a level that is beyond the scope of this thesis.

Finally, the virtually parameterless ICA model provides a robust means for isolating the individual cardiopulmonary components from multiantenna observations. Although the method has almost no parameters, meaning that it requires little configuration, it is ambiguous against the variance and order of the independent

components. This implies that it is not possible to determine the power of the individual cardiopulmonary rates, nor to identify where the source originated from. In other words, it would be possible to determine the amount of persons in a room based on number of cardiac components, but there is no way of knowing which component corresponds to a specific subject. Additionally, there is little knowledge on the effects of ICA on the accuracy of the cardiopulmonary rate estimation. Despite these disadvantages, ICA is a good candidate tool in multiantenna vital sign monitoring, however as this thesis is focused on the adaptive filtering based techniques, the application and evaluation of ICA performance remain future research topics.

5 Simulation results

The performance of multiantenna adaptive signal processing techniques presented in this thesis were evaluated by a series of extensive vital sign estimation simulations. This Chapter gives a detailed description of the developed simulation environment, and presents the results of different simulation scenarios.

5.1 Simulation Environment and Measurement Setup

The basic simulation system implemented in MATLAB comprised of a 1×2 SIMO CW radar, operating at 24 GHz frequency, illuminating one human subject whose breathing and heart beats induce micro-Doppler effect. In order to study the performance of adaptive processing techniques and to simulate the beamforming techniques, two different simulation setups were constructed. The first setup is illustrated in Figure 21a, where one subject was located at a distance of 70 cm in front of the transmit antenna, and the two receivers were asymmetrically placed on both sides of the transmitter. Due to the large displacement of the receivers, this setup was used only with adaptive noise cancellation techniques. In the second setup, see Figure 21b, the two receivers had interelement spacing of $\lambda/2$, thus enabling application of the presented beamforming techniques in directional interference cancelling. Also, the advantages of larger ULA array were shown by increasing the number of receivers.

In addition to simulating reflections from vital sign targets, both setups included static reflections from walls, floor, and other background objects. The background material was chosen to be wood, having a complex permittivity of $\epsilon \approx 2.3 + j3.3$ at the K-band [59]. Furthermore, various levels of additive white Gaussian noise was included in the received signals to account for thermal noise and non-ideal circuitry at both transmitter and receivers.

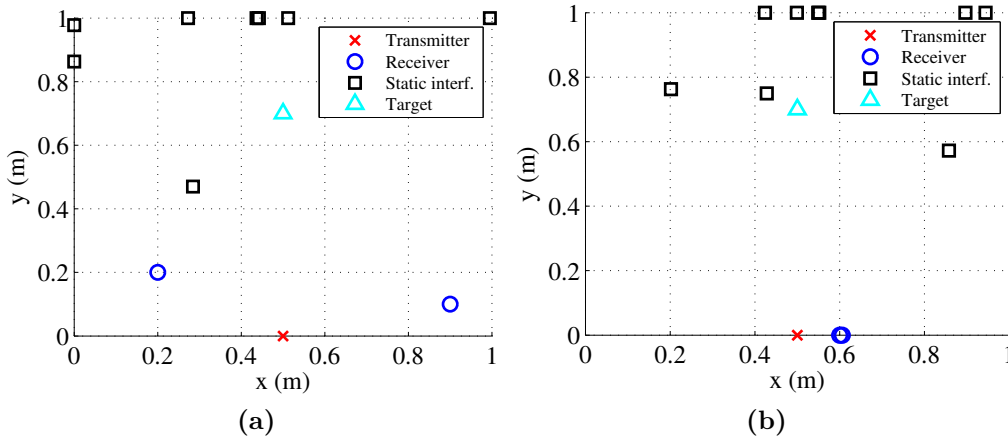


Figure 21: Geometric setup of the MATLAB simulations with a 1×2 CW radar observing one subject emitting vital signs. a) Multiantenna receiver, b) multiantenna receiver with $\lambda/2$ antenna displacement.

The received signal was modeled as a superposition of discrete reflection components according to the mathematical model given in eq. (2.3.9). It is typical to have this type of reflections from multiple sources, such as chest, throat, etc., or even secondary subjects nearby. Consequently, accurate estimation of the vital sign is more difficult. For simplicity, it is assumed in the first simulation setup with adaptive noise cancellation, that the phase modulating vital sign reflections are observed from only one source. To illustrate the directional interference cancelling capabilities of beamforming techniques, the second simulation setup is run with and without a secondary subject in the background. As a two receiver beamformer has only one degree of freedom for signal enhancement or interference cancelling, and the main beam is very wide, the performance of spatial filtering is evaluated also with more than two receivers.

The physiological motion of breathing and heartbeat are modeled according to the presented models in Section 2.1. In the following, the physical vibration of the human body induced by both vital sign activities, are modeled as sinusoids with independent and slowly varying frequencies. Therefore, the natural fluctuations in the rate of breathing and heartbeat, are modeled as random walks within a fixed frequency range of pre-defined minimum and maximum values. For details of implementation of the rate time-evolution, the reader is referred to [13].

5.2 Adaptive Processing Parameter Optimization

The rate of convergence and statistical performance of the NLMS and RLS adaptive processing algorithms are highly dependent on the chosen initial algorithm parameters. Therefore, to obtain the desired gains, the adaptive algorithm parameters need to be carefully selected. The main focus of this chapter is on finding the optimal filter length, the step size parameter, and the forgetting factor λ for the respective NLMS and RLS algorithms. The observed signal is not wide sense stationary which makes the optimization a challenging task. Moreover, the algorithm parameters are dependent on the receiver input SNR, pre-processing filter and downsampling, and the size and variability of the phase modulating micro-Doppler components. As there exists no closed form solution for choosing the data dependent parameters, the values were optimized for micro-Doppler frequencies in the range of 0.05 – 3.00 Hz using Monte-Carlo type simulations with a fixed pre-processing stage of no pre-filtering, and downsampling by a factor of 2. The specified range for micro-Doppler was based on minimum and maximum simulated vital sign frequencies.

In optimizing the algorithm adaptation parameters, the adaptive processing outputs, denoted by $y_{ap}(k) = \mathbf{h}^H(k)\mathbf{x}(k)$, where $\mathbf{h}(k)$ is defined in (4.2.20) for NLMS, and in (4.2.28) for RLS, were compared to a noiseless reference signal $y_{ref}(k)$ containing the same vital signs. Although such signal would be hard to obtain in actual measurements, it can be used in simulations to find the parameter values that may be employed in real world experiments as well. Therefore, the adaptation parameters were chosen as the values minimizing the algorithm output average squared

error, yielding the following performance metrics for NLMS

$$\mathcal{E}(L, \beta) = \frac{1}{N} \sum_{k=1}^N |y_{ref}(k) - y_{ap}(k)|^2, \quad (5.2.1)$$

and for RLS

$$\mathcal{E}(L, \lambda) = \frac{1}{N} \sum_{k=1}^N |y_{ref}(k) - y_{ap}(k)|^2. \quad (5.2.2)$$

As a result, using the mean square error as the optimization criterion results in an adaptation output signal that minimizes the squared residuals. In other words, the optimal output minimizing the MSE is the reference signal itself.

Typically with adaptive algorithms, the steady state MSE depends on the speed of adaptation. Faster adaptation yields a larger steady state MSE, whereas slower adaptation results in smaller excess error. Consequently, the choice of adaptation parameter values is generally a tradeoff between speed of convergence and steady state excess error. Moreover, another constraint that need to be considered in parameter optimization for vital sign monitoring is the limited sample size. It may not always be feasible to wait tens of seconds for algorithm convergence before estimating the vital signs, or the cost of acquiring more samples may be too high. As an example, locating earthquake victims buried in the debris is a time critical application where the usually vast areas of destruction should be searched within approximately two days. Another way to reduce adaptation excess error is to suppress the measurement noise through the adaptive filter structure. As a result it is not enough to simply optimize the adaptive algorithms for fast tracking, but also for noise attenuation through the choice of filter length.

The filter length and adaptation parameter values for NLMS and RLS algorithms were selected using exhaustive search. Figure 22 illustrates MSE values for both

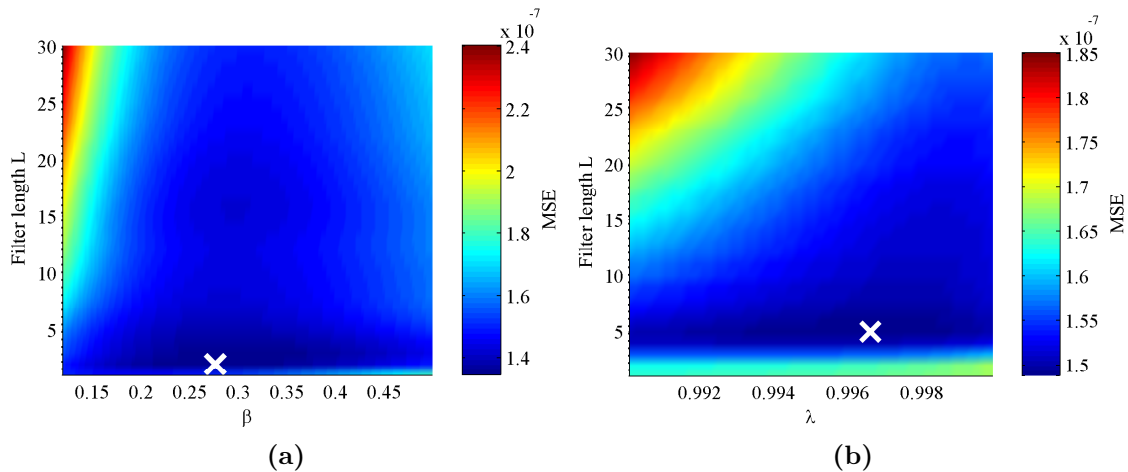


Figure 22: The parameter values for a) NLMS and b) RLS algorithms were found by minimizing the MSE, SNR = 16 dB. Results apply for one subject with both cardiopulmonary activities present.

algorithms with different parameter values. As can be seen, a local minimum is found for both algorithms. The adaptive parameter values were optimized for different levels of input SNR, and the results are listed in Table 3. Based on the optimized

Table 3: Optimized parameter values for NLMS and RLS algorithms are dependent on the prevailing SNR level. These values assume the presence of one subject with both cardiopulmonary activities present.

SNR (dB)	NLMS		RLS	
	L	β	L	λ
-10	23	0.015	1	0.9980
-8	23	0.025	3	0.9995
-6	19	0.025	4	0.9999
-4	15	0.030	3	0.9999
-2	18	0.040	3	0.9999
0	16	0.055	3	0.9999
2	12	0.085	3	0.9991
4	12	0.125	3	0.9991
6	10	0.140	2	0.9991
8	8	0.287	2	0.9995
10	4	0.145	2	0.9995

values, it can be seen that there is a nonlinear relation between the receiver input SNR and the adaptation parameters β and λ . Furthermore, when the SNR is low, the adaptive techniques increase the FIR filter length in order to make the filter more frequency selective. This is in line with the assumption that the adaptive techniques enable operation at lower SNR conditions through noise cancelling. The values given in Table 3 were used in all simulations concerning adaptive noise cancellation techniques.

5.3 Performance of Adaptive Noise Canceller

The performances of the adaptive noise cancelling techniques presented in this thesis were evaluated using SNR improvement and vital sign estimation success rate as quantitative criteria. The results were compared both to the case of using only one receiver, and MRC with multiple receivers.

5.3.1 Results for Estimating Both Cardiopulmonary Activities

The design of the adaptive filter is dependent on the chosen adaptation algorithm, as was seen in Table 3. The frequency response of the resulting filter may vary among other things depending on the optimal filter length for a particular SNR level. This can be seen in Figure 23, which illustrates the differences in filter frequency domain characteristics between the NLMS and RLS algorithms. With small filter lengths, the adaptive algorithms need to make a tradeoff between a smooth passband for vital sign frequencies, and sufficient noise attenuation outside the frequency band

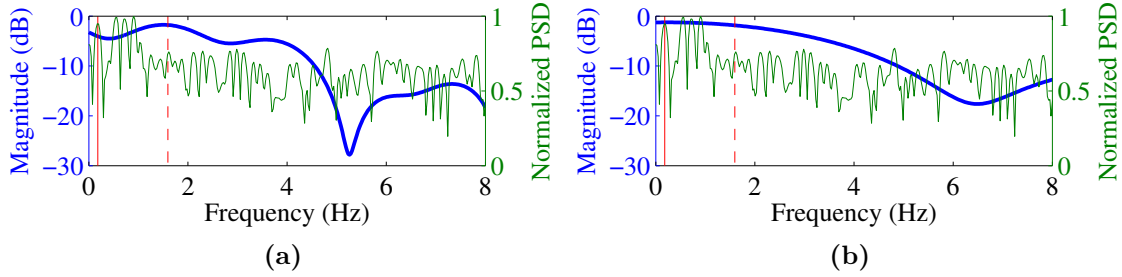


Figure 23: Adaptive filter frequency responses (bold blue line) using a) NLMS, and b) RLS algorithm at $\text{SNR} = 2$ dB. Simultaneous processing of both breathing (solid line) and heartbeat (dashed line) activities may result in attenuation of the vital sign frequencies if the filter length is not sufficient. The respective normalized signal frequency spectrums are displayed with the thin green lines.

of interest. As a result of the passband ripple, some of the vital sign frequencies may experience attenuation, but more importantly the breathing harmonics are not necessarily filtered out. This problem could be addressed by increasing the used filter lengths, which would lead to suboptimal performance in the MSE sense, or by processing the cardiopulmonary components individually. In order to demonstrate the gains obtained by adaptive filtering, this section presents the results for processing both breathing and heartbeat components together. Finding suboptimal filter lengths in the MSE sense was left outside of the scope of this thesis.

The operation of adaptive noise cancellation techniques is illustrated in Figure 24, where a sample data sequence of 5 seconds was processed with the presented methods using experimentally optimized parameters. Clearly, all of the illustrated methods are able to adapt the secondary input to the reference. By comparing the convergence of the NLMS and RLS methods in the IQ-time space, there is no significant difference between the two methods. However, by analyzing the MSE learning curves of both algorithms, it can be seen that the RLS converges slightly faster in general, see Figure 25a. However, this does not imply that the RLS would always have faster convergence, see Figure 25b, because the adaptation parameters are dependent on the observed data as was shown in Section 5.2. Moreover, it should be pointed out that independent of the SNR conditions, both the RLS and NLMS have approximately same steady state MSE. Therefore, it is necessary to use other criteria for evaluating algorithm performance.

Instead of the total MSE, more informative evaluation criteria for analyzing the algorithm performance are the obtained SNR gain, and the success rate of vital sign estimation following adaptive processing. These criteria give a better indication of how the different frequency components, such as micro-Doppler frequencies, are enhanced or attenuated during adaptive filtering.

The SNR gain of each techniques was evaluated by performing a series of 100 independent Monte-Carlo simulations, each consisting of 60 seconds of data sampled at 50 Hz for both receivers. This data was thereafter processed using the presented techniques in Section 4. The results are shown in Figure 26, where the input SNR

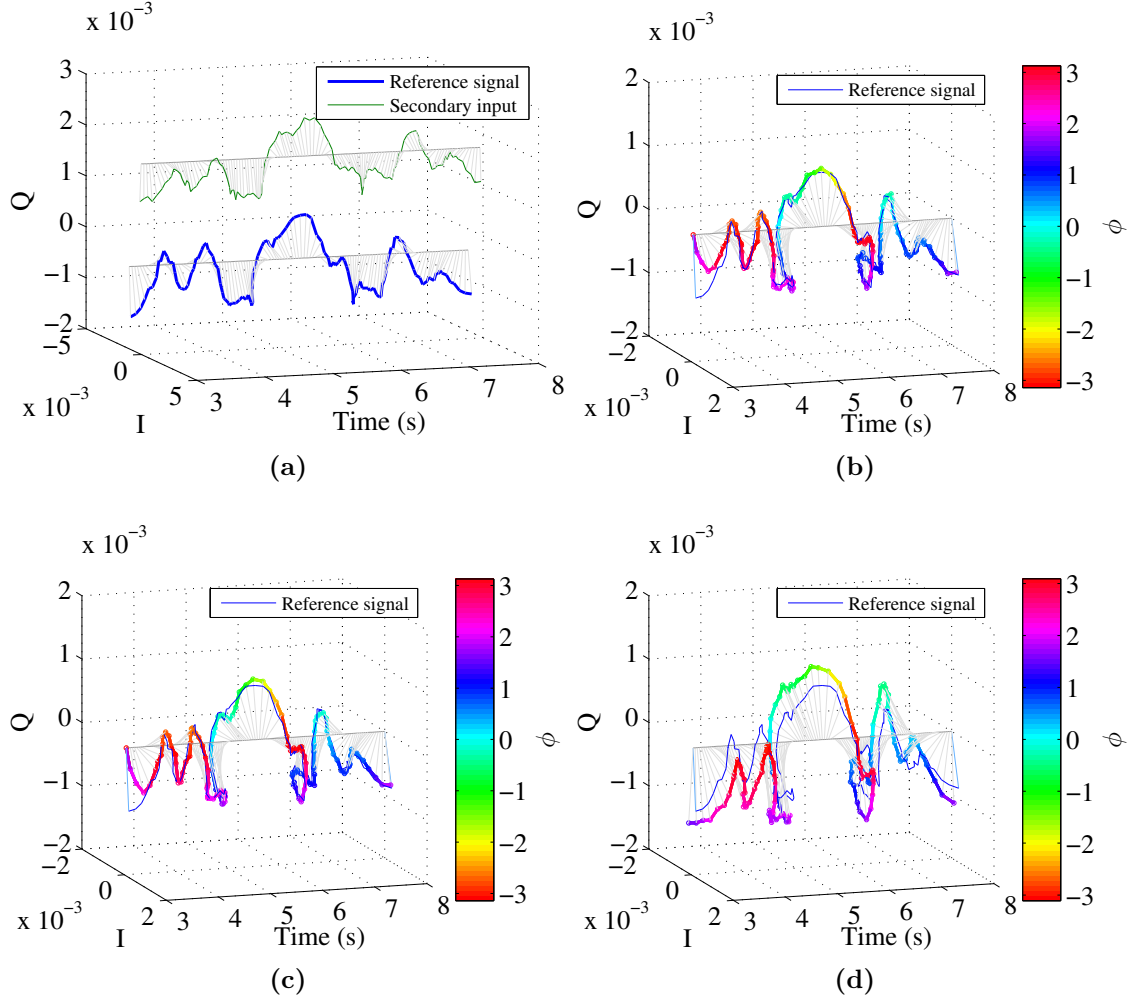


Figure 24: Operation of the adaptive processing techniques. a) Received vital sign signals, and output of b) NLMS, c) RLS, and d) MRC adaptive methods at SNR = 20 dB. The FIR filter techniques adapt to reference input, whereas the MRC performs coherent combining resulting in a larger signal radius in the IQ-plane.

before adaptive processing was defined as the maximum among all receive antennas

$$\text{SNR}_{\text{in}}(\text{dB}) = \max_m 10 \cdot \log_{10} \frac{a_m^2}{\sigma_w^2}, \quad (5.3.1)$$

where $m = 1 \dots M_R$, a_m^2 is the squared amplitude of the received signal arc at one receiver, and σ_w^2 is the variance of the respective white noise. The expression (5.3.1) is also the SNR of a SISO system that is used as a reference. The results indicate that the multiantenna adaptive techniques provide a notable output SNR gain when compared to using only one receiver, see Figure 26a. At low SNR regime, the adaptive filtering techniques outperform also the adaptive MRC. This is explained by the additional filter taps used for further noise cancellation, see (4.2.2). On the other hand, if the input SNR is increased above 7 dB, the gain from adaptive noise cancellation decreases slowly, whereas the MRC reaches a relatively steady gain of

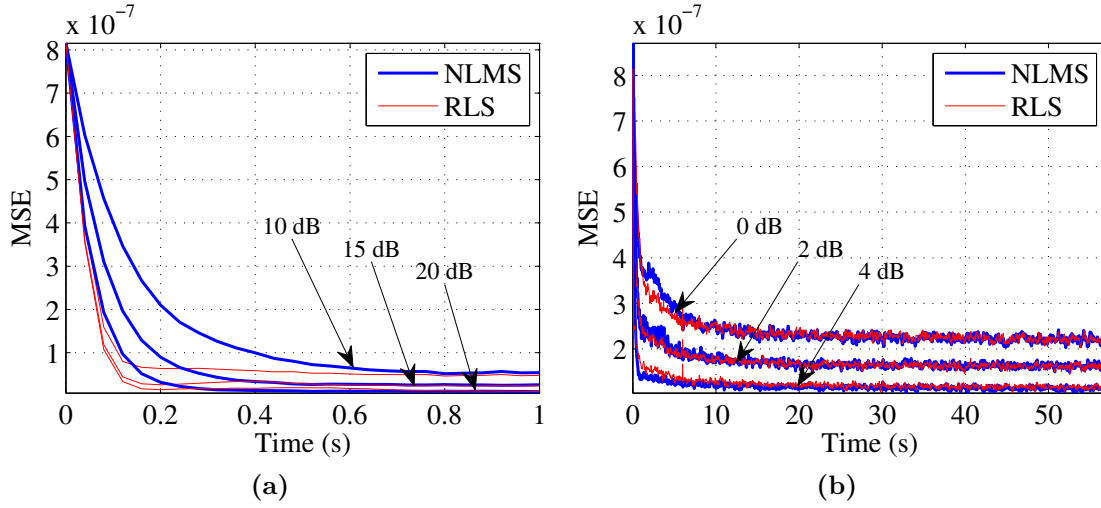


Figure 25: MSE learning curves of the NLMS and RLS adaptive algorithms evaluated over 1000 independent Monte-Carlo simulations at a) high SNR regime, b) low SNR regime. The rate of convergence and excess MSE depend on the experimentally optimized algorithm parameters and the receive SNR.

+3 dB through coherent combining of the receiver signals. Again, an intuitive explanation for this can be found by analyzing the adaptive filter parameters. As was shown in Table 3, the optimized filter length generally decreases with increasing the input SNR. Having too many degrees of freedom would result in following the noise and finding structures in the data that do not exist. Consequently, decreasing the filter length makes the filter transition band wider, thus resulting in worse noise cancelling performance. Nevertheless, using two receivers with the adaptive processing techniques enable operation at approximately 3 dB lower SNR, which is also the typical array gain of two receivers.

After enhancing the demodulated signals, the instantaneous breathing and heart-beat rates were estimated from the output signal $\hat{y}(k)$ using the MVDR spectrum estimator. The spectral estimates were computed from a window of 3 seconds of past data samples, and the estimates were updated once a second. A maximum error of $\pm 5\%$ was allowed to call an estimation successful. The instantaneous rate estimates of one simulation run are illustrated in Figure 27, showing the advantages of employing multiple receivers with adaptive processing techniques. Even at low input SNR regime adaptive filtering may improve the estimation success rate by up to 20 %-units compared to the case of using a one receiver SISO system, see Figure 26b. Therefore, in addition to the SNR gain, the multiantenna adaptive processing techniques also enable reliable vital sign estimation.

5.3.2 Results for Estimating Heartbeat Only

The vital sign estimation problem can be simplified for adaptive noise cancellation algorithms by removing the breathing component and estimating only the heartbeat

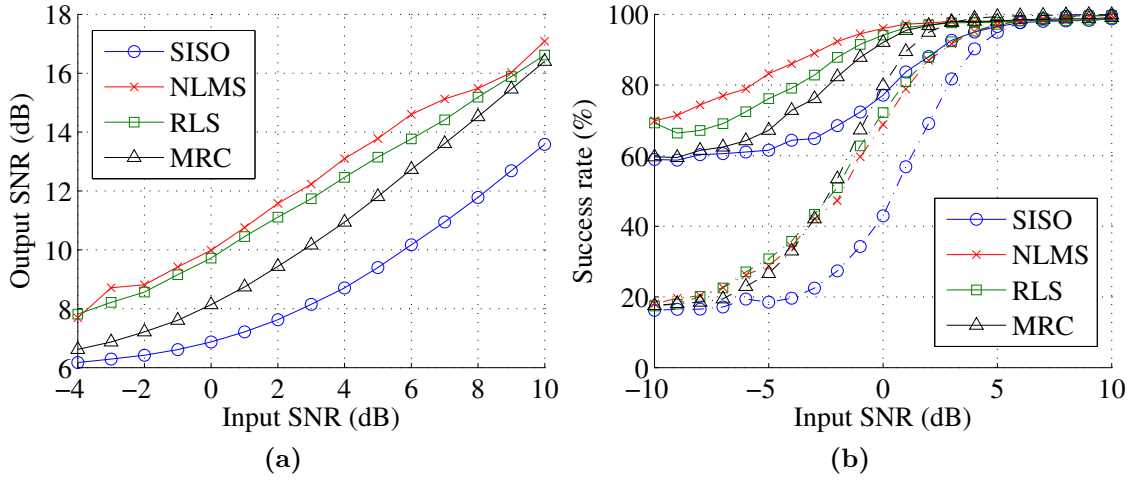


Figure 26: a) Adaptive processing techniques provide a significant output SNR gain, and b) improve the success rate of both heartbeat (dashed line) and breathing (solid line) rate estimates.

rates. Typically in sports and medicine, the heart rate is the vital sign of interest, and therefore breathing may be considered as nuisance in measurements. Removing the breathing component relaxes the passband width requirement for the designed adaptive filter, which enables a more accurate filter frequency response design, as can be seen in Figure 28. The resulting FIR filter has now a bandpass structure for enhancing the heartbeat frequencies, and the structure is emphasized especially with long filters.

In order for the adaptive methods to be able to focus on the heartbeat signal, the breathing component needs to be removed before adaptive processing. However, effective removal of the breathing component may be difficult due to the interfering harmonic terms that are present before signal demodulation. One possible solution would be to perform adaptive processing after signal demodulation, but this requires the use of linear demodulation due to the arctangent demodulation phase estimation problems that arise when the SNR is low. However, the application of linear demodulation is feasible only with small signal arc lengths in IQ plane, that is when the breathing component is not present, or the system operation frequency f_c is below K-band, as was shown in Section 3.2. Another option would be to use long bandpass filters for extracting the heartbeat component from the received signal, but this is problematic due to the breathing harmonics that may be present within the filter passband, and the exact heartbeat frequency is not known a priori. Furthermore, using tight bandpass pre-filters would already do most of the work for adaptive noise cancellation. For simplicity, the following simulations assume that the subject is holding his breath during monitoring, thus removing the problem of obtaining a breathing free signal for heartbeat estimation.

The results of applying these filters for estimating the heartbeat rates are illustrated in figure 29. By removing the breathing component and its harmonics, the average success rate of heartbeat rate estimates is increased substantially. The

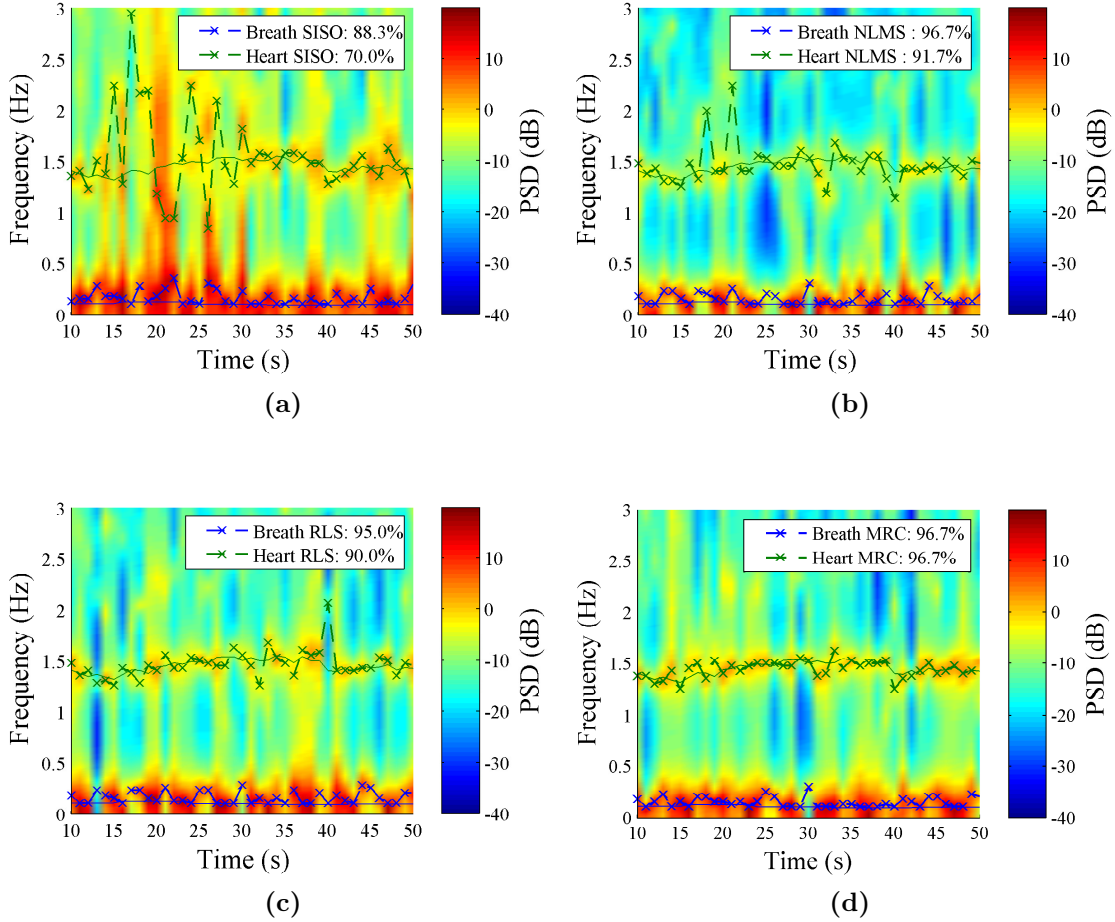


Figure 27: Time-frequency spectrum illustrating vital sign estimates and respective success rates for different methods, $\text{SNR}_{\text{in}} = 2$ dB. Solid lines represent true vital sign rates, and dashed lines the estimates of a) SISO with no adaptive processing, b) LMS, c) RLS, d) MRC. Multiantenna adaptive techniques have superior rate estimation performance compared to a SISO system.

adaptive noise cancellation techniques utilizing NLMS, RLS and MRC algorithms enable an acceptable estimation success rate of 80% still at an input SNR level of -9 to -7 dB. In contrast, when the breathing component was present, a corresponding performance for heartbeat estimation was obtainable at $\text{SNR}_{\text{in}} = 1$ dB. Thereby, the system heartbeat rate estimation dynamic range may be increased by up to 10 dB by effectively removing the breathing component along with its harmonics.

5.4 Simulation Results for Spatial Methods

The simulations were run using the system geometry of setup 2, see Section 5.1. In order to show the advantages of using multiple antennas in signal enhancement and directional interference cancelling, the simulations were run first with one subject,

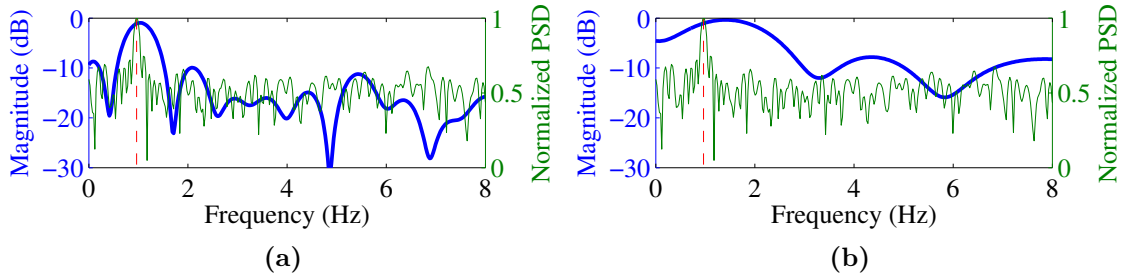


Figure 28: Adaptive noise cancellation filter frequency responses at $\text{SNR}_{\text{in}} = 2$ dB for estimating heartbeat only. a) The NLMS algorithm results in a bandpass filter amplifying the heartbeat (dashed line) frequencies, b) whereas the optimized RLS filter yields a shorter filter with smoother lowpass type frequency response.

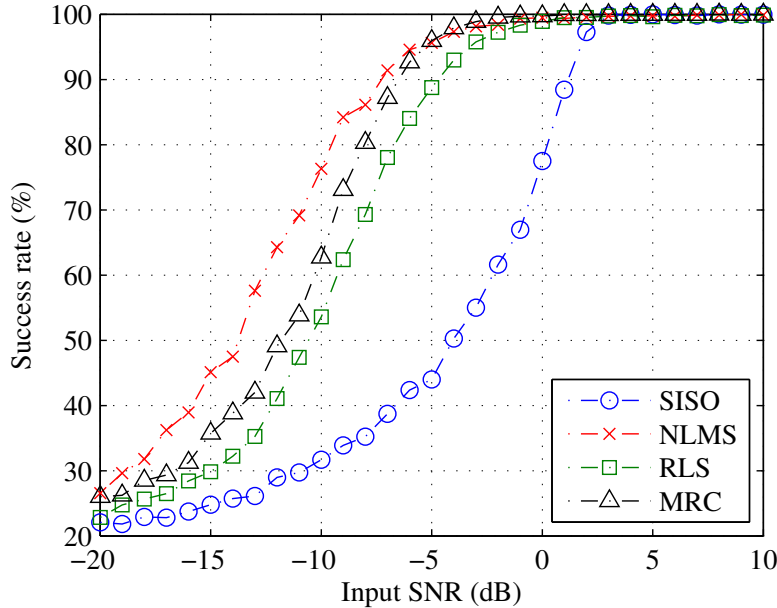


Figure 29: Removing the breathing component improves the heartbeat rate estimation success rate significantly compared to the case when both vital signs are estimated together, see Figure 26b. With low SNR values, it is necessary to use linear demodulation.

and then with two subjects in front of the transmitter. The performances of the multiantenna spatial methods were evaluated based on the obtained SNR gain, and vital sign estimation success rate. The results were compared to the case of using only one receiver.

5.4.1 Results for Beamforming on One Subject

The beampatterns and operation of the three different beamforming techniques in multiantenna vital sign monitoring are shown in Figure 30. As can be seen in Figure 30a, the conventional matched filter beamformer and robust Capon beamformer are able to correctly steer their beampatterns to the direction of the subject. In contrast,

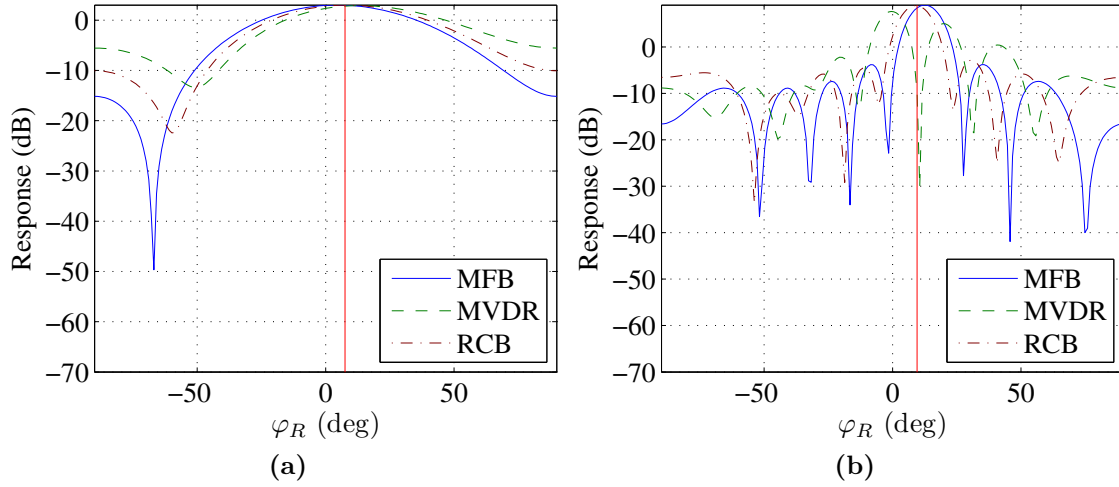


Figure 30: Beampatterns of MFB, MVDR, and RCB with a) 2 receiver antennas, and b) 8 receiver antennas under $\text{SNR}_{\text{in}} = 2$ dB. Red line represents the approximate angular location of the subject. A two antenna array has only one degree of freedom for signal enhancement or interference cancelling. With multiple receivers, the MVDR tries to place a null in the direction of the signal of interest due to the robustness issues discussed in Section 4.3.2.

when the estimated signal DoA contains error, the MVDR beamformer tries to place a null in this direction due to the robustness issues that were discussed in Section 4.3.2. As a result, the MFB and RCB are able to enhance the signals carrying the vital signs, whereas the MVDR sees the signals as interference and attenuates them. Although the problems with MVDR are not that significant with using only two receivers, increasing the number of receive antennas emphasizes its unrobustness, as can be seen in Figure 30b. Consequently, the following performance analysis is focused on the two former beamforming techniques.

The results of applying the presented beamforming techniques for estimating the vital signs of one subject are shown in Figure 31. Using the beamforming techniques with two closely spaced receivers may improve the receive output SNR by up to 3 dB, as is seen in Figure 31a. This is almost equivalent to the SNR gain obtained by adaptive noise cancellation techniques, such as the MRC. Furthermore, increasing the array aperture by adding more receivers gives a better angular resolution and more degrees of freedom for resolving the signal of interest and possible interferers. In addition, there is a subtle advantage of applying the RCB over the MFB, because the former technique attempts to attenuate any directional interference passing through the sidelobes, while the MFB simply maximizes the gain towards the subject without any sidelobe optimization. However, with small antenna apertures, that is with a small number of antennas, the difference between these two beamforming techniques is not significant. The corresponding advantage in view of the vital sign estimation success rate is shown in Figure 31b.

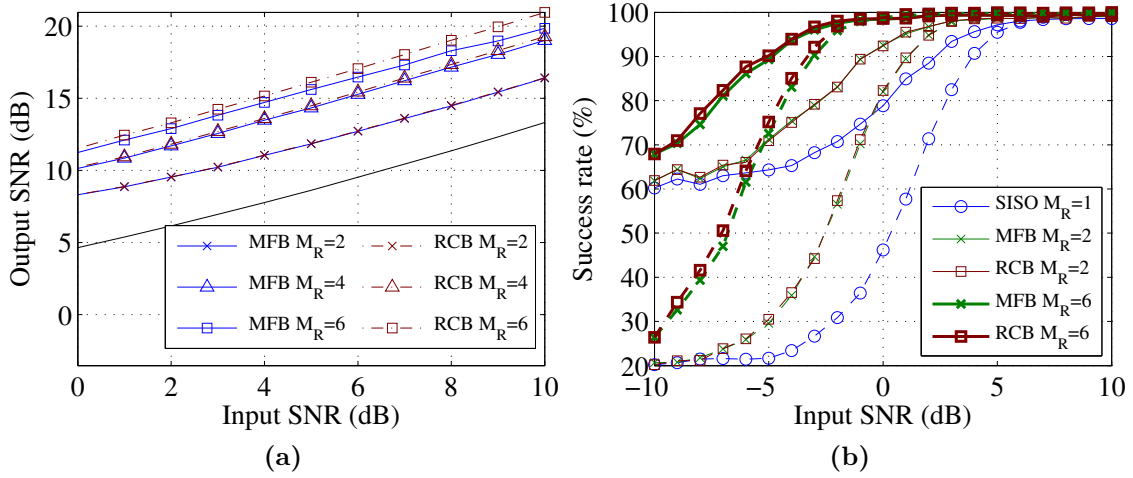


Figure 31: a) MFB and RCB techniques provide a significant output SNR gain, and b) improve the success rate of both heartbeat (dashed line) and breathing (solid line) rate estimates.

5.4.2 Results for Directional Interference Cancelling

In addition to enhancing the vital sign signals in a particular direction by steering the receiver beampattern, the beamforming techniques may be used to cancel directional interference, see Section 4.3.2 and 4.3.3. To evaluate the interference cancelling capabilities of the MFB and RCB techniques, the second simulation setup was modified to include a secondary subject, see Figure 32. To further show the beamforming gain dependency on the angular displacement of the two subjects, the position of the secondary subject as well as the number of receiver antennas was varied.

The advantage of beamforming techniques in attenuating the reflections from the secondary subject are illustrated in Figure 33. By analyzing the spectrum of a demodulated input of only one receive antenna, see Figure 33b, it is hard to separate the cardiopulmonary rates of the two subjects unless there is a significant difference in the respective breathing and heartbeat rates. However, if the angular location of the primary subject is known or estimated from the data, the multiantenna beamforming techniques may be used to suppress reflections from sources of interference, see Figure 33d. Thereafter, the vital sign of the primary subject may be estimated accurately. It was assumed in all simulations that a priori approximate knowledge of the primary subject angular location was available. Without this assumption, secondary subjects closer to the radar could result in significant estimation errors.

The results of interference cancelling beamforming in vital sign estimation are shown in Figure 34. When vital sign reflections are observed from two subjects, the single receiver SISO system with omnidirectional antenna does not have the required angular resolution to identify different sources. With multiple receivers however, the beamforming techniques may be used to attenuate the interference, and therefore

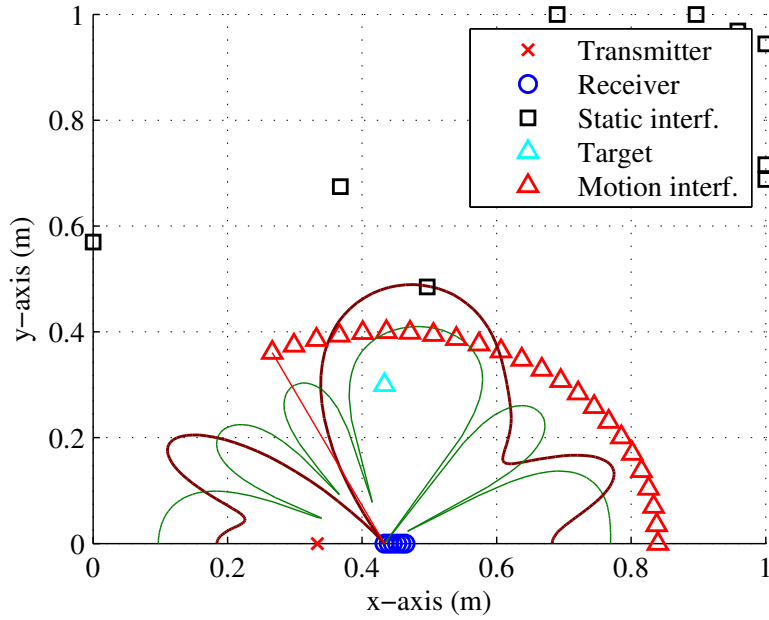


Figure 32: Beamforming technique interference cancelling capabilities were evaluated by placing a secondary subject in range of the radar system, and varying the angular displacement between the primary and secondary subjects. Beampatterns of RCB and MFB are illustrated by bold solid red, and solid green lines respectively.

improve the SINR defined as

$$\text{SINR}(\text{dB}) = \log_{10} \frac{a_m^2}{\sigma_{i+w}^2}, \quad (5.4.1)$$

where σ_{i+w}^2 is the radial variance resulting from interference and white noise. The MFB and RCB have roughly identical SINR performance in attenuating secondary vital signs, see Figure 34a. Typically, the RCB has superior interference cancelling capabilities compared to MFB, due to data independent sidelobes of MFB. However, if the directional interference is not overpowering the primary signal, the MFB and RCB techniques yield similar beampatterns as a result of focusing most of the receiver gain towards the primary signal of interest. The skewness of receiver SINR performance is caused by the displacement of the transmitter and receiver.

There is a clear loss in performance when the two reflection points are closely spaced, and thus illuminated by the beampattern main lobe. This results in amplification of both signals, thus thwarting the advantage of directional interference cancelling. Nevertheless, since the RCB is specifically designed to enhance the primary signal while still attenuating interference in other directions, it obtains a slightly better interference cancelling performance compared to the MFB. Therefore, the RCB is preferred in multiantenna applications where the primary signal is weak, or overpowered by interference from the environment.

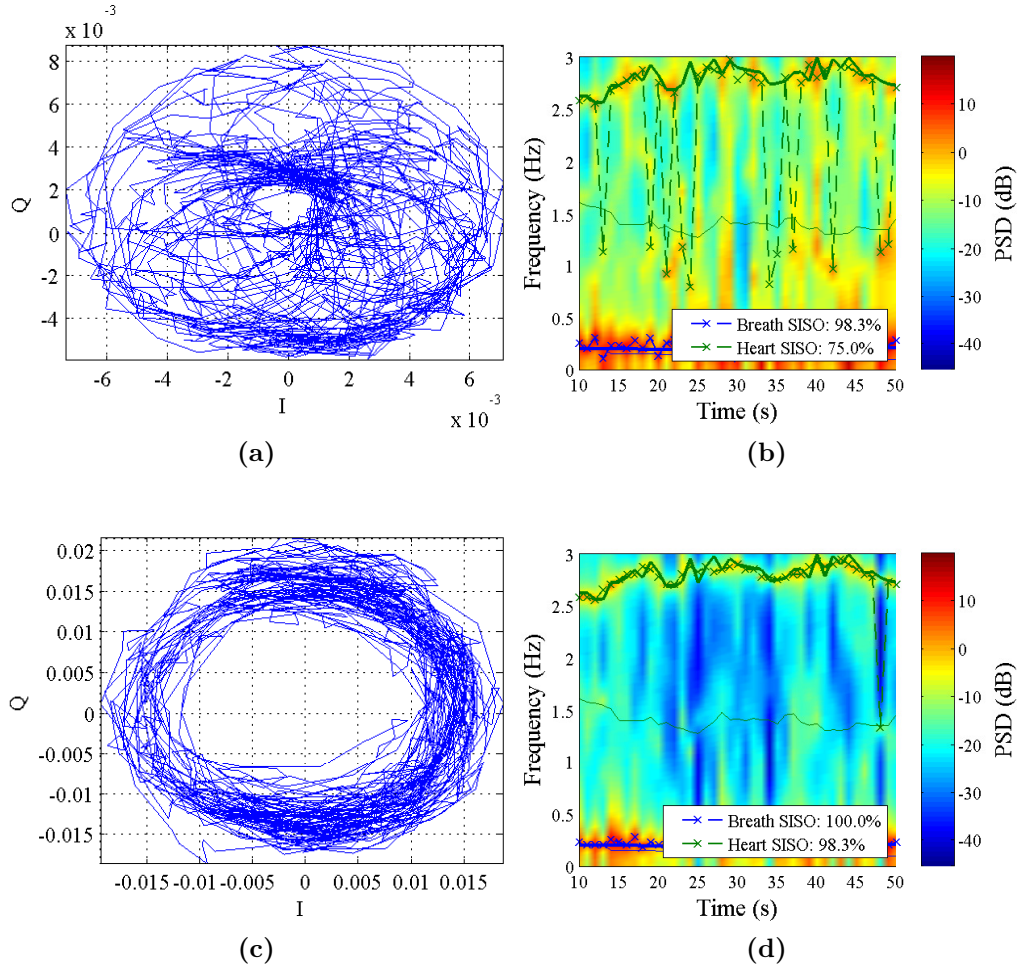


Figure 33: Beamforming techniques may be used to suppress directional interference. Figures a) and b) show the single receiver signal in both time and frequency domain, illustrating the interference caused by the presence of a secondary subject vital signs. Figures c) and d) show the respective outputs of the RCB technique applied for $M_R = 6$ receivers. True instantaneous primary and secondary subject cardiopulmonary frequencies are denoted by bold solid, and solid lines respectively, $\text{SNR}_{\text{in}} = 20$ dB. There is a clear advantage of multiantenna beamforming techniques in interference cancelling.

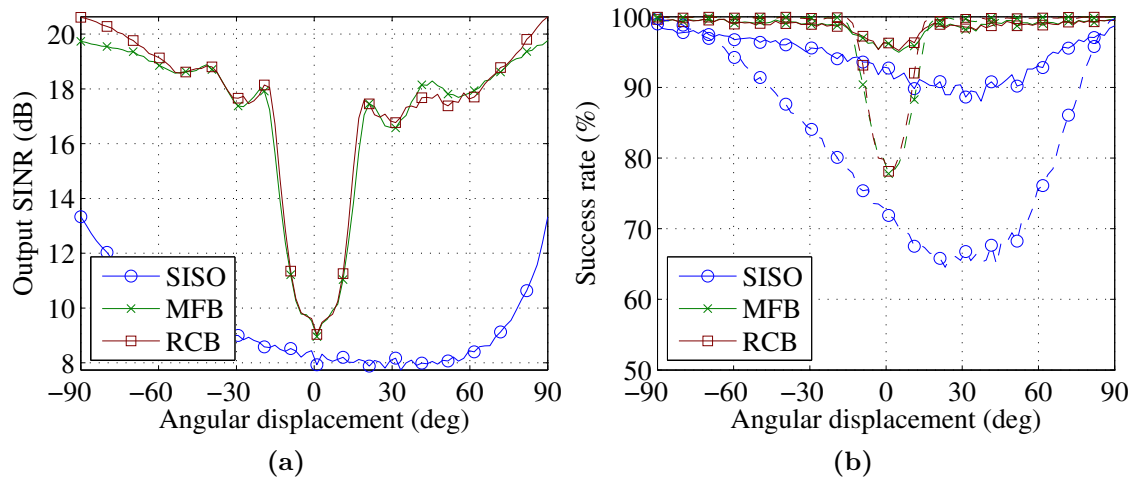


Figure 34: Performance of spatial interference cancelling as a function of primary and secondary subject angular displacement. a) MFB and RCB techniques provide a significant output SNR gain, and b) improve the success rate of both heartbeat (dashed line) and breathing (solid line) rate estimates. $\text{SNR}_{\text{in}} = 10$ dB.

6 Summary

The purpose of this thesis was to study the applicability and performance of different adaptive processing techniques for multiantenna vital sign estimation. To enable accurate modeling of human vital signs, mathematical motion models were derived for both cardiopulmonary activities based on the physiology and dynamics of heartbeat and breathing. Also, a realistic signal propagation model was derived for multiantenna receiver systems. Three different adaptive processing techniques were presented to increase the reliability and dynamic range of wireless vital sign monitoring systems. The main contribution of the thesis was the novel application of adaptive filtering in vital sign estimation to improve the performance of multiantenna vital sign monitoring. Finally, a paper on the presented adaptive methods was written and submitted to the 2013 IEEE Radar Conference [16].

The applicability and performance of these multiantenna adaptive processing techniques were evaluated based on extensive simulations using the derived realistic signal propagation model. Based on the simulations, the adaptive methods improve the output SNR and success rate of vital sign estimation, and may thus be used to increase the reliability and operation range of wireless multiantenna CW radar vital sign monitoring systems. This section gives a brief summary of the adaptive techniques and respective simulations, and presents discussion on applications and practical limitations of these methods within the field of vital sign monitoring.

6.1 Discussion

6.1.1 Performance and Application of Adaptive Techniques

The simulation results showed that the presented adaptive filtering techniques provide a superior vital sign estimation performance in low SNR, as compared to simply phase aligning the signals with MRC. The advantage of the adaptive noise cancellation methods was based on the additional filter taps used to bandpass filter the vital sign components, while still attenuating the wideband additive noise. This advantage was emphasized when the breathing component was removed to allow shorter transition bandwidth in the FIR filter design, thus improving the success rate of heartbeat estimation.

Although the adaptive noise cancellation techniques were shown to have good performance and relatively low computational complexity, the main drawback of these methods is the problem of adaptation parameter optimization. Fortunately, the vital sign estimation performance is not too sensitive to the choice of adaptation parameters, although subtle differences may be achieved by careful selection of these values. While there is no closed form solution available for choosing these values, the main computational burden lies in pre-computing the parameters. Nevertheless, the adaptive noise cancellation methods, unlike the spatial methods, are not that sensitive to the receiver array geometry, but perform well even if the receivers are widely separated.

If the receiver is disturbed by directional motion clutter, the spatial methods outperform the adaptive filtering techniques, as the latter methods rely on temporal

processing. Due to this limitation, they are unable to identify or separate signals in the spatial domain. Thereby, the adaptive noise cancellation techniques are suitable for single subject vital sign estimation applications with low background motion clutter and moderate computational resources for parameter optimization. On contrary, the RCB is applicable to single source vital sign monitoring even under high directional motion clutter, and is virtually parameter free.

6.1.2 Array Size Considerations

In practice, building a radar array operating at 24 GHz with antenna interelement spacing $\lambda/2 \approx 6.2$ mm may impose implementation challenges. Compared to the wavelength, the sheer physical size of the individual sensors could prohibit assembly of such a fine array structure. However, due to recent advances in micro and nano-scale semiconductor manufacturing technologies, there exist electromagnetic sensor manufacturers like Fujitsu and Intel that are capable of producing antenna elements on millimeter scale. This could eventually lead to embedding such high frequency sensors in mobile devices such as smartphones. If these radars should become a new emerging standard within mobile phones, the growing high demand on the sensors could reduce the component prices, thus enabling a wider range of applications. This happened for example with CMOS active pixel sensors in the early 1990's when the digital camera was irreversibly integrated to mobile phones.

Even if the price of the array sensors would become affordable, another complexity and scaling issue would rise from fitting individual RF frontends behind each array element. As opposed to fixed beampattern directional array, each antenna element would require A/D conversion and IQ sampling circuitry to enable any of the adaptive signal enhancement techniques presented in this thesis. Therefore, it is not just the size of the sensors, but one has to consider the entire radar system when designing new applications.

An obvious solution to these physical constraints laid out by the operation frequency is to use a larger antenna interelement spacing. Although the noise cancellation techniques are not as sensitive of receiver geometry, see Section 5.3, increasing antenna spacing results in undersampling for spatial methods, thus leading to aliasing and unwanted grating lobes. Furthermore, while the far field distance is proportional to the square of array geometric dimension, increasing antenna interelement spacing would significantly increase the minimum operation range of the array for beamforming techniques. For example, a six element array with $\lambda/2$ spacing has a theoretical far field starting at 22.5 cm, whereas the far field for a similar array with an increased antenna element spacing of λ begins at 90 cm.

Another disadvantage of small sensors is their smaller output transmit power. As indicated by the general radar equation (2.3.2), the maximum operation range is highly dependent on the array to target distance and the transmitted signal power. Therefore, a low transmit power would further constrain the efficient operation range of the system.

6.2 Conclusion

This thesis addressed the problem of vital sign estimation with the application of adaptive signal enhancement techniques using multiantenna CW radar. Three adaptive processing techniques were proposed, along with a realistic multiantenna signal propagation model. The goal with the adaptive techniques was to enhance the signals carrying the cardiopulmonary micro-Doppler information through coherent combining of multiple receive inputs, while still attenuating directional interference and noise.

The simulation results showed that high frequency CW radar systems equipped with multiple receive antennas may be used to address the problem of vital sign monitoring under low SNR conditions. Also, it was shown that the proposed adaptive noise cancellation techniques may be used in arbitrary receiver array geometry to provide a significant increase in vital sign rate estimation accuracy, and to enable operation at lower SNR conditions. In contrast, in addition to the increased SNR gain, the spatial beamforming methods relying on compact receiver geometry were shown to provide good directional interference cancelling capabilities.

While the main challenge with online location independent healthcare services is the lack of compact and reliable mobile medical sensors, the presented techniques were shown to provide robust tools for accurate wireless vital sign monitoring. As a result of the low complexity algorithms, these techniques are well applicable also in mobile devices with limited processing power and battery lifetime. Also, as the physical size of electronic components is constantly getting smaller, it will be possible to embed multiantenna sensors to various devices including mobile phones.

6.3 Future Work

It was shown in this thesis that both adaptive noise cancellation and spatial processing techniques can be used to improve the output SNR in a multiantenna receiver radar system. The adaptive filter techniques were however only applied to a two receiver radar. Thereby, future studies should focus on the advantages of concatenating the noise cancelling filters for more than two inputs. To further improve the robustness and reliability of vital sign monitoring, the application of multiple transmit antennas should be considered. This would allow transmit beamforming, thus enabling more efficient use of transmit resources through focusing the transmitted energy on the primary subject only.

Another approach to interference cancellation and separation of closely spaced targets is to apply space-time adaptive processing techniques. These techniques are based on spatial array processing with pulse-Doppler signals, and are applied in for example airborne radar systems to account for radar platform motion and suppression of directional ground clutter [60]. It would be interesting to study the applicability of STAP in vital sign monitoring for random body movement cancellation.

One further interesting approach to separating the vital sign components from excess motion clutter in multiantenna CW radar is the application of ICA. While

ICA has been shown to work for separating individual breathing and heartbeat components, it would be interesting to study the advantages of ICA in random body movement cancellation, since any interfering motion such as hand waving and head nodding, should intuitively be uncorrelated with the cardiopulmonary activities.

References

- [1] J. Lin, "Noninvasive microwave measurement of respiration," *Proceedings of the IEEE*, vol. 63, no. 10, p. 1530, oct. 1975.
- [2] K. Chen, D. Mirsa, H. Wang, H. Chuang, and E. Postow, "An x-band microwave life detection system," *IEEE Transactions on Biomedical Engineering*, vol. 33, pp. 697–702, 1986.
- [3] K. Chen, Y. Huang, J. Zhang, and A. Norman, "Microwave life-detection systems for searching human subjects under earthquake rubble or behind barrier," *IEEE Transactions on Biomedical Engineering*, vol. 47, no. 1, pp. 105 –114, jan. 2000.
- [4] O. Boric-Lubecke, V. Lubecke, A. Host-Madsen, D. Samardzija, and K. Cheung, "Doppler radar sensing of multiple subjects in single and multiple antenna systems," in *Telecommunications in Modern Satellite, Cable and Broadcasting Services, 2005. 7th International Conference on*, vol. 1, sept. 2005, pp. 7 – 11 vol. 1.
- [5] D. Smardzija, O. Boric-Lubecke, A. Host-Madsen, V. Lubecke, I. Sizer, T., A. Droitcour, and G. Kovacs, "Applications of MIMO techniques to sensing of cardiopulmonary activity," in *Wireless Communications and Applied Computational Electromagnetics, 2005. IEEE/ACES International Conference on*, april 2005, pp. 618 – 621.
- [6] V. Chen, F. Li, S.-S. Ho, and H. Wechsler, "Micro-doppler effect in radar: phenomenon, model, and simulation study," *IEEE Transactions on Aerospace and Electronic Systems*, vol. 42, no. 1, pp. 2 – 21, jan. 2006.
- [7] T. Sparr and B. Krane, "Micro-doppler analysis of vibrating targets in SAR," *IEE Proceedings on Radar, Sonar and Navigation*, vol. 150, no. 4, pp. 277–83, aug. 2003.
- [8] V. Chen, F. Li, S.-S. Ho, and H. Wechsler, "Analysis of micro-doppler signatures," *IEE Proceedings Radar on Sonar and Navigation*, vol. 150, no. 4, pp. 271–6, aug. 2003.
- [9] H. Gao, L. Xie, S. Wen, and Y. Kuang, "Micro-doppler signature extraction from ballistic target with micro-motions," *IEEE Transactions on Aerospace and Electronic Systems*, vol. 46, no. 4, pp. 1969 –1982, oct. 2010.
- [10] A. Ghaleb, L. Vignaud, J. M. Nicolas, and A. Ghaleb, "A refine micro-doppler analysis of pedestrians in ISAR imaging," *7th European Conference on Synthetic Aperture Radar (EUSAR), 2008*, pp. 1 –4, june 2008.
- [11] L. Vignaud, A. Ghaleb, J. Le Kernec, and J.-M. Nicolas, "Radar high resolution range & micro-doppler analysis of human motions," in *International Radar Conference - Surveillance for a Safer World, 2009*, oct. 2009, pp. 1 –6.

- [12] C. Li, J. Cummings, J. Lam, E. Graves, and W. Wu, "Radar remote monitoring of vital signs," *IEEE Microwave Magazine*, vol. 10, no. 1, pp. 47–56, february 2009.
- [13] J. Salmi, O. Luukkonen, and V. Koivunen, "Continuous wave radar based vital sign estimation: Modeling and experiments," in *IEEE Radar Conference (RADAR)*, 2012, may 2012, pp. 0564–0569.
- [14] D. Hoyer, K. Schmidt, R. Bauer, U. Zwiener, M. Kohler, B. Luthke, and M. Eiselt, "Nonlinear analysis of heart rate and respiratory dynamics," *IEEE Engineering in Medicine and Biology Magazine*, vol. 16, no. 1, pp. 31–39, jan.-feb. 1997.
- [15] L. Changzhi, L. Jun, L. Jian, and L. Jenshan, "Accurate doppler radar noncontact vital sign detection using the RELAX algorithm," *IEEE Transactions on Instrumentation and Measurement*, vol. 59, no. 3, pp. 687–695, march 2010.
- [16] J. Aho, J. Salmi, and V. Koivunen, "Adaptive processing and realistic signal propagation modeling for multiantenna vital sign radar," in *IEEE Radar Conference*, 2013, may. 2013.
- [17] A. C. Guyton and J. E. Hall, *Textbook of Medical Physiology*. Philadelphia: Elsevier, 2006.
- [18] R. Davies-Jones and V. Wood, "Simulated doppler velocity signatures of evolving tornado-like vortices," *Journal of Atmospheric and Oceanic Technology*, vol. 23, no. 8, pp. 1029–1048, aug. 2006.
- [19] M. Skolnik, *Radar handbook*. New York, NY: McGraw-Hill, 1970.
- [20] D. Miller, *The Illustrated Directory of Modern American Weapons*. London: Salamander Books, 2002.
- [21] D. Bliss and K. Forsythe, "Multiple-input multiple-output (MIMO) radar and imaging: degrees of freedom and resolution," in *Signals, Systems and Computers, 2003. Conference Record of the Thirty-Seventh Asilomar Conference on*, vol. 1, nov. 2003, pp. 54–59 Vol.1.
- [22] A. Haimovich, R. Blum, and L. Cimini, "MIMO radar with widely separated antennas," *IEEE Signal Processing Magazine*, vol. 25, no. 1, pp. 116–129, 2008.
- [23] J. Li and P. Stoica, "MIMO radar with colocated antennas," *IEEE Signal Processing Magazine*, vol. 24, no. 5, pp. 106–114, sept. 2007.
- [24] Q. Zhou, J. Liu, A. Host-Madsen, O. Boric-Lubecke, and V. Lubecke, "Detection of multiple heartbeats using doppler radar," in *IEEE International Conference on Acoustics, Speech and Signal Processing*, 2006, vol. 2, may 2006, p. II.

- [25] A. Sihvola and I. Lindell, *Sähkömagneettinen kenttäteoria 2 Dynaamiset kentät*, 3rd ed. Otatieto, 2002.
- [26] G. Camelia, “Compilation of the dielectric properties of body tissues at RF and microwave frequencies.” King’s Coll London (United Kingdom) Dept. of Physics, Tech. Rep., 1996.
- [27] J. Salmi and A. Molisch, “Propagation parameter estimation, modeling and measurements for ultrawideband MIMO radar,” *IEEE Transactions on Antennas and Propagation*, vol. 59, no. 11, pp. 4257–4267, nov. 2011.
- [28] D. Manolakis, V. Ingle, and S. Kogon, *Statistical and Adaptive Signal Processing: Spectral Estimation, Signal Modeling, Adaptive Filtering and Array Processing*. Norwood: Artech House, 2005.
- [29] J. Salmi, “Statistical modeling and tracking of the dynamic behavior of radio channels,” Master’s Thesis, Helsinki University of Technology, 2005.
- [30] C. Li and J. Lin, “Complex signal demodulation and random body movement cancellation techniques for non-contact vital sign detection,” in *IEEE MTT-S International Microwave Symposium Digest, 2008*, june 2008, pp. 567–570.
- [31] B.-K. Park, A. Vergara, O. Boric-Lubecke, V. Lubecke, and A. Host-Madsen, “Quadrature demodulation with DC cancellation for a doppler radar motion detector,” Dept. of Electrical Engineering, University of Hawaii, Tech. Rep., 2007.
- [32] M. Zakrzewski, H. Raittinen, and J. Vanhala, “Comparison of center estimation algorithms for heart and respiration monitoring with microwave doppler radar,” *IEEE Sensors Journal*, vol. 12, no. 3, pp. 627–634, march 2012.
- [33] N. Chernov and C. Lesort, “Least squares fitting of circles,” *Journal of Mathematical Imaging and Vision*, vol. 23, pp. 239–252, 2005, 10.1007/s10851-005-0482-8. [Online]. Available: <http://dx.doi.org/10.1007/s10851-005-0482-8>
- [34] P. Stoica and R. Moses, *Spectral Analysis of Signals*. New Jersey: Pearson Prentice Hall, 2005.
- [35] G. Proakis, C. Rader, F. Ling, C. Nikias, M. Moonen, and I. Proudler, *Algorithms for statistical signal processing*. New Jersey, USA: Prentice Hall, 2002.
- [36] J. Capon, “High-resolution frequency-wavenumber spectrum analysis,” *Proceedings of the IEEE*, vol. 57, no. 8, pp. 1408–1418, aug. 1969.
- [37] J. Aho, “Comparison and application of spectral estimation methods: Vital sign estimation,” Dept. of Signal Processing and Acoustics, Aalto University, Tech. Rep., 2012.

- [38] J. Benesty, J. Chen, and Y. Huang, "Recursive and fast recursive capon spectral estimators," *EURASIP J. Appl. Signal Process.*, vol. 2007, no. 1, pp. 23–23, Jan. 2007. [Online]. Available: <http://dx.doi.org/10.1155/2007/45194>
- [39] L. Cohen, *Time-frequency analysis*. Prentice Hall PTR Englewood Cliffs, New Jersey, 1995, vol. 778.
- [40] J. Ville, "Theorie et applications de la notion de signal analytique," *Cables et transmission*, vol. 2, no. 1, pp. 61–74, 1948.
- [41] L. Stankovic, "A method for time-frequency analysis," *IEEE Transactions on Signal Processing*, vol. 42, no. 1, pp. 225–229, 1994.
- [42] P. Rakovic, E. Sejdic, L. Stankovic, and J. Jiang, "Time-frequency signal processing approaches with applications to heart sound analysis," in *Computers in Cardiology, 2006*. IEEE, 2006, pp. 197–200.
- [43] A. Host-Madsen, N. Petrochilos, O. Boric-Lubecke, V. Lubecke, B. Park, and Q. Zhou, "Signal processing methods for doppler radar heart rate monitoring," *Signal Processing Techniques for Knowledge Extraction and Information Fusion*, pp. 121–140, 2008.
- [44] C. Li and J. Lin, "Random body movement cancellation in doppler radar vital sign detection," *IEEE Transactions on Microwave Theory and Techniques*, vol. 56, no. 12, pp. 3143–3152, dec. 2008.
- [45] D. Smardzija, O. Boric-Lubecke, A. Host-Madsen, V. Lubecke, T. Sizer, A. Droitcour, G. Kovacs, *et al.*, "Applications of mimo techniques to sensing of cardiopulmonary activity," in *IEEE/ACES International Conference on Wireless Communications and Applied Computational Electromagnetics, 2005*. IEEE, 2005, pp. 618–621.
- [46] B. Widrow, P. Mantey, L. Griffiths, and B. Goode, "Adaptive antenna systems," *Proceedings of the IEEE*, vol. 55, no. 12, pp. 2143–2159, dec. 1967.
- [47] S. Haykin, *Adaptive filter theory*, 4th ed. Prentice-Hall, Englewood-Cliffs, NJ, 2003.
- [48] H. Sayed and M. Rupp, "Robustness issues in adaptive filtering," in *The Digital Signal Processing Handbook*. New York: CRC Press, 1998, ch. 20.
- [49] S. Ljung and L. Ljung, "Error propagation properties of recursive least-squares adaptation algorithms," *Automatica*, vol. 21, no. 2, pp. 157–167, 1985. [Online]. Available: <http://www.sciencedirect.com/science/article/pii/0005109885901104>
- [50] J. Li, P. Stoica, and Z. Wang, "On robust capon beamforming and diagonal loading," *IEEE Transactions on Signal Processing*, vol. 51, no. 7, pp. 1702–1715, july 2003.

- [51] V. Koivunen, "Comparison of robust beamforming techniques," Helsinki University of Technology, P.O Box 3000, Finland, Tech. Rep., 2012.
- [52] H. Krim and M. Viberg, "Two decades of array signal processing research: the parametric approach," *IEEE Signal Processing Magazine*, vol. 13, no. 4, pp. 67–94, jul 1996.
- [53] A. Hyvärinen and E. Oja, "Independent component analysis: algorithms and applications," *Neural networks*, vol. 13, no. 4, pp. 411–430, 2000.
- [54] R. Vigário, V. Jousmäki, M. Haemaelaeninen, R. Haft, and E. Oja, "Independent component analysis for identification of artifacts in magnetoencephalographic recordings," *Advances in neural information processing systems*, pp. 229–235, 1998.
- [55] K. Kiviluoto and E. Oja, "Independent component analysis for parallel financial time series," in *Proceedings of International Conference on Neural Information Processing, 1998*, vol. 2, 1998, pp. 895–898.
- [56] M. Zakrzewski and J. Vanhala, "Separating respiration artifact in microwave doppler radar heart monitoring by independent component analysis," in *IEEE Sensors, 2010*. IEEE, 2010, pp. 1368–1371.
- [57] N. Petrochilos, M. Rezk, A. Host-Madsen, V. Lubecke, and O. Boric-Lubecke, "Blind separation of human heartbeats and breathing by the use of a doppler radar remote sensing," in *IEEE International Conference on Acoustics, Speech and Signal Processing, 2007*, vol. 1. IEEE, 2007, pp. I–333.
- [58] A. Hyvarinen, "Fast and robust fixed-point algorithms for independent component analysis," *IEEE Transactions on Neural Networks*, vol. 10, no. 3, pp. 626–634, 1999.
- [59] M. Belrhiti, S. Bri, A. Nakheli, M. Haddad, and A. Mamouni, "Complex permittivity measurement for dielectric materials at microwave frequencies using rectangular waveguide," *European Journal of Scientific Research*, vol. 49, no. 2, pp. 234–248, 2011.
- [60] R. Klemm, *Principles of space-time adaptive processing*. Inspec/Iee, 2002, no. 159.

A Convergence Analysis of LMS Algorithm

This appendix gives a detailed convergence analysis of the LMS algorithm. The LMS algorithm is based on the steepest decent approach to iteratively compute the filter coefficients starting from an initial guess of $\mathbf{h}(0) = \mathbf{0}$. The goal is to minimize the MSE, see eq. (4.2.7), by updating the filter coefficients in the direction of the negative gradient. Instead of using the true gradient, LMS employs a gradient approximation based on the instantaneous squared error

$$\nabla_{\mathbf{h}} e^2(k) \approx -2e(k)\mathbf{x}(k), \quad (\text{A1})$$

thus resulting in an iterative update rule given in (4.2.15), which is repeated here for convenience

$$\mathbf{h}(k+1) = \mathbf{h}(k) - 2\beta e(k)\mathbf{x}(k). \quad (\text{A2})$$

A simple approach to analyze the convergence of the algorithm is to take the expectation of the weight coefficients $\mathbf{h}(\mathbf{k})$ in (A2) after a large number of iterations, thus yielding

$$\begin{aligned} E\{\mathbf{h}(k+1)\} &= E\{\mathbf{h}(k)\} - 2\beta E\{(y(k) - \mathbf{h}^H(k)\mathbf{x}(k))\mathbf{x}(k)\} \\ &= [\mathbf{I} + 2\beta\mathbf{R}_{xx}(k)] E\{\mathbf{h}(k)\} - 2\beta\mathbf{r}_{xy}(k), \end{aligned} \quad (\text{A3})$$

where \mathbf{I} is the identity matrix, and $\mathbf{R}_{xx}(k)$ and $\mathbf{r}_{xy}(k)$ are the respective instantaneous auto- and cross-correlation matrices. Here it is assumed that $\mathbf{h}(k)$ is independent of $\mathbf{x}(k)$, which based on the assumption that the delay between successive iterations of the LMS algorithm is long enough so that sample inputs vectors $\mathbf{x}(k)$ and $\mathbf{x}(k+1)$ are independent. This restrictive assumption can however be relieved to allow highly correlated input samples without losing the convergence, as is shown in [46]. Using the initial value of $\mathbf{h}(0)$ for the weight vector, $k+1$ iterations of (A3) will result in

$$E\{\mathbf{h}(k+1)\} = [\mathbf{I} + 2\beta\mathbf{R}_{xx}(k)]^{k+1} \mathbf{h}(0) - 2\beta \sum_{i=0}^k [\mathbf{I} + 2\beta\mathbf{R}_{xx}(k)]^i \mathbf{r}_{xy}(k). \quad (\text{A4})$$

To obtain a relation for the step size parameter β and the eigenvalues of the sample autocorrelation matrix, $\mathbf{R}_{xx}(k)$ can be rewritten using a similarity transformation \mathbf{Q} as

$$\mathbf{R}_{xx}(k) = \mathbf{Q}^{-1}\mathbf{\Lambda}\mathbf{Q}, \quad (\text{A5})$$

where $\mathbf{\Lambda}$ is a diagonal matrix with eigenvalues of $\mathbf{R}_{xx}(k)$ on the diagonal

$$\mathbf{\Lambda} \triangleq \begin{bmatrix} \lambda_1 & 0 & \cdots & 0 \\ 0 & \lambda_2 & \cdots & 0 \\ \vdots & & \ddots & \vdots \\ 0 & 0 & \cdots & \lambda_L \end{bmatrix}. \quad (\text{A6})$$

Equation (A4) can now be expressed as

$$\begin{aligned} E \{ \mathbf{h}(k+1) \} &= [\mathbf{I} + 2\beta \mathbf{Q}^{-1} \mathbf{\Lambda} \mathbf{Q}]^{k+1} \mathbf{h}(0) - 2\beta \sum_{i=0}^k [\mathbf{I} + 2\beta \mathbf{Q}^{-1} \mathbf{\Lambda} \mathbf{Q}]^i \mathbf{r}_{xy}(k) \\ &= \mathbf{Q}^{-1} [\mathbf{I} + 2\beta \mathbf{\Lambda}]^{k+1} \mathbf{Q} \mathbf{h}(0) - 2\beta \mathbf{Q}^{-1} \sum_{i=0}^k [\mathbf{I} + 2\beta \mathbf{\Lambda}]^i \mathbf{Q} \mathbf{r}_{xy}(k). \end{aligned} \quad (\text{A7})$$

Requiring that the diagonal matrix $[\mathbf{I} + 2\beta \mathbf{\Lambda}]$ has all its diagonal elements below magnitude of unity, the first term in (A7) vanishes as the number of iterations increases as

$$\lim_{k \rightarrow \infty} [\mathbf{I} + 2\beta \mathbf{\Lambda}]^{k+1} \rightarrow 0. \quad (\text{A8})$$

Convergence of the second term in (A7) can be analyzed by using the geometric series summation formula, which will result in

$$\lim_{k \rightarrow \infty} \sum_{i=0}^k [\mathbf{I} + 2\beta \mathbf{\Lambda}]^i = -\frac{1}{2\beta} \mathbf{\Lambda}^{-1}. \quad (\text{A9})$$

Combining (A8) and (A9), it can be seen that the weight coefficients in (A7) converge towards the Wiener-Hopf solution of optimal weights as

$$\begin{aligned} \lim_{k \rightarrow \infty} E \{ \mathbf{h}(k+1) \} &= \mathbf{Q}^{-1} \mathbf{\Lambda}^{-1} \mathbf{Q} \mathbf{r}_{xy}(k) \\ &= \mathbf{R}_{xx}^{-1}(k) \mathbf{r}_{xy}(k) \end{aligned} \quad (\text{A10})$$

LMS algorithm convergence towards the optimal Wiener solution is guaranteed only if the step size parameter β is set within certain limits. The previous requirement for the magnitude of the diagonal elements of matrix $[\mathbf{I} + 2\beta \mathbf{\Lambda}]$ to be less than unity gives bounds for β . Since all eigenvalues of \mathbf{R}_{xx} are positive, that is the diagonal terms of $\mathbf{\Lambda}$ are positive, the bounds for β are given by

$$|1 + 2\beta \lambda_{max}| < 1, \quad (\text{A11})$$

or simply

$$-\frac{1}{\lambda_{max}} < \beta < 0, \quad (\text{A12})$$

where λ_{max} is the maximum eigenvalue of \mathbf{R}_{xx} .